University of London
Imperial College of Science, Technology and Medicine
Department of Physics

An experimental investigation into tokamak edge MHD behaviour

Phillip Jones B.Sc.

October 2003

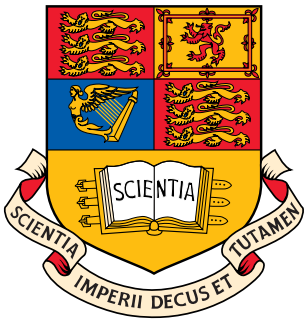

A thesis submitted in partial fulfilment of the requirements for the degree of Doctor of Philosophy of Science of the University of London and the Diploma of Imperial College

To Tara...
without whom, I could not have done this.

Acknowledgements

This work was jointly funded by the UK department of Trade and Industry and Euratom. Financial support was provided by EPSRC and UKAEA.

I would like to thank my supervisors at Culham Laboratory, Prof. Patrick Carolan and Dr. Anthony Field, and my supervisor at Imperial College, Dr. Micheal Coppins for their help and advice throughout my time as a PhD student.

Working at Culham Science Centre is very much a team effort and nobody could achieve their objectives without the mutual assistance of the entire COMPASS-D, MAST, and ECRH teams but special thanks must be given to the following people who went that extra mile to help; Hendrick Meyer for informal supervision and help with all things Linux, Howard Wilson, Mathew Hole, and Colin Roach, for writing various numerical stability analysis codes and their inexhaustible patients in helping me run those codes, Steve Cowley for insights into ELM physics and Steve's brother for drawing the ballooning mode diagram, and Richard Martin, for writing get_ida, Xpad, and Xpad6.

Technical expertise was supplied by Gordon Harrison and the special techniques group. IT support far beyond the call of duty was provided by Nick Benterman and John Waterhouse.

Personal thanks go to the following people; Andrew Knight of Imperial College for making me feel welcome in the department, Mikhail Tournianski and Mike Walsh for their support and encouragement, Micheal Coppins for his good humour and cups of coffee, Ian Jenkins, Ivor Coffey, and all the participants, past and present of the table that tells it like it is.

Abstract

The HELIOS-CELESTE hybrid diagnostic (Carolan et al., 2001) is a multi-chord, multi-time active spectroscopic diagnostic attached to the COMPASS-D (Fielding et al., 1996) tokamak. Line intensity ratios from a neutral helium jet are used to measure n_e and T_e at the plasma edge, making use of emission rates based on a full collisional-radiative model of neutral helium (Summers, 1994). Doppler spectroscopy of HeII ions is used to measure velocity and temperature of those ions in the same region. Synergy of the two diagnostics produces neutral density and radial electric field measurements.

Edge Localised Modes (ELMs) (Zohm, 1996) are short, quasi-periodic bursts of particles and energy from the plasma edge, during H-mode (Wagner et al, 1982). A review of ELM phenomenology and theories is presented.

A simple model of line intensity of one of the neutral helium lines based on the coronal model is used as a self-consistency check of the HELIOS measurements. Measurements from HELIOS are benchmarked against Thomson scattering measurements. Combining the HELIOS and CELESTE diagnostic is shown to enhance the usefulness of both diagnostics and the synergy is used to lend new insight into H-mode transition behavior, most notably the absence of a radial electric field before the transition into H-mode.

Data from the HELIOS diagnostic shows a fall in the edge electron pressure gradient prior to the onset of type III ELMs on COMPASS-D. Data from Thomson scattering and a linear D_α camera on MAST is used to validate the observation. This result is compared with a leading theory of ELM dynamics and is found to contribute to the development of the theory.

Table of Contents

List of Figures

Chapter 1

Introduction

The purpose of this work was to develop, operate and analyse the data from a diagnostic known as the helium injection and optical spectroscopy (HELIOS) - charge exchange line emission spectroscopy for temperature evaluation (CELESTE) Hybrid (Carolan et al., 2001) and to use that data as part of an investigation into edge magnetohydrodynamic (MHD) behaviour (Wilson et al., 2000) on the compact assembly for shaping studies (COMPASS)-D tokamak (Fielding et al., 1996).

A tokamak is an axisymmetric torus shaped device in which plasma is confined using externally imposed and internally generated magnetic fields. The externally applied toroidal magnetic field must be many times greater than the mainly internally generated poloidal field in order to suppress the main magnetohydrodynamic instabilities (Artsimovich, 1972b; Wesson, 1997). This is the main difference between tokamak devices and the earlier design of the Reverse Field Pinch (Baker, 1987). The aim is to confine the plasma at high enough temperatures and densities to achieve sustained nuclear fusion which could be used as an energy source. A major difficulty facing tokamak physicists is that of instabilities known as edge locaised modes (ELMs) (Zohm, 1996) in the plasma which adversely affect confinement when in high confinement mode (H-mode) (Wagner et al, 1982) and may result in damage to certain plasma facing components.

In this thesis, the leading theories of the causes of ELMs will be examined. A model will be presented of ELM behaviour that describes regions of normalised edge current ($j_{\|}/\langle j \rangle$) and normalised edge pressure gradient (α) parameter space that are stable and unstable (Connor et al., 1998). The model suggests that access to H-mode may be dependent on stabilisation of a current driven instability known as the peeling instability, which occurs at low electron collision frequency (ν_e). It would also be the case that for H-modes with ELMs, the length of the inter-ELM period is dependent

on the current diffusion time τ_η, which is dependent on the edge resistivity, η.

The HELIOS-CELESTE hybrid diagnostic is a synergy of two spectrometers, (Field et al., 1999a; Carolan et al., 1998) that look at the same region of the COMPASS-D tokamak. The region is at the edge of the plasma on the outboard side, covering approximately $5cm$ around the plasma boundary known as the last closed flux surface (LCFS) or separatrix (Wesson, 1997). The diagnostics measure electron temperature and density profiles over the region, and poloidal velocity and temperature of singly ionised helium. This data can be combined in synergy to extract the neutral density and radial electric field at the plasma edge (Meyer et al., 2000).

1.1 Nuclear fusion

Nuclear fusion is the process whereby light nuclei collide and fuse to form heavier nuclei and thereby release energy due to the difference between the sum of the binding energies of the fuel nuclei and the binding energy of the product nuclei. The major difficulty arises from trying to get the nuclei close enough to overcome Coulomb repulsion and allow fusion. It is not necessary to make the nuclei collide, due to quantum mechanical tunnelling, the probability of fusion is dependent on how close two nuclei are to one another. In a neutral gas, at room temperature and atmospheric pressure, the collisions between the neutral atoms do not allow nuclei to get close enough to each other to fuse. In order to get large numbers of nuclei to fuse, it is necessary to heat and compress the gas to such an extent that ionisation takes place and the gas becomes a plasma.

Once ionised, the plasma must react before it neutralises or disperses. To prevent instant re-combination, the process must be performed in a vacuum chamber. For more energy to be generated by the reactions than was needed to heat and ionise the gas, the plasma must satisfy the Lawson criterion (Lawson, 1957),

$$n_i \tau_E > \frac{3T_i}{\frac{\eta_l}{1-\eta_l}\frac{1}{4}\langle \sigma v_i \rangle E_f - bT_i^{1/2}}. \tag{1.1}$$

In the above, η_l is Lawson's efficiency co-efficient, E_f is the energy released from each fusion reaction, and b is the bremsstrahlung coefficient. To satisfy the condition, the reaction must either occur very quickly, as in the case of inertial confinement (Holzrichter, 1983), or the plasma must be confined for a long period of time, as in the case of magnetic confinement, the method used by tokamaks.

1.1.1 Magnetic confinement

Magnetic fields, or ***B**-fields* are used to confine plasma for long enough periods of time at high density and temperature so that more energy is produced by fusion than is consumed by the heating and compression of the plasma. Simply put, a plasma may be confined by a magnetic field according to a simplified from of the Navier-Stokes equation. For a fluid where there are no external forces and there is radial force balance,

$$\boldsymbol{j} \times \boldsymbol{B} = \boldsymbol{\nabla} p. \tag{1.2}$$

The simplicity of the equation hides the complexity of the issue. In the following section, a short introduction to the difficulties associated with magnetic confinement will be given.

Charged particles in a magnetic field follow a helical trajectory with the guiding centre of their orbits following magnetic field lines unless a drift is caused by a gradient or curvature of the magnetic field, or the presence of an electric field (Chen, 1984). This behaviour can be explained by simple electromagnetism. Splitting the velocity of an individual particle into two components; parallel ($\boldsymbol{v}_{\|}$) and perpendicular ($\boldsymbol{v}_{\perp}$) to the magnetic field, each component can be considered separately in a Lorentz equation,

$$m\frac{\mathrm{d}\boldsymbol{v}_{\|,\perp}}{\mathrm{d}t} = e\left(\boldsymbol{E} + \boldsymbol{v}_{\|,\perp} \times \boldsymbol{B}\right). \tag{1.3}$$

In the absence of an electric field, it is clear that the component of the particle's velocity along the magnetic field is unchanged, however the particle will experience a force that is directed at right angles to the magnetic field lines. This force causes the particle to orbit around the field line in a helical trajectory. This means that plasma can be confined by a magnetic field. The problem with using a parallel magnetic field is that plasma will diffuse along the magnetic field lines indefinitely or until the particles hit the walls of whatever vacuum vessel the experiment happens to be held in.

One early type of magnetic confinement machine was the magnetic mirror or magnetic bottle (Itatani et al., 1980). This type of machine consisted of a solenoid with strong magnetic coils at each end. The two end coils increase the strength of the magnetic field, thereby compressing the magnetic field lines as shown in figure 1.1.

To explain how this type of confinement device works, it is necessary to introduce

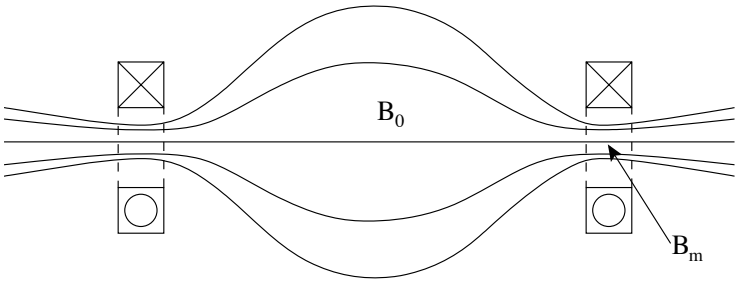

Figure 1.1: *A simple way of confining a plasma is in a magnetic mirror. A parallel magnetic field is compressed using a strong magnetic coil at each end of the device.*

the magnetic moment,

$$\mu \equiv \frac{1}{2}\frac{mv_{\perp}^2}{B}, \tag{1.4}$$

where m is the mass of the particle and $v_{\perp}$ is its velocity perpendicular to the magnetic field. For each particle, μ is invariant, provided that the particle moves relatively slowly from the region with low $\boldsymbol{B}$-field to high $\boldsymbol{B}$-field compared to the time it takes to make one Larmor orbit. As a given particle moves from a region of low $\boldsymbol{B}$-field to high $\boldsymbol{B}$-field, the particles perpendicular velocity will increase. By conservation of energy, the parallel velocity must decrease. This phenomenon can be interpreted as a force parallel to the $\boldsymbol{B}$-field,

$$\boldsymbol{F}_{\parallel} = -\mu \boldsymbol{\nabla}_{\parallel} \boldsymbol{B}. \tag{1.5}$$

This force will tend to reflect the particle back into the mirror.

This type of confinement is not suitable for sustained plasma discharges due to the fact that only a proportion of the particles with sufficiently high $v_{\perp}$, for any given parallel velocity $v_{\parallel}$ will be reflected. By considering that μ is invariant,

$$\frac{\frac{1}{2}mv_{\perp 0}^2}{B_0} = \frac{\frac{1}{2}mv_{\perp m}^2}{B_m}. \tag{1.6}$$

In the above, 0 indicates the weakest point in the field and m indicates the throat of the mirror. Appealing to conservation of energy allows the limiting case where reflection only just occurs to be defined by,

$$v_{m\perp}^2 = v_{\perp 0}^2 + v_{\parallel 0}^2 \equiv v_0^2. \tag{1.7}$$

Combining equations 1.6 and 1.7 gives,

$$\frac{B_0}{B_m} = \frac{v_{\perp 0}^2}{v_{\perp m}^2} = \frac{v_{\perp 0}^2}{v_0^2} \equiv sin^2\theta_g. \tag{1.8}$$

where θ_g is the angle between the direction of motion of the guiding centre of the particle and the field lines in the weakest part of the field. This angle defines a *loss cone* in trajectory space. All particles within the cone are not confined. Since particles are deflected by 90° over one collision time then the effective confinement is one collision time. One solution to the problem is to *bend* the magnetic field lines round into a torus so that the field lines have no ends.

A simple torus cannot confine a plasma well either. In a toroidal magnetic field, the strength of the field will fall off with distance from the centre of the radius of curvature. This magnetic field gradient will cause a particle drift. The drift velocity can be calculated using the generalised drift equation,

$$V_F = \frac{\boldsymbol{F} \times \boldsymbol{B}}{qB^2}. \tag{1.9}$$

Substituting in equation 1.5 gives,

$$V_{\nabla B} = -\frac{\mu \boldsymbol{\nabla} B \times \boldsymbol{B}}{qB^2}. \tag{1.10}$$

The effect of this drift is illustrated in figure 1.2a. Note that particles of opposite charge will drift in opposite directions and so, this drift will cause an ambipolar electric field to develop. The ambipolar electric field acts in the opposite direction to the drift and therefore acts against particle loss, however the electric field leads to a second particle drift by which both positive and negative particles will drift in the same radial direction. The velocity can be derived by substituting $F = qE$ into equation 1.9,

$$V_{E\times B} = \frac{\boldsymbol{E} \times \boldsymbol{B}}{B^2}. \tag{1.11}$$

The effect of which is illustrated in figure 1.2b. The combination of these two drifts prevents such a simple design from effectively confining a plasma. In order to achieve a well confined plasma, it is necessary to cause the particles to orbit in both the toroidal and poloidal directions, thereby short-circuiting the $\boldsymbol{E} \times \boldsymbol{B}$ drift.

1.2 Tokamaks

It is important at this point to describe in general terms, the basic geometry and coordinate systems for tokamaks. Figure 1.3 shows the topology, it is clear that the Cartesian coordinate system would be of little use as it would fail to make proper use of the tokamak's radial symmetry. A cylindrical coordinate system: major radius (R),

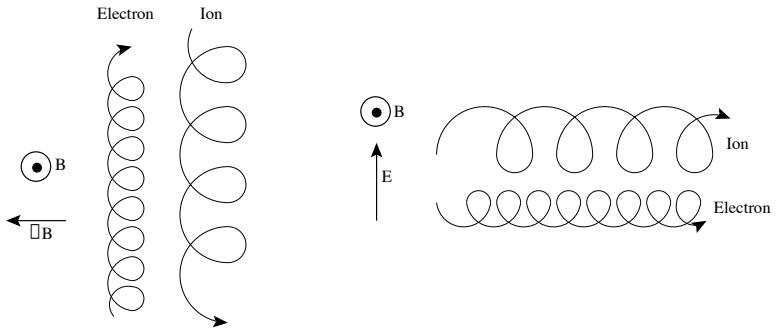

(a) *The ∇B drift.* **(b)** *The $E \times B$ drift.*

Figure 1.2: *Particle drifts that result in a loss of particles from a toroidal magnetic field.*

height (Z), and toroidal angle (ϕ), makes use of toroidal axisymmetry. Alternatively, to make use of the poloidal symmetry, a toric coordinate system: toroidal angle, (ϕ), poloidal angle (θ), and the minor radius (r) might be used. In reality, the plasma does not have a circular cross-section and so it is often useful to define a coordinate system that relies on a physical property of the plasma itself, poloidal flux (ψ), which will be explained in more depth in section 1.3.1.

1.2.1 History

It was noted in section 1.1.1 that for a simple toroidal field with no poloidal twist, the net result of the particle drift would be a loss of particles outward in the direction parallel to the major radius. Several designs have been considered to address the problem of the particle drift. The earliest concept was known as the stellarator. The original idea was a *figure of 8* vacuum vessel with magnetic coils attached to the side, this concept was eventually abandoned as impractical due to the insurmountable engineering problems that it provided. Modern stellarators (Anderson and Garabedian, 1994) have helical magnetic coils which give rise to magnetic field lines that twist in the poloidal plane. The most notable aspect of the stellarator is that it relies entirely on externally generated magnetic fields.

A second method of generating the poloidal orbit that is necessary for confinement is by inducing a current in the plasma itself. The pinch effect (*cf.* figure 1.4) is achieved by using the plasma as if it were the secondary coil in a transformer. The induced current generates a poloidal magnetic field. This method is used in several

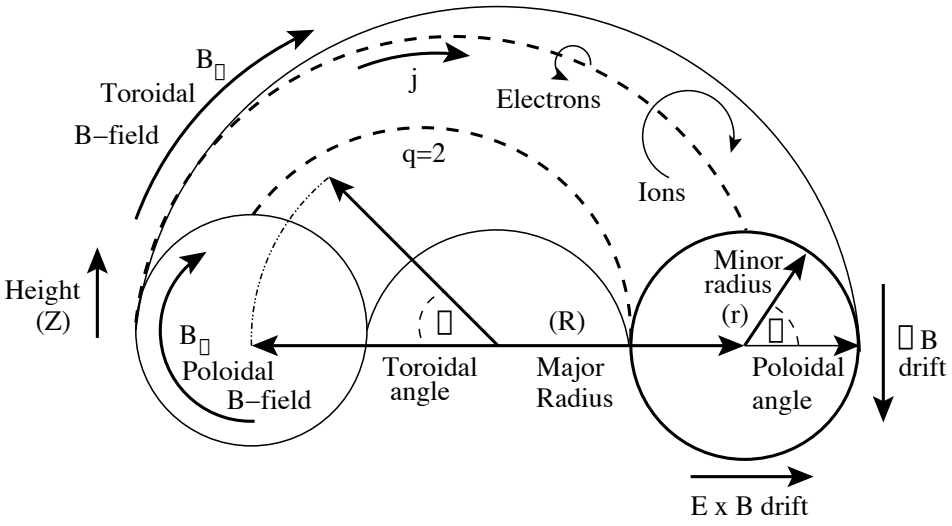

Figure 1.3: *The toroidal coordinate system.*

forms of confinement device including the spheromak (Browning et al, 1989), reverse field pinch (RFP) (Baker, 1987), and tokamak (Artsimovich, 1972b; Wesson, 1997). The spheromak relies entirely on internally generated magnetic field and has no central core. The RFP and tokamak are similar devices that use the combination of externally applied and internally generated toroidal and poloidal fields to form the required helical topology. They differ in so much as the RFP uses a much smaller externally applied field and relies on the internal relaxation of the plasma to reach a stable state. The tokamak uses a strong externally applied magnetic field so that $B_\phi \gg B_\theta$ to stabilise the plasma. Tokamak confinement times are much larger than for the RFP or Spheromak.

1.2.2 The COMPASS-D and MAST tokamaks

Almost all of the work that will be presented in this report was carried out on the COMPASS-D tokamak at Culham Science Centre (Fielding et al., 1996). COMPASS stands for Compact Assembly for Shaping Studies, D refers to the shape of the poloidal cross-section of the vessel. COMPASS-D is especially important to the tokamak research programme as it is the smallest tokamak ($R = 0.56m, r = 0.17m$) with similar geometry to the Joint European Torus (JET) (Gormezano et al, 2001) and the planned International Experimental Tokamak Reactor (ITER) (Aymar, 1996) which means that it applies a large weighting to the scaling laws drawn up from the ITER database.

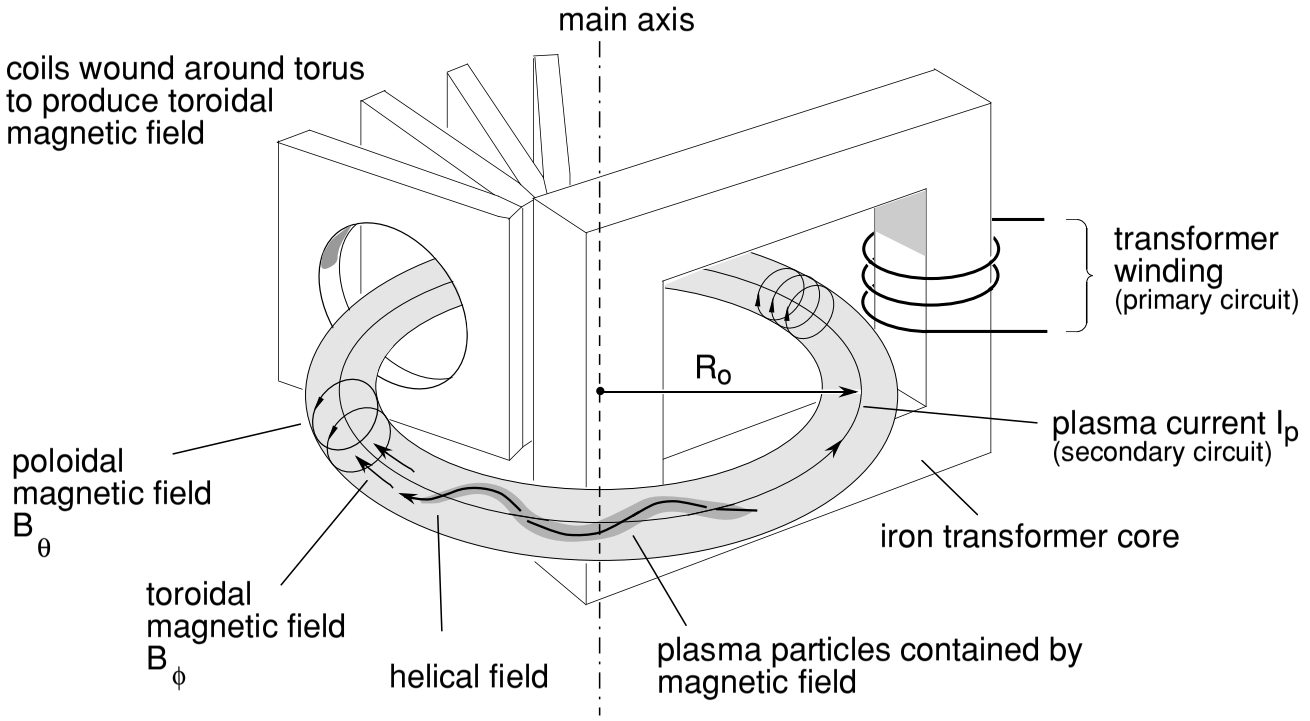

Figure 1.4: *Schematic diagram of a tokamak showing transformer action, pinch effect and the resulting magnetic fields.*

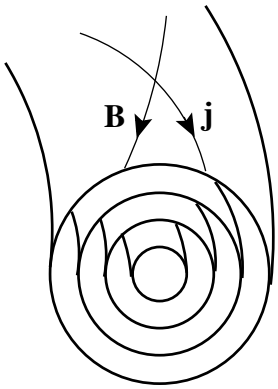

Figure 1.5: *Magnetic field lines and current lines lie on nested surfaces of constant poloidal magnetic flux.*

The Mega Amp Spherical Tokamak (MAST) (Carolan et al., 2002) is a tight aspect-ratio device also based at Culham Science Centre. The advanced concept of the tight aspect-ratio or spherical tokamak was conceived in a effort to make a tokamak that was simpler, smaller and cheaper than the conventional configuration. The aspect ratio, defined as the major radius divided by the minor radius, (R/r) of MAST is nominally 1.4 compared with the more usual ITER-like aspect ratio of 2.5.

1.3 Magnetic flux, ψ

The magnetic flux through a closed loop, of area $\boldsymbol{S}$ is equal to the number of field lines passing through the loop in one direction, minus those passing through in the opposite direction. Mathematically,

$$\psi = \int_S \boldsymbol{B} \cdot \mathrm{d}\boldsymbol{S}. \tag{1.12}$$

Since a torus is axisymmetric about the major axis, by specifying R, and Z, a loop around the major axis is defined. The poloidal magnetic flux is the magnetic flux that passes through this loop. Since magnetic field lines can not cross, they are frozen into the plasma and lie on nested toroidal surfaces of constant poloidal magnetic flux. From force balance, $\boldsymbol{j} \times \boldsymbol{B} = \nabla p$, therefore $\boldsymbol{B} \cdot \boldsymbol{\nabla} p = 0$ and $\boldsymbol{j} \cdot \boldsymbol{\nabla} p = 0$, lines of $\boldsymbol{B}$, and $\boldsymbol{j}$, lie on surfaces of constant p, an illustration of which is shown in figure 1.5.

By symmetry, the same argument can be applied to describe surfaces of constant toroidal flux. The parameter of toroidal flux is not used during this investigation. For that reason, in this work, the terms *magnetic flux* and *flux function* should be taken to refer to poloidal flux.

1.3.1 Flux coordinates

It is often useful to introduce flux coordinates (ϕ, ψ, θ) into our analysis of plasma parameters. Figure 1.5 shows nested surfaces of constant magnetic flux for a plasma with a circular poloidal cross-section. Since magnetic field lines and therefore surfaces of constant flux are frozen into the plasma (section 1.3), a set of values for ϕ, ψ, and θ specify a position in the plasma itself, rather than the vessel. Real tokamak plasmas generally do not have circular poloidal cross-sections, and pressure effects can significantly distort the flux surfaces so that in the general case, numerical reconstruction of the shape of the magnetic surfaces is required.

In many cases, parameters can be considered to be flux quantities, an example of which is electron density, n_e, if the rate of diffusion along the field line is on a shorter time scale than local changes in the plasma. In these cases, measurements taken in different parts of the plasma that lie on the same flux surfaces can be directly compared, *i.e.* $n_e = n_e(\psi)$. As will be seen in chapter 5, the ability to compare measurements from different parts of the plasma that lie on the same flux surface is extremely useful.

Since the pinch effect is the result of current flow through the plasma (see figure 1.4), which is induced by external flux linkage from a solenoid on the major axis, the quantity of magnetic flux at any given point must be constantly changing throughout each discharge. It can be seen that magnetic flux is a useful parameter when considering measurements within a single time frame but when comparing multiple time points, the actual value of magnetic flux on a given surface will have changed. To compensate, the external flux, which is equal to the flux on the magnetic axis, is subtracted leaving only the internal flux, which is then normalised. The transform is given below;

$$\psi_N = \frac{\psi - \psi_a}{\psi_a - \psi_b}. \tag{1.13}$$

In the above, ψ_a is the value of ψ at the magnetic axis and ψ_b is the value of ψ at the plasma edge. Normalised poloidal flux, ψ_N, ranges from 0 at the centre to 1 at the edge of the confined plasma, which is defined as the last closed flux surface (LCFS) or *separatrix*.

For studies of the plasma edge region, it is often convenient to measure parameters at set values of normalised flux, for example $\psi = 0.95$. The notation ψ_{95} or $\psi = 95\%$ are commonly used.

1.3.2 Magnetic equilibrium reconstruction, (EFIT)

In general, a physical measurement of a plasma parameter will be in real space coordinates and so some method is required to convert these into flux space coordinates.

Magnetic coils are placed on the vessel walls to directly measure the local magnetic field. The magnetic field inside the vessel is then reconstructed. Several numerical codes have been written to perform this task. The code used during this investigation is the Equilibrium reconstruction FIT (EFIT) code (Lao et al., 1985). EFIT solves the Grad-Shafranov equation (Shafranov, 1958),

$$j_\phi = R\,\frac{\mathrm{d}p}{\mathrm{d}\psi} + \frac{\mu_0}{R} f\,\frac{\mathrm{d}f}{\mathrm{d}\psi}. \tag{1.14}$$

Here, f is a new parameter, it is a flux function, like p, and is defined as,

$$f(\psi) = \frac{RB_\phi}{\mu_0}. \tag{1.15}$$

EFIT performs an iterative, multi-parameter fit to all available magnetic data. in order to reconstruct a poloidal cross-section of the plasma current and magnetic flux. EFIT is also capable of accepting a number of other measurements, like the pressure profile. The weight of fit for each parameter can be set according to confidence in the measurement or the known errors. EFIT outputs a number of parameters both global and local. Examples of EFIT output include ψ_N, B_r, B_ϕ and B_θ, current density, $j(\psi)$, and the total plasma current I_p.

Figure 1.6 is an example of a contour plot of ψ_N with the major radius and height shown. By interpolating the value of ψ for any given point in the cross-section, it is possible to translate the positions of data points in real space into flux coordinates.

1.3.3 Safety Factor, *q*

An important concept in stability theory is that of the safety factor, (q). The safety factor derives its name from the importance that it plays in determining stability.

Each magnetic field line in a tokamak that is in equilibrium undergoes a helical path, around the torus on its magnetic surface. At some toroidal angle, ϕ, the field line will pass through a particular position in the poloidal cross-section. After some change of angle, $\Delta\phi$, the field line will pass through the same position in the poloidal cross-section, q being defined as,

$$q = \frac{\Delta\phi}{2\pi}. \tag{1.16}$$

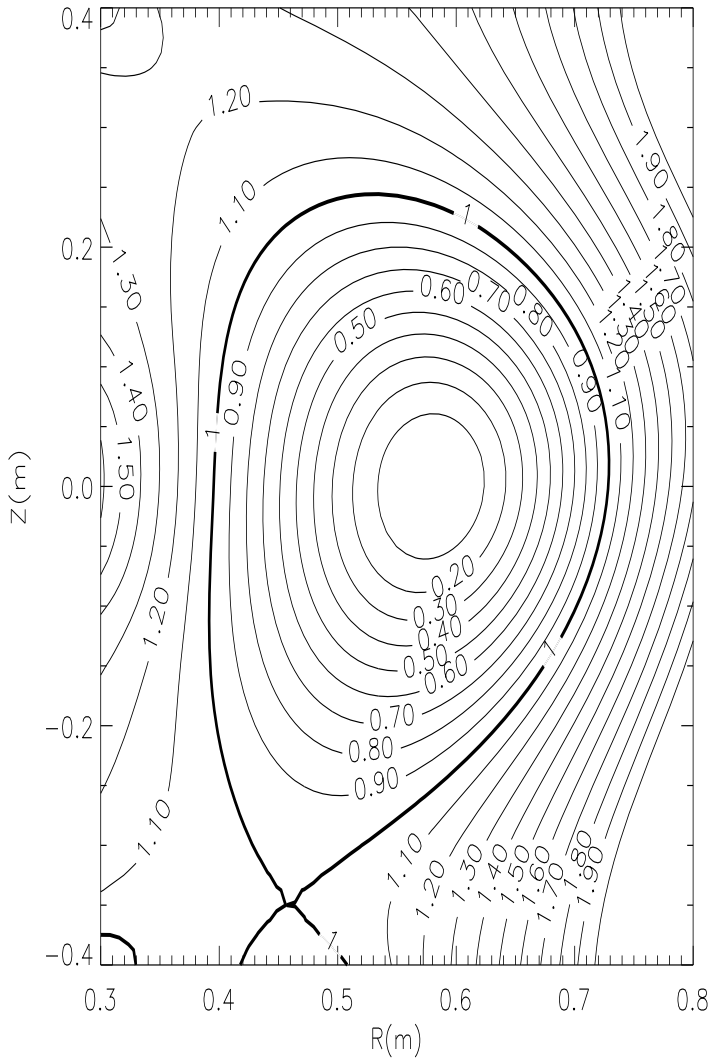

Figure 1.6: *Contour plot of ψ_N for discharge number 29759 at $t = 0.148s$. The separatrix is shown in bold.*

In other words, the q of a field line is equal to the number of toroidal rotations of the torus that the field line makes for every poloidal rotation. Some field lines will have a rational value of q. That means that the field lines travel a whole number of toroidal orbits in some whole number of poloidal orbits. For example, a $q = 3/2$ field line makes 3 toroidal circuits for every 2 in the poloidal direction and will be a closed loop. Not all field lines have rational q and so do not all join up with themselves. A more general method of calculating q at a point in the plasma is to make use of the equation of a field line,

$$\frac{R\,\mathrm{d}\phi}{\mathrm{d}s} = \frac{B_\phi}{B_\theta}. \tag{1.17}$$

where $\mathrm{d}s$ stands for the distance moved in the poloidal direction, $d\phi$ the toroidal angle moved through, with B_θ and B_ϕ referring to the poloidal and toroidal components of the magnetic field. Substituting equation 1.17 into equation 1.16 gives,

$$q = \frac{1}{2\pi}\oint \frac{1}{R}\frac{B_\phi}{B_\theta}\,\mathrm{d}s. \tag{1.18}$$

where the integral is carried out over a single poloidal circuit around the flux surface. Magnetic field lines cannot cross, and so on any given surface of q, the pitch of the magnetic field lines(B_ϕ/B_θ), for each toroidal circuit of the field lines must be the same. Equation 1.18 then tells us that q is the same for all magnetic field lines lying on any given magnetic surface. The corollary of this is that q is a flux function, *i.e.* $q = q(\psi)$.

1.4 Neo-classical diffusion

Collisional transport in tokamaks is dependent mainly on toroidal effects. The particle and heat fluxes are larger in toroidal geometry than for those of a simple cylinder (Wesson, 1997). To distinguish between the cases, diffusion for a cylinder is referred to as classical, whilst in toroidal geometry, there is neo-classical diffusion. An important concept for neo-classical diffusion is the bounce time. Particles on the outboard side of the torus will move along field lines from the region of low $\boldsymbol{B}$-field on the outboard mid-plane to high $\boldsymbol{B}$-field on the inboard mid-plane. This variation in $\boldsymbol{B}$-field is responsible for a magnetic mirror effect, similar to that outlined in section 1.1.1. The confinement regime is dependent on how the electron bounce frequency (as a result of the mirror effect), is related to the electron-electron collision frequency

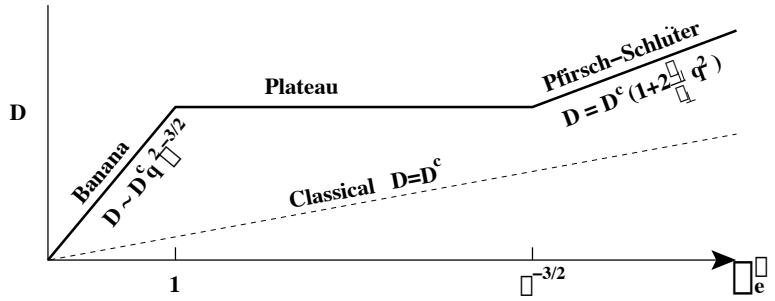

Figure 1.7: *Diffusion coefficients for neo-classical (solid line) and classical (dashed line) with respect to collision frequency.*

of the plasma. The bounce time is given by,

$$\omega_b \sim \frac{\varepsilon^{3/2} v_{eT}}{qR}, \tag{1.19}$$

where ε is the inverse aspect ratio of the flux surface and v_{eT}, is the electron thermal velocity. The electron-electron collision frequency, which from here on will be referred to as the collisionality is defined by,

$$\nu_e = \frac{n_e e^4 \ln \Lambda}{\epsilon_0^2 m_e^{1/2} T_e^{3/2}}. \tag{1.20}$$

Here, ϵ_0 is the permittivity of free space and $\ln \Lambda$ is the Coulomb logarithm which compensates for small angle collisions as a result of long range Coulomb interactions (Chen, 1984). The collisionality is often normalised to the bounce frequency. The normalised collisionality is given by,

$$\nu_e^* = \frac{\nu_e q R}{\varepsilon^{3/2} v_{eT}}. \tag{1.21}$$

The normalised bounce frequency (ν_e^*), is a flux function. In general however, ν_e^* does not vary by more than an order of magnitude through much of the plasma. Since ν_e^* is constant to within an order of magnitude, the plasma can be considered to be one of three regimes: The *banana* regime, *Pfirsch-Schlüter* regime, or *plateau* regime. As a complication, ν_e^* near the edge can be very different to that in the rest of the plasma as T_e and n_e are important factors in ν_e. As will be shown later, the collisionality and confinement regime at the edge is important in stability theory.

Figure 1.7 shows how neo-classical diffusion changes with collision frequency compared with simple classical diffusion.

1. The *banana* regime is defined as the collisionless regime, when the electron collision frequency is lower than the bounce frequency, $\nu_e^* < 1$. The regime is so-called because the combination of the mirror effect and $\nabla \boldsymbol{B}$ drift causes the trapped particles to trace out banana-shaped orbits in the tokamak, like the one shown in figure 1.8.

2. The *Pfirsch-Schlüter* regime occurs when the collisionality of the plasma is sufficient for the number of trapped particles to be negligible and a fluid model can be applied to the plasma. The criterion for this regime is $\nu_e^* > \varepsilon^{-3/2}$.

3. The *plateau* regime lies between the two previous regimes that are separated by a factor of $\varepsilon^{-3/2}$. In this regime, the diffusion is dominated by a small class of particles with such a low velocity parallel to the $\boldsymbol{B}$-field ($v_{\|}$) that their diffusion coefficient is unaffected by the collisionality of the bulk of the plasma.

The confinement regimes as such will not play a big part in this investigation. Their relevance here lies in the fact that there are pressure gradient and magnetic components to the plasma current density (equation 1.14). In the banana regime, the pressure gradient component is more important. To understand why this is the case, it is important to look at two important mechanisms for generating current density in tokamaks; the bootstrap current (see section 1.4.1), and the Pfirsh-Schlüter current (see section 1.4.2). In section 2.6, the relevance of the regimes of confinement to stability theory and ELM physics will be explained.

1.4.1 The bootstrap current

The bootstrap current was described by Bickerton et al. (1971). The trajectories of electrons on trapped orbits are the result of the combination of the mirror effect and $\nabla \boldsymbol{B}$ drift. An example of a trapped particle orbit is shown in figure 1.8. These are known as banana orbits due to their distinctive shape.

Collisions between trapped and passing electrons transfer momentum into the passing electrons. Since there is a density gradient in the tokamak and the banana orbits have a finite width, there will be more trapped electrons travelling in the direction of the field lines than against them on any given flux surface. The passing electrons have an equilibrium velocity which is determined by a balance of momentum between the trapped electrons and the relatively stationary ions. The extra momentum given to the passing electrons results in the bootstrap current which can be estimated

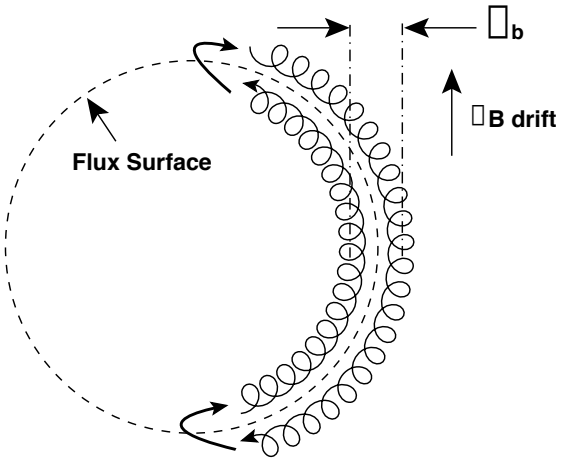

Figure 1.8: *A banana orbit as traced out by a trapped electron in a tokamak.*

using the formula (Wesson, 1997),

$$j_b \sim -\frac{\varepsilon^{1/2}}{B_\theta} T_e \frac{\mathrm{d}n_e}{\mathrm{d}r}. \tag{1.22}$$

At high collisionality, the trapped particle fraction drops as the plasma enters the plateau regime, the banana orbits are disrupted, and the bootstrap current is suppressed.

1.4.2 The Pfirsch-Schlüter current

This phenomena was first discovered by Pfirsch and Schlüter (1962). There is a small current perpendicular to $\boldsymbol{B}$, the bulk of which is a diamagnetic current as a result of the density gradient in the tokamak. Due to the variation in the $\boldsymbol{B}$-field, the poloidal velocity of the passing particles is reduced as they reach the top part of the tokamak which leads to a charge separation and an electric field. The electric field drives a current along the magnetic field lines. Due to the geometry of the tokamak, this current is parallel to the $\boldsymbol{B}$-field on the outboard side and anti-parallel on the inboard side. The Pfirsch-Schlüter current is given by,

$$j_{PS} = -\frac{2}{B_p} \frac{r}{R} \frac{\mathrm{d}p}{\mathrm{d}r} \cos\theta. \tag{1.23}$$

1.5 Magnetohydrodynamics, (MHD)

MHD is a macroscopic, dynamic description of an electrically conducting fluid immersed in a magnetic field (Hopcraft, 1993). Unlike the physics of particle drifts that

were shown in section 1.1.1, the plasma is treated like a fluid rather than a collection of positively and negatively charged particles. In order for such a model to be valid, the plasma must be quasi-neutral and locally Maxwellian (Chen, 1984).

1.5.1 MHD Waves and instabilities

Starting with a plasma in axisymmetric equilibrium (section 1.3), some kind of external disturbance may displace an element of the plasma and excite an instability or wave. It is usual to consider a single Fourier mode of the form,

$$\boldsymbol{\xi} = \boldsymbol{\xi_0} \exp\left\{i\left(\boldsymbol{k}\cdot\boldsymbol{x} - \omega t\right)\right\}, \tag{1.24}$$

where ξ is the plasma displacement of the wave or instability, $\boldsymbol{k}$ is the wave vector, and ω is the frequency. The wave or instability will have a dispersion relation, that is $\omega \equiv \omega(\boldsymbol{k})$. If the dispersion relation is such that ω is real, then the result is a wave. If ω is imaginary then equation 1.24 becomes,

$$\boldsymbol{\xi} = \boldsymbol{\xi_0} \exp\left\{i\boldsymbol{k}\cdot\boldsymbol{x} + \gamma t\right\}, \tag{1.25}$$

where $\gamma = -i\omega$ and is called the growth term. This special case of the wave equation does not oscillate in time but represents an exponentially growing instability.

The physics of instability growth in plasmas is more complex than in other situations. The main complicating factor being the presence of charge carrying particles making the physics of instabilities a combination of electromagnetic and kinetic effects. There are many types of instabilities, one important class with regard to tokamaks, are a group called MHD instabilities (Bateman, 1978). For an instability to be classified as an MHD phenomenon, the magnetic field must play a central role. Examples of two such instabilities are the ballooning mode (see section 2.4.3) and peeling mode (see section 2.4.4).

The physics of these phenomena are beyond the scope of this short introduction to tokamak physics (see chapter 2). Suffice to say that MHD instabilities are especially dangerous on surfaces of rational q. If a whole number of wavelengths fit onto a closed magnetic field line, the wave or instability is resonant on that q surface. Tiny perturbations that will excite an instability will always be present in a tokamak plasma so the mere existence of conditions favorable to growth is sufficient to ensure growth of the instability.

1.5.2 Edge Locaised Modes, ELMs

In chapter 2, the concepts of low and high confinement modes (Wagner et al, 1982), will be explained. A brief introduction will be given here for the purposes of putting the rest of this chapter in context. The basic physics of confinement in tokamaks is not well understood. For this reason confinement of particles and energy is modelled by a series of scaling laws which correspond to modes of confinement. One of these modes is known as higher or H-mode and is characterised by the existence of steep gradients in temperature and density near to the plasma edge. A phenomena associated with H-mode is Edge Locaised Modes (ELMs), which are periodic bursts of bursts of particles and energy from the plasma edge.

ELMs represent an important area of research in tokamak physics. ELMs are detrimental for confinement and lead to large power deposition on certain plasma-facing components in tokamaks. In future, larger tokamaks, including possible next step devices like ITER (Loarte et al., 2000), ELMs will be potentially larger and more damaging. The understanding and control of these events is of the utmost importance.

A review of ELM phenomenology and theory is presented in chapter 2.

1.6 The HELIOS-CELESTE hybrid diagnostic

A spectrometer (Hutchinson, 1987; Conway, 1998) is a device for analyzing the spectral properties of a light source. The central component of a spectrometer is its diffraction grating, which is a high quality mirror with many fine grooves cut into the reflective surface. The edges of the grooves act as if they are discrete, coherent light sources and as such, they have an associated interference pattern. The corollary being that a diffraction grating will *split* a polychromatic light beam into several monochromatic beams. The practical result is a spatially separated spectrum, which can be used to tell a number of things about the conditions to which the ions that emit the light are being exposed.

HELIOS stands for HELium Injection and Optical Spectroscopy. HELIOS is an active spectroscopic diagnostic that works by the injection of neutral helium into the tokamak plasma, at the mid-plane, on the outboard side. The atoms of neutral helium become excited by collisions with free electrons in the plasma and emit light at certain characteristic wavelengths. The physics of this emission and how it was used to measure the temperature and density of the plasma electrons is explained in chapter 4. Light from the helium emission is collected by a set of collection optics and conveyed to a spectrometer by means of optical fibres. A representation of the

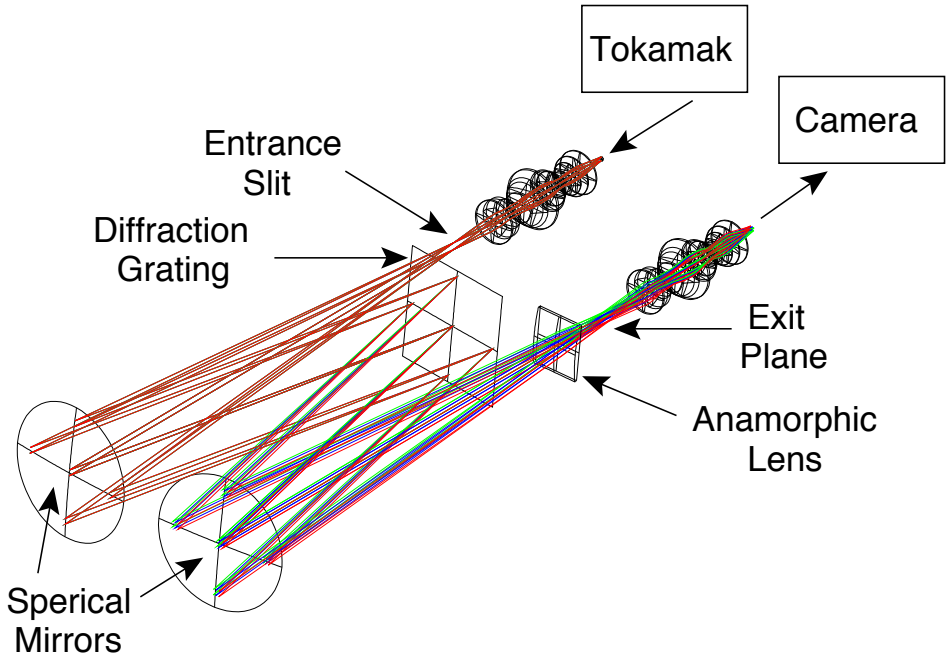

Figure 1.9: *A representation of the HELIOS spectrometer.*

HELIOS spectrometer (Field et al., 1999a) is shown in figure 1.9. A pair of $35mm$ front-to-front lenses was used to match the angle of divergence of the cone of light from the optical fibres to the F-number of the spectrometer, which optimises the throughput of the intensity of the light. A spherical mirror is used to reflect the light onto the diffraction grating, which separates the spectrum and reflects it, via a second spherical mirror to the exit plane. At the exit, an anamorphic lens corrects for the astigmatism caused by the off-axis use of the spherical mirrors and a second set of lenses matches the F-number of the spectrometer to a CCD camera that is used to record the spectra.

HELIOS uses the ratios of the intensities of helium spectral lines to extract electron temperature and density measurements. Ratios are used, as opposed to absolute intensities to cancel out the dependence of the intensities on the neutral helium density. HELIOS is particularly useful as it measures electron densities and temperatures with good spatial resolution at the plasma boundary. It also has much better temporal resolution than other electron temperature and density diagnostics like Thomson Scattering (Hutchinson, 1987). One of the aims of this work is to improve upon the temporal resolution and spatial coverage of HELIOS so that it can be used to measure profiles of electron density and temperature between ELM events.

CELESTE (Carolan et al., 1995) stands for Charge Exchange Light Emission Spectroscopy for Temperature Evaluation. CELESTE shares the same optics as HELIOS and so the two spectrometers are inherently aligned. The design of the spectrometer is similar to that of HELIOS but it has higher spectral, spatial, and temporal resolution. A further difference is that CELESTE is tuned to a wavelength of light emitted by singly ionised helium.

CELESTE is a Doppler spectrometer. Doppler spectroscopy relies on the phenomena of Doppler shifting whereby a wave emitted from a source moving either towards or away from the observer appears to have a different wavelength than if the object and observer were stationary with respect to one another. If the object is moving away from the observer, the wavelength appears to lengthen; this is known as red-shift, if the object is moving towards the observer, a blue-shift is the result. By taking advantage of this phenomenon, the velocity of the helium ions are calculated by measuring the shift of the spectral line from its known, unshifted wavelength. The thermal motion of the ions results in a broadening of the spectral line. This broadening is used to calculate the temperature of the helium ions.

Full details of the HELIOS and CELESTE spectrometers and how they were calibrated for this investigation are given in chapter 3. Details of the physics used to extract the plasma parameters from the observed spectra are given in chapter 4.

1.6.1 D_α emission

H_α or D_α emission, is a useful diagnostic tool employed on many tokamaks (Wesson, 1997). The observed light is emitted by recycled neutral hydrogen or deuterium, depending on which isotope is being used for the bulk ion in the plasma, due to its interaction with hot plasma that is diffusing out of the confined area. The COMPASS-D tokamak uses deuterium for its bulk ion.

The most common use of this diagnostic is as a measure of recycling particle fluxes, and by inference the quality of confinement. For this purpose, a spectrometer is used to analyse the light from the edge of the plasma and record the intensity of the D_α emission.

As an individual deuterium atom travels from the vacuum to the confined plasma, it will become excited as it suffers collisions with free electrons and will eventually become ionised. The excitation and ionisation rates compete and the strength of the D_α emission line is the result. Tournianski et al. (2001) proposed a model for the excitation and ionisation of neutral deuterium and found that both rates are strongly dependant on the plasma electron density in the region of densities and temperatures

that are observed in tokamak edge regions. Since the electron density and temperature in the confined plasma region are sufficient to ionise deuterium, the emission shell lies just outside the last closed flux surface. Furthermore, since the two rates are most strongly dependant on electron density, the thickness of the emission shell can be used to measure the electron density gradient at the edge.

The model by Tournianski et al. (2001) was used in this investigation to analyse neutral deuterium density and electron density gradient using the HELIOS spectrometer. Further details are presented in section 4.3.

1.7 Aims and motivation

The aims of this research project are:

- To upgrade the existing helium line ratio diagnostic, HELIOS and combine it with a high resolution Doppler spectrometer, CELESTE.
- To demonstrate the usefulness of not only both spectrometers separately but also the added advantages of combining the two diagnostics in synergy.
- To use the HELIOS-CELESTE hybrid diagnostic to investigate aspects of the L-H transition, in particular to diagnose the timing of the onset of the edge pedestal and electric field shear with respect to the transitions (Wagner et al, 1982).
- To use data from HELIOS in the development of a model for ELM dynamics that encompasses and extends one of the leading theories of tokamak stability (section 2.6).

Chapter 2

Edge Localised Modes

2.1 H-mode

In the absence of instabilities, the energy confinement time, τ_e for a toroidally confined plasma should be entirely determined by Coulomb collisions. In reality, τ_e for a tokamak is found to be much shorter than neo-classical theory would suggest (Wesson, 1997). The reasons for this are not well understood and so it has become necessary to describe confinement time using empirical scaling laws, which take the form of products of powers of the various parameters. Even this method does not adequately describe the confinement time over the full range of parameter space and so several regimes or *modes* of confinement have been defined, each with their own empirical scaling law to describe the confinement time.

Two important modes of confinement in present day tokamak physics are L-mode and H-mode (Stambaugh et al, 1990; Fielding et al., 1996). L-mode is defined by the use of external heating. Internal or ohmic heating relies on power absorbed by the plasma due to its resistance to the induced electrical current (section 1.2.1), according to $P_\Omega = \eta j^2$ where, in a steady state, P_Ω is the power into the plasma or the power required to maintain the current density (j), and η is the resistivity. Resistivity is dependent on electron collisionality, ν_e, which in turn is inversely dependent on temperature, $\eta \propto \nu_e \propto T_e^{-3/2}$. Ohmic heating of plasmas becomes ineffective as the temperature of the plasma increases. When external heating, such as radio frequency heating (Fielding et al., 1988) or neutral beam injection (Ciric et al., 2002) is used, plasma energy can be raised beyond the so-called saturation mode which is the point at which Ohmic heating becomes impossible due to loss of resistivity. The confinement time is found to degrade as heating power is increased (Goldston, 1984). The cause of this degradation in confinement time is unstable MHD activity,

that is plasma waves and instabilities that disrupt confinement and cause anomalous cross-field transport.

H-mode is the most developed of the high confinement modes and is considered by many to be the most likely candidate for a steady state operating regime. H-mode was first discovered on the ASDEX Tokamak (Wagner et al, 1982) during an investigation into the confinement properties of auxiliary-heated, high β tokamak discharges. The term β is the ratio of kinetic to magnetic pressure in the plasma,

$$\beta = 2\mu_0 \frac{p}{B^2}, \tag{2.1}$$

where p is the kinetic pressure. It was found that the discharge could be made to access an improved regime of confinement when the beam input power was above a certain critical value, P_{crit}. In general, a doubling or better of the confinement time was observed.

This behaviour was unexpected and the exact cause is not fully understood. One partial explanation of the effect describes a sudden change in the stability of the edge region of the plasma, that is the MHD activity mentioned above suddenly becomes quiescent or at least stable. Since the regime was first observed, H-modes have been developed on many machines and under many different operating conditions (Hawryluk et al, 1986; Carolan et al, 1994; Fielding et al., 1996; Gormezano, 1999).

The key to the success of the H-mode is the edge transport barrier or confinement barrier; a region of steep temperature and density gradient that is formed close to the plasma edge (Fujita, 2001). Figure 2.1 shows electron density profiles over a transition from L-Mode to H-mode on the ASDEX Tokamak (Wagner et al, 1990). As can be seen, there is a clear increase in the density gradient at the edge of the plasma and a *knee* is formed in the density profile. The characteristic shape is known as a *pedestal* and such pedestals have been shown to form during H-modes in both the density and temperature profiles (Groebner and Osbourne, 1998).

There is a specific type of instability associated with H-modes. Edge Localised Modes (ELMs) (Zohm, 1996; Connor, 1998; Fielding et al., 2001) are short, repetitive perturbations in the edge region, leading to loss of particles and energy. ELMs are problematic for tokamak physicists because they degrade the confinement barrier and can cause damage to plasma-facing hardware. Of particular concern are the high energy fluxes at surfaces which come into contact with the plasma, which would shorten the life of limiter and divertor plates if left uncontrolled (Loarte et al., 2000). According to Osbourne et al. (1997), the energy loss from the plasma for the largest

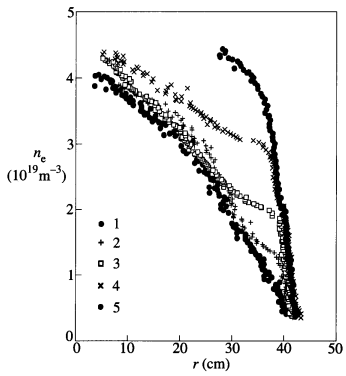

(a) *Time Sequence of density profiles measured around the transition from L- to H- mode.*

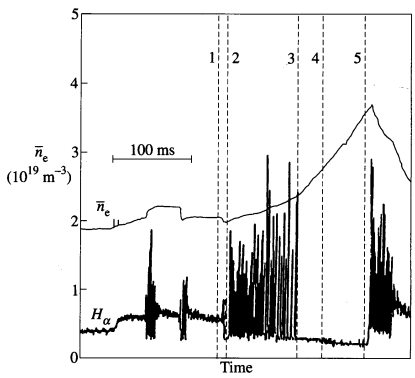

(b) *D_α emission and average density. The dotted lines refer to the times at which the density profiles in (a) were measured.*

Figure 2.1: *The transition from L- to H-mode as shown by Wagner et al (1990).*

type of ELM (type I) scales as,

$$\frac{\Delta E_{\text{ELM}}}{E_{\text{TOTAL}}} \propto \frac{P}{S}^{-0.4} B^{-0.3}, \tag{2.2}$$

where P is the total input power and S is the plasma surface area. The loss of energy from ITER, the planned future *International Tokamak Experimental Reactor* would be,

$$\Delta E_{\text{ELM}} \approx 26MJ.$$

Infrared camera measurements by the same author suggest that $75\% - 100\%$ of the energy losses would be deposited on the divertor plates in a time-scale of $1 - 2ms$, making an average power deposition of $\approx 1.7 \times 10^4 MW$ over that initial period.

It is thought by some that ELMs may have some redeeming features (Burrell et al, 1989; Vollmer et al., 1990; Thomas et al., 1992; Naito and the JT-60 team, 1993). The exhaust of particles from the edge region could be of some use in controlling densities, especially of impurity ions and helium ash. These impurities could reduce re-activity and cause the plasma to *choke*. For these reasons, controlling the type and frequency of ELMs is of the utmost importance.

In pursuit of the goal of ELM control, several authors have contributed to models and descriptions of how ELMs may be caused and how they might develop (Snyder et al., 2002; Wilson et al., 2001; Igitkhanov et al., 2002).

2.2 The phenomenology of ELMs

2.2.1 MHD ELM types

The first classification of ELM phenomena was given for the DIII-D tokamak (Doyle et al., 1991). Three distinct types of ELM were numbered in the order in which they were discovered.

Type I ELMs

Type I or giant ELMs are the most undesirable. They are large, regular bursts of MHD activity which result in large heat loads to the divertor or limiter plates. These giant ELMs could well be intolerable in a large tokamak device. They are most easily distinguished because the ELM frequency increases with input power (Doyle et al., 1991). They appear at high input power levels, often after a period of ELM-free H-mode.

Type I ELMs appear to be connected with a normalised edge pressure gradient, α (Gohil et al, 1988), which is calculated from the pressure gradient averaged over a flux surface and normalised to the average pressure. The correct value must be calculated numerically, taking account of plasma shaping and finite aspect ratio effects. For this reason, a large aspect ratio, circular cross-section approximation is commonly used and is given by,

$$\hat{\alpha} = -\frac{2\mu_0 R q^2}{B^2}\frac{\mathrm{d}p}{\mathrm{d}r}. \tag{2.3}$$

In the above, R is the tokamak major radius, q is the safety factor, B is the magnetic field, and dp/dr is the radial derivative of the plasma pressure. The origin of this term is explored in section 2.4.3. The review article by Connor (1998), noted that there is a critical value of α, known as the ideal ballooning limit (α_{cr}). The ballooning limit, α_{cr} can be calculated for a plasma with cylindrical cross-section, however it is found that α_{cr} is sensitive to the geometry of the plasma and so a numerical code is required to calculate α_{cr} for practical purposes. Merely reaching α_{cr} does not necessarily trigger the ELM. On JET, studies that have traced α over the time leading up to Type I ELMs have found that the plasma can remain at α_{cr} for some time before the ELM is initiated (Lingertat et al., 1997). Scaling studies on ASDEX-U also found that the plasma reaches α_{cr} and can remain at the limit for some time before an ELM commences (Kass et al., 1997). The team at JT-60U, in Japan, have also corroborated this result (Kamada et al., 1994). The success of these experiments means that on certain tokamaks, it is possible to experimentally measure α_{cr}, under

certain conditions. The triangularity δ has been varied $(-0.06 < \delta < 0.4)$ and it has been found that the observed α_{cr} varies according to its dependence on δ as predicted by numerical modelling (Lingertat et al., 1997). The evidence suggests that the ideal ballooning mode is a limiting factor to the pressure gradient but not, by itself, the trigger for the ELM. Two candidate explanations suggest themselves. A transient flow of heat or anomalous diffusion of pressure to the edge region might force a sudden increase in α, causing a strong, explosive instability (Hurricane et al., 1997). Alternatively, the ballooning mode might limit α until such time as the edge current density ($j_{\|}$) evolves upwards due to a fall in collisionality, to trigger the peeling mode, which is a current-driven edge instability (Igitkhanov et al., 2002). A further discussion on these two possibilities is given in section 2.4.3. The peeling mode will be described in more detail in section 2.4.4.

Type II ELMs

Type II ELMs, sometimes called *grassy* ELMs, are only observed on a few large machines including ASDEX-U and DIII-D (Wagner et al, 1982; Doyle et al., 1991). They are brought about by increasing the elongation and triangularity of a plasma which is displaying type I ELMing behaviour. Type II ELMs generally have a higher frequency than type I ELMs for a given input power but are of smaller magnitude, a feature which might make them useful as a means of avoiding excess heat loading to plasma-facing vessel components like divertor plates. It is thought that the increase in triangularity and elongation can give access to a region of so-called *second stability* (Snyder et al., 2002) to the ballooning mode and it is in this region that type II ELMs are observed (Ozekiet al, 1990).

Type II ELMs only occur in highly shaped plasmas at low s/q^2, corresponding to access to second stability where s (shear) is defined as,

$$s = \frac{r}{q}\frac{\mathrm{d}q}{\mathrm{d}r}. \tag{2.4}$$

In the above, q is the safety factor, (section 1.3.3). Shear is a measure of how much the pitch of the magnetic field lines changes with respect to radius. High shear is generally stabilizing as it increases the amount of energy required to perturb the magnetic field lines. Studies on DIII-D including Osbourne et al. (1997), have shown that at low s/q^2, α can exceed α_{cr}. This result implies that low shear may result in a change in the equilibrium that results in a suppression of the ideal ballooning mode (section 2.4.3). This change equilibrium might allow access to the second region of stability, where type II ELMs are found.

Type III ELMs

Type III ELMs have been observed on all tokamaks that have achieved H-mode. Examples of work that has been published concerning them are (Kass et al., 1997; Fielding et al., 2001; Pogutse et al., 1999). Type III ELMs are smaller and therefore less damaging than their Type I counter-parts but are still somewhat problematic. Like all ELMs, they lead to a lowering of the edge temperature gradient. Unlike, Type I and type II ELMs, type III ELMs are observed at relatively low input power levels, often prior to a period of ELM-free H-mode (Fielding et al., 1996). They are also notably different as their frequency decreases with input power but their magnitude tends to increase. In keeping with this observation, it has been shown that that sawtooth heat pulses (Levinton et al., 1994), which increase the power through the separatrix, can stabilise type III ELMs.

On the ASDEX-U tokamak, type III ELMs are observed below a certain critical temperature $T_e < 300eV$. This observation suggests that resistivity in the plasma core and therefore the current profile, may play some role in the event. They can also be induced by radiative cooling which cools the edge, increasing its resistivity (Kass et al., 1997).

According to the original DIII-D classification, type III ELMs occur at $0.3 < \alpha/\alpha_{cr} < 0.5$ but analysis as reported by Osbourne et al. (1997), shows that there are in fact two subtypes of the type III ELM; one at high average density $(\bar{n}_e)$ and the other at low average density. The high density type III ELMs disappear above a certain critical temperature, which implies that they can be stabilised by decreasing resistivity. This is in agreement with the work by Kass et al. (1997) described above.

The low density type III ELMs, disappear above a critical value of α which scales as the plasma current squared, I^2. In global parameters, this manifests as a maximum input power,

$$P_{cr} \propto \frac{I_p^{2.4}}{\bar{n}_e^2}, \tag{2.5}$$

where $\bar{n}_e$ is the average electron density. This observation implies that the pressure gradient may be important in stabilizing these ELMs. The importance of these results and how they can be interpreted in light of one of the leading ELM models, will be shown in section 2.6.

2.2.2 Other ELM types

The number nomenclature has been widely adopted throughout the tokamak community and it will be used in this work from this point onwards. In addition to the three numbered types, there are two less frequently discussed types of ELM. The two final ELM types are different to the above mentioned three as they are not primarily MHD events. They are included here for completeness but will be excluded from the rest of this discussion.

Dithering ELMs

Dithering ELMs or dithering H-mode refers to rapid transitions between L- and H-Mode. An example is given by Valovic et al. (1994) for COMPASS-D. The distinction is made between MHD-ELMs and L-H ELMs; MHD-ELMs being the type III ELMs mentioned above and L-H ELMs being dithering ELMs.

Compound ELMs

A type III ELM followed by a short period of L-mode is described as a compound ELM. They were first observed in the ASDEX-Upgrade tokamak (Wagner et al, 1982), and lasted $\approx 5 - 10ms$.

2.3 ELMs on COMPASS-D

The *classical* H-mode evolution is as follows: 1. L-mode gives way to type III ELMy H-mode. The ELMs increase in size but decrease in frequency as the input power is increased. The transition to H-mode is usually accompanied by a sharp drop in the D_α signal. 2. Type III ELMy H-mode is followed by a period of ELM-free H-mode. 3. Finally, type I ELMs are observed, which increase in frequency as input power continues to increase.

COMPASS-D never clearly displayed this behaviour, despite increases in ECRH heating power of up to a factor of four after an L-H transition (Fielding et al., 1988). The transition into H-mode is not accompanied by a sharp drop in D_α and the so onset of H-mode is defined as being the first appearance of ELMs, which generally grow in size and decrease in frequency as input power is increased until a transition into ELM-free H-mode occurs.

An example of a typical D_α trace from an Ohmic H-mode can be seen in figure 2.2, plotted along with poloidal velocity by Fielding et al. (1996). As can be seen,

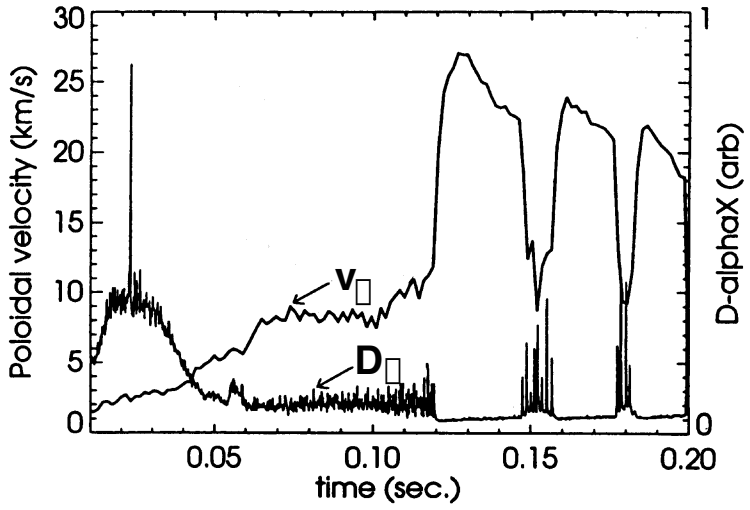

Figure 2.2: *Time history of D_α emission and poloidal rotation of carbon (C^{2+}) ions for Ohmic H-mode discharge number 16000. Notice how the D_α trace shows type III ELMs evolving slowly with no clear transition until ELM-free H-mode at $0.12s$. The second set of ELMs were originally thought to be type I but may, in fact, be large type III ELMs.*

after some period of ELM-free H-mode, COMPASS-D displays periods of large regular ELM activity which were originally identified as type I ELMs, (Colton et al., 1996). In the light of the analysis by Osbourne et al. (1997) and because of uncertainties in the frequency scaling with input power, it is thought that these two types of ELMs may be the *small* and *large* sub-classes of type III ELMs mentioned in the previous section (Connor, 1998).

2.4 ELM Physics

Connor (1998) and Zohm (1996) present useful and comprehensive reviews of the various types of ELM theory. This section will contain a brief introduction to edge localised instabilities followed by a more in-depth review of two particular instabilities; the ballooning mode (Connor et al., 1978), which is driven by pressure gradients, and the peeling mode (Manickam, 1992), which is driven by current density gradients. Both of these instabilities were mentioned in section 2.2 as having particular relevance to ELM physics. As will be seen, the particular model of stability presented will have implications for both ELMs and H-mode access.

2.4.1 MHD stability

The general method for finding the conditions for stability for a given equilibrium is to derive an equation for the change in potential energy (δw) as a result of any physically allowable perturbation. If the perturbation to an equilibrium leads to a lowering of the potential energy, then the equilibrium is unstable. This method is referred to as the energy principle (Bernstein et al., 1958).

The energy principle can sometimes be used directly to obtain a criterion for stability by arranging the terms of δw in a form that, when the criterion is satisfied, δw will always be negative for all displacements. More commonly, it is necessary to use a trial function to make δw negative and hence demonstrate instability. By minimizing the energy principle, it is often possible to find points at which $\delta w = 0$ and thereby find curves of marginal stability for a variety of instabilities. Although beyond the scope of this review of ELM physics, the derivations of the energy principles and their minimisations were performed for the ballooning and peeling modes by Connor et al. (1978) and Connor et al. (1998).

2.4.2 Localised Modes

There are many types of instability, with varying characteristics. Two important defining features are the mode numbers, which are the number of wavelengths in single poloidal and toroidal circuits of the torus (m and n, respectively). The stabilizing effect of the magnetic tension brought about by perturbing the magnetic field lines is minimised when the mode numbers match the helix of the magnetic field lines, *i.e.* $m = nq$ where q is the safety factor (section 1.3.3). This condition is known as resonance and a particular mode may have one or more resonant surfaces within a plasma.

High n modes tend to be more strongly stabilised by field line bending and therefore more strongly peaked around their resonant surface. In the limit of $n \rightarrow \infty$, the number of resonant surfaces becomes infinite and the distance between them becomes zero. The $n \rightarrow \infty$ limit allows theorists to assume that a mode is localised to a single surface of ψ. Stability can then be treated as a surface property.

2.4.3 The ballooning mode

The ballooning mode was originally described by Coppi and Rosenbluth (1965) and the mathematical formalisation was performed by Connor et al. (1978). The ballooning mode is a pressure driven localised mode, resonant on $n^{1/2}$ rational surfaces, that

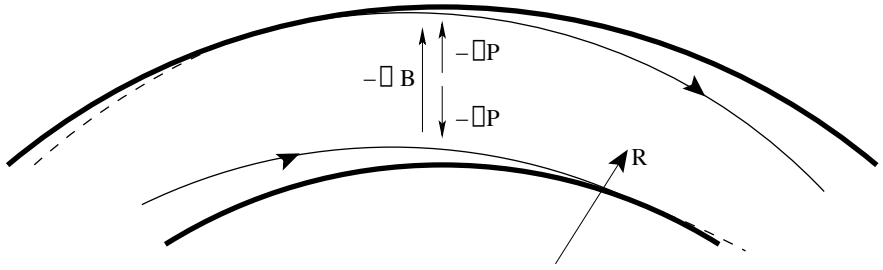

Figure 2.3: *Plan view of a section of a torus. The curvature of the B-field is stabilizing on the inboard side of the torus and destabilizing on the outboard side.*

was originally formulated for the plasma core. One of the most important features of the ballooning mode is the effect on stability of the average curvature of the magnetic field. The curvatures of the field lines change sign from the inboard to the outboard side with respect to the curvature of the surfaces of constant kinetic pressure.

An understanding of how magnetic curvature affects stability is aided by figure 2.3. In this plan view of a torus, we can see how on the inboard side, the gradient in magnetic field points in the opposite direction to the gradient in kinetic pressure. Force balance is given by,

$$\boldsymbol{F} = \frac{\boldsymbol{B}\cdot\boldsymbol{\nabla}\boldsymbol{B}}{\mu_0} - \boldsymbol{\nabla}\left(p + \frac{B^2}{2\mu_0}\right) = 0. \tag{2.6}$$

Since the majority of the magnetic field is toroidal and falls off as $1/R$, the magnetic tension term, $\boldsymbol{B}\cdot\boldsymbol{\nabla}\boldsymbol{B}$ can be simplified to

$$\boldsymbol{B}\cdot\boldsymbol{\nabla}\boldsymbol{B} \approx \boldsymbol{B_\phi}\cdot\boldsymbol{\nabla}\boldsymbol{B_\phi} = \frac{B_\phi^2}{R}\left(-\hat{\boldsymbol{e}}_{\boldsymbol{R}}\right) \tag{2.7}$$

where $\hat{\boldsymbol{e}}_{\boldsymbol{R}}$ is a unit vector in the major radius direction. The magnetic tension force points inward along the major axis on both the outboard and inboard side, whereas the kinetic pressure term $-\boldsymbol{\nabla}p$ points outward on the outboard side and inwards on the inboard side. The force balance is maintained by the magnetic pressure term, $\boldsymbol{\nabla}B^2/2\mu_0$. This asymmetry leads to the phenomena of good and bad magnetic curvature.

Figure 2.4 shows a perturbation whereby plasma is pushed outwards along the minor radius. If the *finger* of plasma is thin, there will be pressure balance across it, which will lead to a weakening of the magnetic field. The weakening of the magnetic field can be related to the displacement of the perturbation by comparing the kinetic

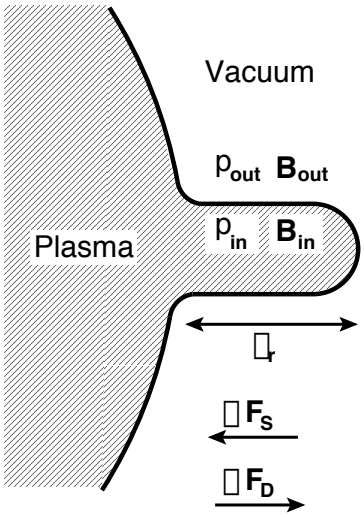

Figure 2.4: *The Mechanism of the ballooning instability. A finger of plasma extends out into a lower kinetic pressure region. The pressure balance across the magnetic field leads to a weakening of the magnetic tension and is the driving force of the instability.*

and magnetic pressure inside the *finger* to that outside,

$$P_{in} - P_{out} = \frac{B_{out}^2}{2} - \frac{B_{in}^2}{2}, \tag{2.8}$$

$$= \frac{1}{2}(B_{out} - B_{in})(B_{out} + B_{in}), \tag{2.9}$$

$$\boldsymbol{\xi} \cdot \boldsymbol{\nabla} p = \delta B_{\|} B. \tag{2.10}$$

Note that the kinetic pressure inside the *finger* is assumed to not have changed due to the perturbation. This assumption is valid if the plasma is incompressible, hence only for high-β discharges.

The magnetic field weakening causes a loss of magnetic tension. Since the magnetic tension force points inwards along the major radius, a drop in the tension force on the outboard side is destabilizing. The effect is rather like over-inflating a balloon, the more the surface is stretched, the weaker the restoring force and so the perturbation grows exponentially, which is why the outboard side is said to have bad magnetic curvature. A reduction in magnetic tension on the inboard side is stabilizing and so the inboard side is said to have good magnetic curvature.

In the ballooning mode, the perturbation is minimised on the inboard side. In order to achieve this, the magnetic field lines must be *bent back* onto the unperturbed magnetic surface. This bending requires extra force and is therefore a stabilizing

influence on the ballooning mode.

Figure 2.5 is a schematic representation of the ballooning mode. A field line is *pushed out* of the plasma resulting in a *finger*-like perturbation of plasma that can be seen protruding into the vacuum region. On the outboard side, the displacement is largest. Note that the magnitude of the displacement varies slowly, allowing for it to be minimised on the inboard side.

The full mathematical treatment of ballooning stability is given by Connor et al. (1978) but is beyond the scope of this review. A crude stability criterion for the ballooning mode can be obtained by comparing the change in magnetic tension force, as a result of the field weakening expressed in equation 2.10, to the extra force required to bend the field lines back into the unperturbed magnetic surface on the inboard side.

The change in tension force caused by introducing a small change in $\boldsymbol{B}$ to the first term in equation 2.6 is given by,

$$\delta \boldsymbol{F} = \frac{\delta \boldsymbol{B} \cdot \boldsymbol{\nabla} \boldsymbol{B}}{\mu_0} + \frac{\boldsymbol{B} \cdot \boldsymbol{\nabla} \delta \boldsymbol{B}}{\mu_0}. \tag{2.11}$$

The value for $\delta \boldsymbol{B}$ can be found by combining a corollary of the Lorentz equation,

$$\boldsymbol{E} = -\boldsymbol{v} \times \boldsymbol{B}, \tag{2.12}$$

where v is the velocity of a positively charged particle, with Faraday's Law,

$$-\frac{\partial \boldsymbol{B}}{\partial t} = \boldsymbol{\nabla} \times \boldsymbol{E}. \tag{2.13}$$

The result is integrated to yield,

$$\delta \boldsymbol{B} = \boldsymbol{\nabla} \times (\boldsymbol{\xi} \times \boldsymbol{B}), \tag{2.14}$$

which can be expanded to give,

$$\delta \boldsymbol{B} = \boldsymbol{B} \cdot \boldsymbol{\nabla} \boldsymbol{\xi} - \boldsymbol{\xi} \cdot \boldsymbol{\nabla} \boldsymbol{B} - \boldsymbol{B} (\boldsymbol{\nabla} \cdot \boldsymbol{\xi}). \tag{2.15}$$

The first term on the right hand side of the above equation is perpendicular to $\boldsymbol{B}$. It is in this term that the extra force required to minimise the perturbation on the inboard side must be included. The second term is a small magnetic field convection term which can be ignored. The third term, which is purely parallel to $\boldsymbol{B}$, is where the force due to the loss of magnetic tension can be included. Since the third term represents the parallel component of the change in the $\boldsymbol{B}$-field, it can be replaced with $\boldsymbol{B}(\delta B_{\parallel}/B)$. The equation now becomes,

$$\delta \boldsymbol{B} = \boldsymbol{B} \cdot \boldsymbol{\nabla} \boldsymbol{\xi} - \boldsymbol{\xi} \cdot \boldsymbol{\nabla} \boldsymbol{B} - \boldsymbol{B} \left(\frac{\delta B_{\parallel}}{B} \right). \tag{2.16}$$

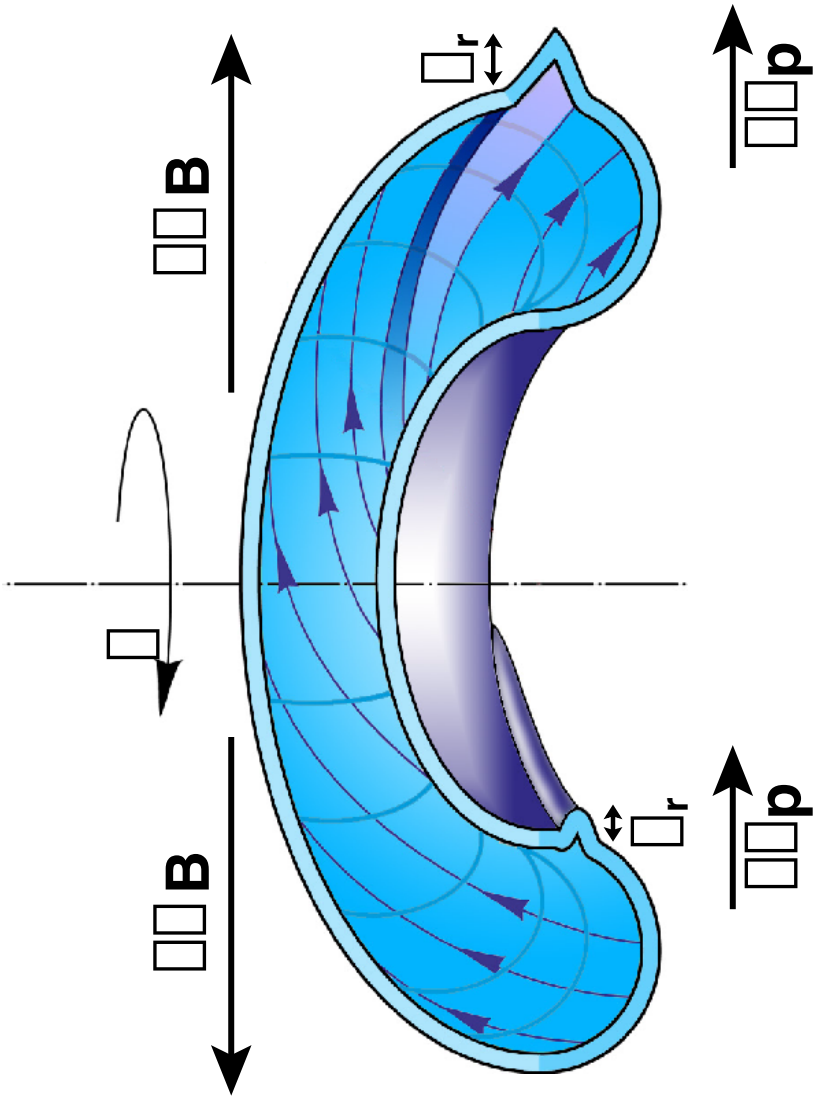

Figure 2.5: *A representation of a ballooning instability. A field line is pulled out of the plasma, forming a* finger*-like perturbation that varies in amplitude slowly along the field line. The perturbation balloons out on the outboard side and is minimised on the inboard side. Thanks to Steve Cowley.*

To calculate the change in force on the element of perturbed plasma due to the bending of the field lines back onto the unperturbed surface, the first term of equation 2.16 can be substituted into equation 2.11 to give,

$$\delta \boldsymbol{F_S} = \frac{(\boldsymbol{B}\cdot\boldsymbol{\nabla}\boldsymbol{\xi})\cdot\boldsymbol{\nabla}\boldsymbol{B}}{\mu_0} + \frac{\boldsymbol{B}\cdot\boldsymbol{\nabla}\left(\boldsymbol{B}\cdot\boldsymbol{\nabla}\boldsymbol{\xi}\right)}{\mu_0}. \tag{2.17}$$

In the above, $\delta \boldsymbol{F_S}$ is the stabilizing contribution to the final force balance. This can be simplified to give roughly,

$$\delta \boldsymbol{F_S} \sim \frac{-B^2}{\left(\mu_0 q R\right)^2}\boldsymbol{\xi_r}, \tag{2.18}$$

where $\boldsymbol{\xi_r}$ is the radial displacement of the perturbation in the $-\boldsymbol{\nabla}p$ direction. The above field line bending term is always stabilizing as it points inwards along the minor radius.

Substituting the third term of equation 2.16 into equation 2.11 gives the change in force as a result of the reduction in parallel magnetic field. That is,

$$\delta \boldsymbol{F_D} = \frac{1}{\mu_0}\frac{\delta B_\parallel}{B}\boldsymbol{B}\cdot\boldsymbol{\nabla}\boldsymbol{B} + \frac{1}{\mu_0}\boldsymbol{B}\cdot\boldsymbol{\nabla}\left(\frac{\delta B_\parallel}{B}\boldsymbol{B}\right). \tag{2.19}$$

Taking only the component across the field lines, in the direction of $\boldsymbol{\xi_r}$, gives,

$$\delta \boldsymbol{F_D} \sim \frac{2}{\mu_0}\frac{\delta B_\parallel}{B}\boldsymbol{B}\cdot\boldsymbol{\nabla}\boldsymbol{B}. \tag{2.20}$$

Thus, if the field is weakened in the *finger* ($\delta B_\parallel < 0$), the perturbed force is in the opposite direction to the equilibrium curvature force, *i.e.* outwards along the major radius.

Equations 2.10 relates the change in magnetic field to the equilibrium pressure gradient and radial displacement. Equation 2.7 shows the magnetic tension force to always be directed inwards along the major radius. Substituting these two equations into equation 2.20 gives the approximation,

$$\delta \boldsymbol{F_D} \sim \frac{-2}{\mu_0 R}\left(\boldsymbol{\xi_r}\cdot\boldsymbol{\nabla}p\right)\,\hat{\boldsymbol{e}}_{\boldsymbol{R}}. \tag{2.21}$$

For a displacement outwards along the minor radius $\boldsymbol{\xi_r}\cdot\boldsymbol{\nabla}p < 0$. The corollary being that, $\delta \boldsymbol{F_D}$ always acts outwards along the major radius, that is outwards along the minor radius on the outboard side and inwards along the minor radius on the inboard side. $\boldsymbol{F_D}$ is the ballooning force that is destabilizing on the outboard side and stabilizing on the inboard side.

By comparing equations 2.18 and 2.21, a simple criterion for ballooning stability is found

$$1 < -\frac{2\mu_0 R q^2}{B^2}\frac{\mathrm{d}p}{\mathrm{d}r} = \hat{\alpha} \tag{2.22}$$

For low pressure discharges, the favorable magnetic curvature, on the inboard side, is sufficient to stabilise the mode, despite the adverse magnetic curvature on the outboard side, provided that $q > 1$. In higher pressure discharges, the perturbation becomes concentrated to the region of adverse magnetic curvature and the potential energy released by the displacement can be larger than that required to bend the field lines. Under these circumstances, the magnetic curvature can no longer protect the stability of the plasma. The magnetic field lines bulge or balloon on the outboard side, hence the name, *ballooning*.

The ballooning mode is potentially self limiting. That is to say, a key part of the mechanism relies on a steep kinetic pressure gradient across the *finger* of plasma. This steep gradient, as well as leading to the weakening of the magnetic field in that region, will cause a diffusive flow of plasma from the inside to the outside of the *finger*. If this flow is strong enough to reduce the pressure gradient, the plasma can be stabilised and the instability is self limiting. On the other hand, if the *finger* of plasma is too thick or the instability is growing too quickly, the loss of plasma will not be sufficient to stabilise the plasma. In the first case, the ballooning mode can be thought of as a soft limit, in which the plasma is held at the ballooning limit until such time as the edge current density rises and the plasma becomes unstable to the peeling mode. In the second case, it can lead to explosive loss of confinement at the edge.

2.4.4 The peeling mode

The peeling mode was first identified by Manickam (1992) who showed numerically, that an $n = 1$, mode with mixed m numbers could be excited by increasing the plasma edge current density. The mode is a highly localised kink and resonant in the vacuum, with its corresponding rational surface close to the plasma surface so that the stabilizing effect associated with bending the magnetic field lines in the vacuum is negligible (Lortz, 1975). The mode can be anti-ballooning, that is the maximum amplitude of the mode being on the high field side, contrary to the effects of magnetic curvature (Huysmans et al., 1992). This is because the main driving force for the peeling mode is current density shear which can be larger on the inboard than

outboard side. A stability criterion is given by Connor (1998);

$$\sqrt{1-4D_M} > 1 + \frac{2}{2\pi q'} \oint \frac{j_\parallel B}{R^2 B_p^3}\, dl_\theta, \tag{2.23}$$

where dl_θ is the poloidal arc length element and D_M is the Mercier coefficient,

$$D_M = \left(q^2 - 1\right) \left(\frac{q}{q'}\right)^2 \frac{2\mu_0 p'}{r B_\phi^2}. \tag{2.24}$$

The Mercier coefficient is found by rearrangeing the Mercier criterion, which was originally derived by Mercier (1960).

The most important aspect of equation 2.23 is that the integrand is proportional to the parallel current and therefore parallel current is destabilizing. Equation 2.24 tells us that the Mercier coefficient is proportional to the pressure gradient, suggesting that the peeling mode can be stabilised by a pressure gradient. On the other hand, the pressure gradient can drive currents which must be accounted for in equation 2.23. The bootstrap current (section 1.4.1) runs parallel to the magnetic field and is destabilizing (Wilson et al., 1999). The effect of the Pfirsch-Schlüter current (section 1.4.2) is more subtle, the current runs parallel to the field on the outboard side, thereby destabilizing the plasma but anti-parallel on the inboard side, detracting from the bootstrap current and stabilizing the plasma. The role of the Pfirsch-Schlüter current requires careful evaluation of the flux surface integral (Connor et al., 1998).

2.4.5 Stability boundaries

A theoretical study of stability boundaries and their implications for ELM cycles has been presented in a series of papers by Connor et al. (1998), Wilson et al. (1999) and Snyder et al. (2002).

As a useful first order approximation to a stability model, marginal stability curves for the $n = \infty$ approximation to the peeling and ballooning modes in s and α space were calculated by Connor et al. (1998). the results are shown in figure 2.6. The ballooning mode, which is shown by the solid line is pressure driven, and so limits the achievable value of α. The peeling mode, which is current driven is stabilised at high shear (s), since,

$$2 - s = \frac{2 j_\parallel}{\langle j \rangle}, \tag{2.25}$$

where $j_\parallel / \langle j \rangle$ is the normalised edge current density. The result is a stability triangle of high shear and low pressure gradient for any given flux surface.

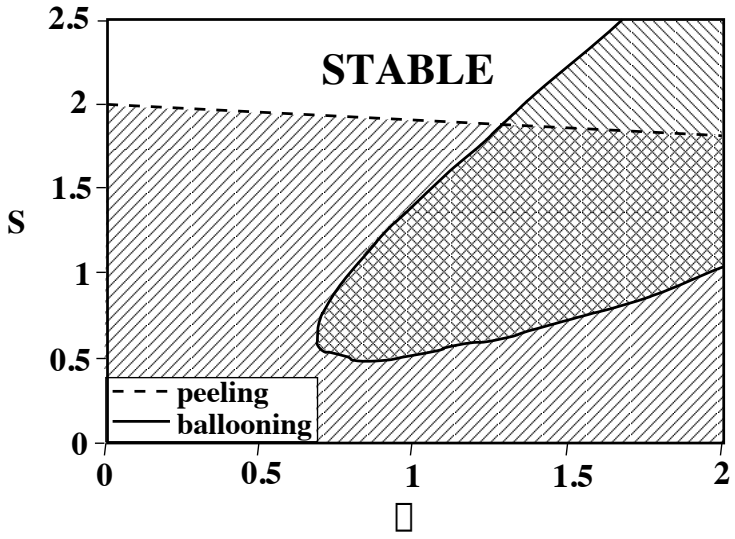

Figure 2.6: *The ballooning (solid line) and peeling (dashed line) marginal stability contours in $s - \alpha$ space, (Connor, 1998).*

The shapes of these curves are dependant on various plasma parameters, most particularly, plasma shaping. For highly shaped plasmas, it is possible for the two unstable regions not to overlap, allowing access to so-called second stability. This result agrees with the observations of type II ELMs reviewed in section 2.2.

The full solution to the edge stability problem was shown in the same series of articles. A numerical code called ELITE, which was originally developed by Howard Wilson at UKAEA analyses stability throughout any region of the plasma. ELITE calculates the growth rates for the ideal eigenmodes of the equilibrium, using the pressure and current density gradients as the sources of free energy. Any given eigenmode can be stable or unstable. If the growth term is positive, then the mode is unstable. ELITE can fourier decompose the resulting eigenmodes by assuming them to be harmonic in the toroidal and poloidal directions. The decomposition takes the form,

$$\xi_r\left(\psi,\theta,\phi\right) = e^{in\phi}\sum_m u_m(\psi)\, e^{-im\theta}. \tag{2.26}$$

Figure 2.7 shows a typical output from the ELITE code. The abscissa is defined as $x = m_0 - nq$, where m and n are mode numbers and q is the safety factor. Integer values of x refer to successive rational q surfaces, counting in from the separatrix, where m_0 is the closest rational surface to the separatrix. Each fourier harmonic of the eigenmode is shown as a separate line. The harmonics that are resonant inside

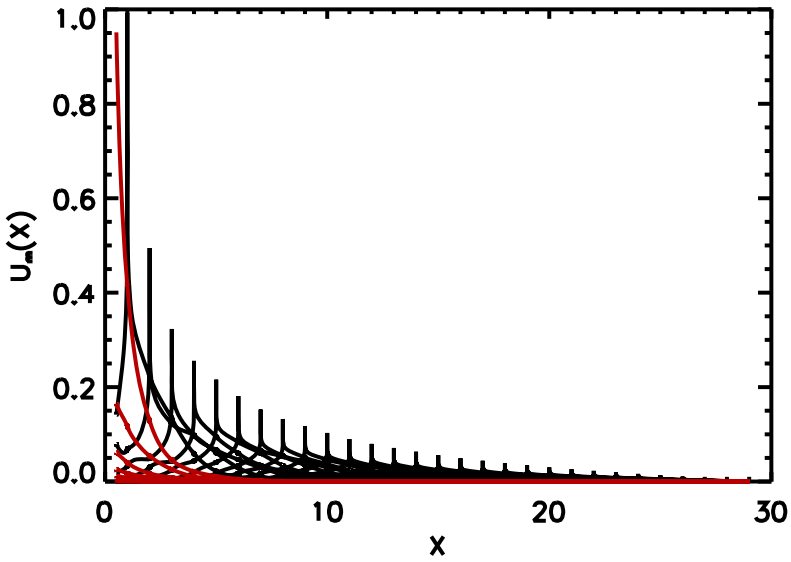

Figure 2.7: *The radial component of the fourier harmonics of a given eigenmode as generated by the ELITE stability code. Each harmonic peaks at a different rational surface (X). Those harmonics resonant outside the plasma are shown by red curves.*

the plasma are shown as black lines, those resonant outside the separatrix are shown in red. It can be seen that each harmonic peaks at a different rational surface. These are the resonant surfaces for each harmonic and the peaking occurs because the mode numbers are such that the field lines do not need to bend to allow m/n of the instability to match the pitch of the field lines. The minimisation of field line bending is the origin of the resonance phenomena.

Further insight can be gained from referring back to equation 2.26. The poloidal term, $e^{-im\theta}$, simplifies to 1 on the outboard side, where $\theta = 0$. On the inboard side ($\theta = \pi$), $e^{-im\theta}$ alternates between 1, and -1 for even and odd values of m, respectively. The ballooning mode is considered to be more radially extended into the plasma, than the peeling mode (Snyder et al., 2002). One corollary of the radial extension of the mode is that the difference in height between successive peaks would be smaller than if the mode were more localised. Since the poloidal term of equation 2.26 switches between 1 and -1 between successive rational surfaces on the inboard side, the radial displacement associated with the eigenmode is minimised on the inboard side. For a more edge localised mode, like the peeling mode, this argument does not apply since the difference in amplitudes of successive peaks is much greater. The conclusion is that radially extended edge modes are ballooning in nature, whereas highly localised modes are not.

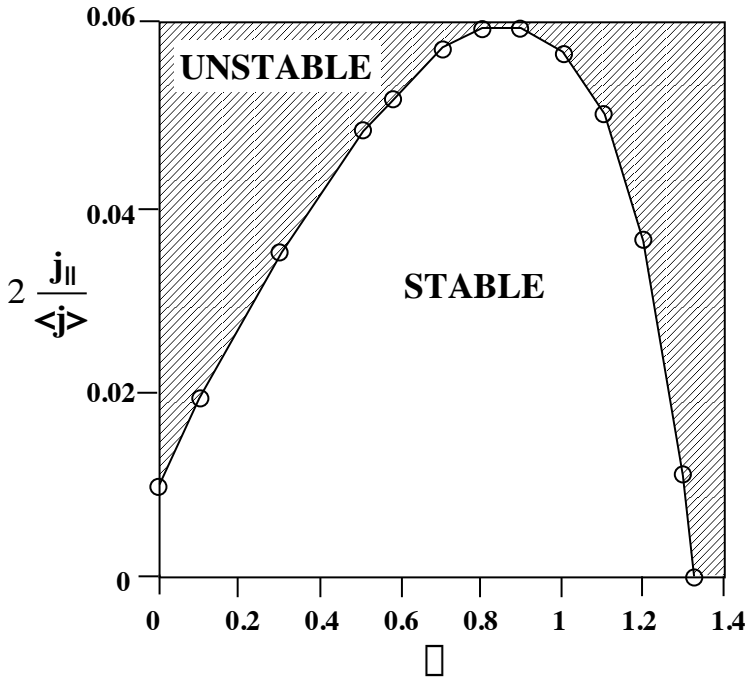

Figure 2.8: *Marginally stable normalised edge current density as a function of edge pressure gradient.*

Connor et al. (1998) abandons the use of s at this point in favor of $2j_{\|}/\langle j\rangle$, as it is a more intuitive parameter. Figure 2.8 shows the results from a numerical calculation showing the normalised edge current density for marginal stability as a function of the normalised edge pressure gradient for a particular rational surface in an equilibrium. There are two solutions of α for each value of $2j_{\|}/\langle j\rangle = 2 - s$. One of which, the lower, corresponds roughly to the peeling boundary while the upper value is just lower than the ballooning boundary. This observation was in quantitative agreement with earlier studies done with simpler models (Wilson and Connor, 1997; Hegna et al., 1996). Analytical results, like the one shown in figure 2.6 are a fairly good approximation to the full numerical solution except for the fact that the peeling and ballooning modes couple at high normalised edge current density, which reduces the size of the stable region by *rounding off* the top corner of the stable *triangle*. Again, this effect was predicted in the earlier studies.

2.5 H-mode access

Connor et al. (1998) presents an argument regarding the relationship between H-mode and collisionality. At low collisionality, the plasma is in banana regime. In this regime, the pressure gradient drives the bootstrap current, which is parallel to the $\boldsymbol{B}$-field and so destabilises the peeling mode (section 1.4.1). A schematic representation of the peeling and ballooning boundaries is shown in figure 2.9a. The above described trajectory is also shown.

It is argued that stability can be achieved by increasing collisionality to the point where the fraction of trapped particles is small, that is $\nu_e^* \gg 1$. The destabilising bootstrap current is much reduced in favor of the Pfirsch-Schlüter current (section 1.4.2) which is antiparallel to the $\boldsymbol{B}$-field on the inboard side and is therefore stabilizing. Figure 2.9b shows this trajectory. Further discussion of this diagram and how it describes type I ELMs is presented in the next section.

Figure 2.10 shows data from COMPASS-D (Field et al., 1999b). It can be seen that access to H-mode correlates with high ν_e^*, as predicted by the model. It can also be seen that ELMs generally occur around $\nu_e^* \approx 1$.

2.6 ELM cycles

A description of the expected trajectory of plasmas during inter-ELM periods is presented by Snyder et al. (2002). Assuming that access to H-mode is achieved due to

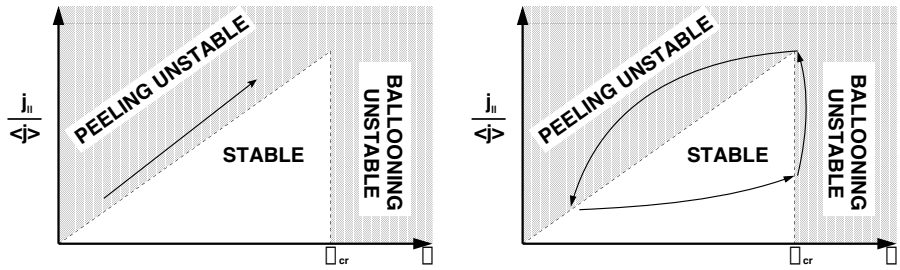

(a) *In the banana regime with low collisionality, $j_\parallel / \langle j \rangle$ rises along with α.*

(b) *At higher collisionality, the bootstrap current is much lower allowing access to H-mode. If ν_e^* falls, $j_\parallel / \langle j \rangle$ will increase and a coupled peeling-ballooning results in a type I ELM.*

Figure 2.9: *Schematic stability diagrams showing the peeling and ballooning boundaries in $j_\parallel / \langle j \rangle$ (normalised edge current density) - α (normalised edge pressure) space. The trajectories of discharges in different regimes is also shown.*

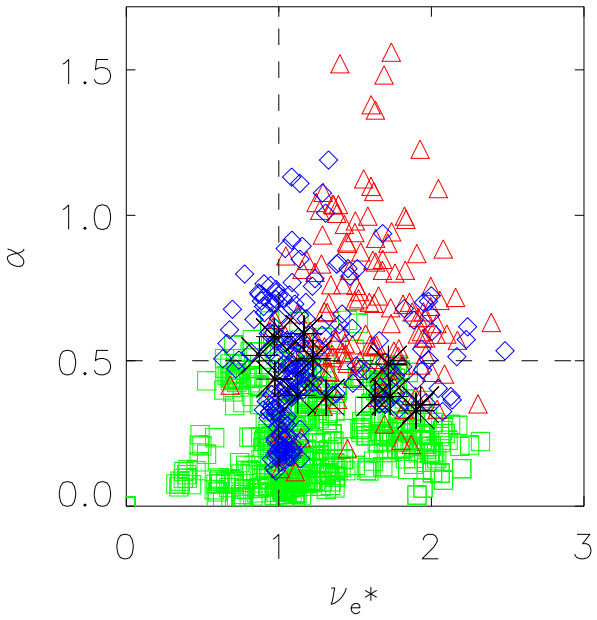

Figure 2.10: *Data from COMPASS-D showing the distribution of L- and H-mode discharges against measurements of α and normalised electron collisionality ν_e^* taken with HELIOS. □ = L-mode, △ = H-mode with no ELMs occurring during the measurement, ◇ = H-mode with an ELM occurring during the measurement.*

high edge collisionality suppressing the bootstrap current, α could rise until the ballooning limit was reached. If the collisionality drops after access to H-mode, then $j_{\|}/\langle j \rangle$ would rise and the peeling mode would become unstable. Figure 2.9b shows how this situation would result in an H-mode with type I ELMs caused by coupled peeling-ballooning modes.

A striking feature of the above described model is the way in which it fits in with the observations of Type I ELMs on several Tokamaks. Reviewing section 2.2.1, it was noted that for type I ELMy plasmas, the pressure gradient is frequently observed to rise to the critical ballooning limit (α_{cr}) and remain there for some time before the ELM event occurs. In section 2.4.3, it was explained that the ballooning mode can be a soft limit to the edge pressure gradient and not necessarily lead immediately to a large instability event. This idea is supported by the shape of the marginal stability curve (figure 2.8), which shows that if the ballooning mode were to result in a small loss of edge pressure, the plasma would be stabilised.

COMPASS-D commonly displayed type III ELMs but possibly not type I ELMs, a slightly different interpretation of the model would apply to type III ELMs.

Two possible dynamics for type III ELMs on COMPASS-D present themselves. The first possibility is that, similarly to the type I model, temporary access to H-mode is granted due to suppression of the bootstrap current via high electron collisionality. If the electron collisionality then falls due to the rise in edge temperature, the edge current density can rise and an ELM would result.

The second possibility is that stability to the peeling mode is temporarily achieved due to the finite resistive diffusion time-scale, which limits the rate at which current can diffuse through the plasma. Any current rise in the edge region cannot happen faster than current can diffuse into the region. The resistive diffusion through a cylindrical shell is given by,

$$\tau_\eta \sim \frac{\mu_0 r l}{\eta}. \tag{2.27}$$

In the above, r is the radius of the cylinder or in this case, the minor radius ($0.17m$) and l is the characteristic scale-length, in this case, the pedestal width ($0.015m$). The resistivity η is given by Spitzer resistivity. For a typical COMPASS-D plasma, the value of T_e at $\psi_N = 0.95$, is $\approx 100eV$. The resistive diffusion time is $\tau_\eta = 4.5ms$.

There is also a neo-classical particle diffusion time, which limits the rate at which particles can diffuse though the plasma. In the absence of convective flows, the rate at which the edge pressure can change would be limited by neo-classical diffusion. For plasmas in the plateau regime ($1 < \nu^* > \epsilon^{-3/2}$), the neo-classical particle diffusion

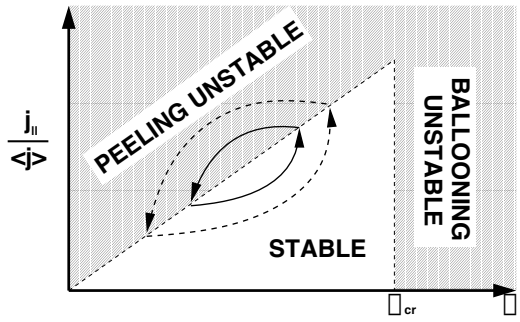

Figure 2.11: *A schematic of the stability boundaries showing the predicted locus of a small (solid line) and large (dashed line) type III ELM event.*

time is given by,

$$\tau_p \sim \frac{R}{v_{eT} q \rho_e^2}\, rl. \tag{2.28}$$

This time works out to be $\tau_p \approx 41ms$, which is an order of magnitude longer than the current diffusion time, equation 2.27. If it is assumed that all plasma parameters evolve towards a particular target, according to the nature of the equilibrium, then the discrepancy in the time-scales could be considered to be a problem. This model would require a significantly shorter particle diffusion time-scale than resistive diffusion time-scale. On the other hand, it is possible that the rate at which the edge pressure gradient changes is not limited by the neo-classical particle diffusion time. Indeed, data from COMPASS-D shows that the edge pressure gradient can change on time-scales much faster than $41ms$ (section 5.4.2). This result implies that neo-classical diffusion alone is not solely responsible for the changes in pressure at the edge. Convective plasma flow or turbulence must play an important role.

From Lenz' law, it is known that in any resistive media, a current cannot rise simultaneously with its source and therefore the edge current density must lag behind the pressure gradient, irrespective of the cause of the change in the edge pressure. If the de-stabilizing current is driven by the edge pressure, then the difference in rise times is prescribed by the resistive diffusion time. A mathematical discussion of Lenz' law and current penetration due to resistive diffusion is provided in section 6.3.4.

This model is appealing as it is clear that type III ELMs would be of smaller size, involving a smaller loss of energy than type I ELMs. Figure 2.11 shows the locus in parameter space for a type III ELMy discharge.

The model is in keeping with the observations by Kass et al. (1997), as mentioned

in section 2.2. In particular, radiative cooling of the edge has been shown to induce type III ELMs. This might be due to the decrease in the current diffusion time as resistivity increases or the increase in resistivity. Furthermore, as also reported by Kass et al. (1997), heating the core of the plasma may cause more current to flow in the core, thereby reducing the value of the normalised edge current.

Work by Osbourne et al. (1997) showed two sub-types of type III ELMs. Although there is nothing in the model to separate these two types of ELMs, the key observations regarding each type can be explained. The high density type disappear above a certain critical temperature. In this case, the ELMs might be stabilized due to an increase in core current. The low density type, disappear above a critical value of α, this may be due to the peeling mode being stabilised by the edge pressure gradient.

The model also includes a candidate explanation as to why type III ELM frequencies decrease with input power while the ELM size increases as mentioned in section 2.2. As the power into the plasma is increased, the temperature of the plasma increases and so does the resistive diffusion time. It might also be thought that the rate at which the edge pressure recovers might increase or at least, not decrease. This effect will allow the plasma to penetrate deeper into the stable region as the input power causes α to rise during each inter-ELM period. The increased depth into the stable region will mean a longer delay before the edge current density can trigger the peeling mode but also a larger ELM cycle in terms of edge pressure and current loss. Figure 2.11 shows the loci in parameter space for a type III ELMy discharge with large and small type III ELMs.

Chapter 3

Instrumentation

At the beginning of this project, the HELium Injection and Optical Spectroscopy (HELIOS) (Field et al., 1999a) and the Charge Exchange and Light Emission Spectroscopy (CELESTE) (Carolan et al., 1995) were already in regular use. Over the course of the project, several alterations and improvements were made to the HELIOS diagnostic and the two diagnostics were unified to create a single powerful diagnostic (Carolan et al., 2001). The result of this synergy was the HELIOS-CELESTE hybrid diagnostic, a schematic of which can be seen in figure 3.1.

3.1 Gas injection

The original HELIOS made use of a $4mm$ open pipe with a graphite end, through which helium was puffed into the COMPASS-D tokamak. The conductance of the pipe proved to be too high; the influx of gas, although constant enough to allow meaningful data to be taken, decayed too rapidly and so data could only be taken over a very short period of time. In addition, it proved difficult to control the amount of helium entering the vessel.

A nozzle manifold was designed to alleviate these problems. The manifold consisted of an oblong block with carbon shields attached to the sides, with counter-sunk hex-headed bolts. The purpose of the carbon shields was to protect the nozzle from the plasma, which would not only score the surface of the manifold but deposit material on the plasma facing sides and eventually block the nozzles. The shields had rounded edges and the bolts were counter-sunk to prevent localised heating.

The manifold was machined out of a single piece of stainless steel. The three nozzles were made out of $0.1mm$-thick discs of steel that were drilled with tapered holes to form tiny convergent nozzles. Several sets of nozzles were made, with exit

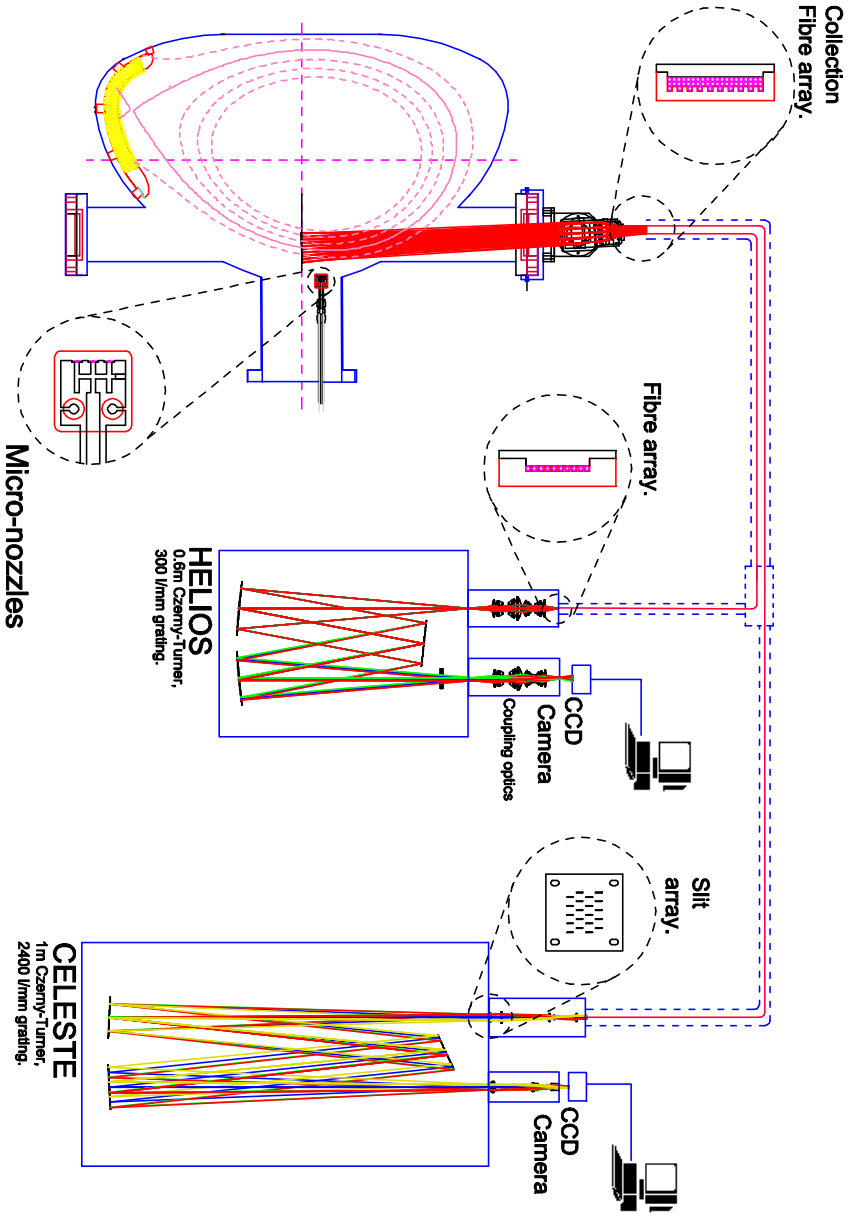

Figure 3.1: *A schematic drawing of the HELIOS-CELESTE hybrid diagnostic.*

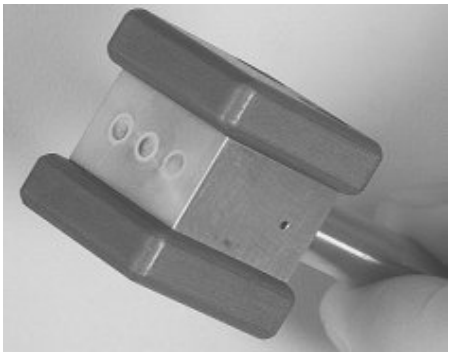

(a) *Photograph of the nozzle manifold. The dark grey blocks on the side of the manifold are graphite shields, which protect the manifold from the plasma.*

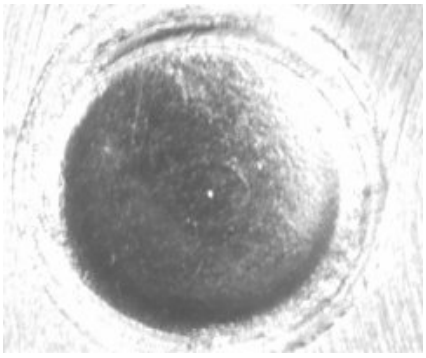

(b) *Closeup photograph of one of the micro-nozzles. The nozzle itself can be seen as a white dot in the centre of the disc.*

Figure 3.2: *The nozzle manifold used for helium gas puffing.*

hole sizes of $10\mu m$, $20\mu m$, $50\mu m$ and $100\mu m$, which gave the ability to vary the conductance of the manifold if it was found to be too high or low. In the final implementation, three $20\mu m$ nozzles were used. A photograph of the nozzle manifold and a close-up of one of the nozzles can be seen in figure 3.2. The nozzle itself can be seen as the white dot in the centre of figure 3.2b.

To prevent accidental re-pressurisation of the tokamak, a plenum was used which was manually valved-off from the helium gas bottle at all times except when filling the plenum to a pressure of between $1 - 1.4bar$. The flow of helium through the manifold was regulated by a piezo-electric valve which was in turn, controlled by a remote waveform generator. The low conductance of the micro-nozzles resulted in a steady influx of $\approx 10^{19}s^{-1}$. After each plasma discharge had finished, a pneumatic valve was opened to allow the volume behind the nozzles to be pumped out by a turbo molecular pump. This was done to prevent helium from leaking into the vessel between discharges and degrading the vacuum conditions.

3.2 Collection lens and optical fibres

Neutral helium was puffed into the tokamak where the gas became excited by collisions with background electrons and thus, emitted light. The physical processes behind this emission will be explained in chapter 4. The light from this emission

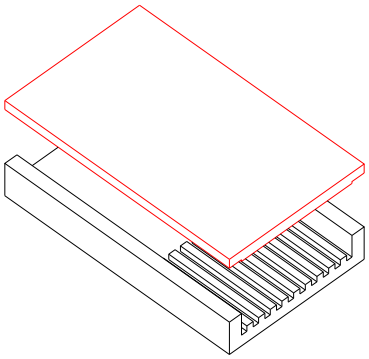

(a) *A design drawing of the brass fibre terminator. Both the base (black) and the lid (red) were made of naval brass.*

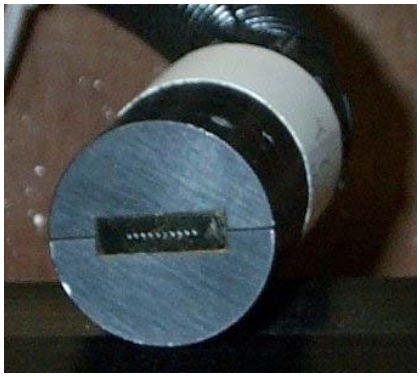

(b) *The completed fibre terminator in its housing.*

Figure 3.3: *The fibre terminator for the HELIOS spectrometer.*

was collected by a lens mounted on one of the top ports of the vessel, at the same toroidal position as the nozzle manifold. The radial position of the lens was such that it viewed, in a vertical direction, an area which included the point at which the central line of the injected helium flow intersected the separatrix. The radial position was $r = 0.693m$. The lens was a $100mm$, $f/2$ which focused the emitted light onto two adjacent arrays of $400\mu m$ diameter quartz optical fibres arranged as shown in the top left corner of figure 3.1.

The single array of ten fibres on the right side of the collection array gathered the light for the HELIOS spectrometer. The ten fibres were separated by oblong ridges of brass measuring $0.6mm \times 0.6mm$, at a pitch of $1.3mm$, standing proud of the inner surface of the fibre terminator. The ten resulting viewing chords had a spacing of $5.2mm$, covering a distance of $46.8mm$ at the mid-plane of the torus where the helium puff entered the plasma.

The adjacent array of 2×19 quartz fibres had the same extent as the single dimensional array of 10 chords. This meant that the two dimensional array covered the same $46.8mm$ radial distance but with twice the resolution, $(2.6mm)$. The three rows of fibres were separated by thin brass shims of $0.1mm$ thickness. The fibre terminator was made from two solid pieces machined out of naval brass. A drawing of one of the fibre terminator assemblies can be seen in figure 3.3a. The fibres were arranged inside the deep half of the block, resin was then poured into the block before the lid was put in place and clamped until the resin was completely set. To

finish the assembly, the fibres were ground down until they were flush with the brass housing and then polished. The assemblies were mounted in custom-made housings which protected the fibres and the assemblies from dust and mechanical damage. A photograph of the completed housing and assembly that connected to the HELIOS spectrometer can by seen in figure 3.3b.

Light was relayed by the bundle of 48 fibres to a junction box where the two sets of fibres were divided. The ten fibres from the single dimensional array were diverted to the HELIOS spectrometer. The fibres from the two dimensional array led to CELESTE.

3.3 The HELIOS Spectrometer

The HELIOS spectrometer was a low dispersion, low resolution instrument. It was a 0.6 meter Czerny-Turner device (Rank-Hilger M600) (Conway, 1998) (*cf.* figure 3.4) fitted with a $1200 lmm^{-1}$ grating. The fibre array can be seen in figure 3.3b. The manufacture method of the fibre terminator was similar to that of the light collection block.

The entrance slit of the spectrometer was of variable width but was normally set to $200\mu m$. A front-to-front conjugate pair of $35mm$ camera lenses were used to match the aperture of the fibres, 0.23 N.A (Numerical Aperture), to that of the spectrometer, $F/4.5$. The lenses were $50mm, F/1.2$ connected to the fibres, with a $100mm, F/2.5$ focusing onto the spectrometer slit. At the spectrometer exit, there was a similar pair of $35mm$ conjugate lenses; a $100mm, F/2.5$, which collimated the light, and a $35mm, F/2.5$ lens re-focused the spectrum onto the Charge Coupled Device (CCD) camera (Burke et al, 1997). The design of the Czerny-Turner spectrometer has an inherent astigmatism. All spectrometers of this type have a slightly shorter focal length in the optical plane, which is the plane corresponding to the direction of the spectral dispersion. This is the result of the spherical mirrors being used off-axis. The effect was corrected using an $f = 300mm$ cylindrical lens which was placed between the collimating mirror and the exit plane.

The CCD camera had a limited dynamic range. Consequently, the slit width was set wide enough to admit adequate light to give good photon statistics without admitting enough to cause saturation. One of the spectral lines observed by HELIOS was much stronger than others and so it was necessary to place a neutral density filter at the exit of the spectrometer to reduce the relative strength of the strongest line.

The CCD camera (Wright Instruments Ltd., No. P059, Enhanced II Electronics)

(a) *The black trunking on the right contains the optical fibres from the tokamak. At the spectrometer exit, the grey lead carries the control signal for the FLC shutter. Connected to the shutter mount are the exit lenses and then the CCD camera The two grey boxes in the foreground are the camera power supply (top) and the control system for the FLC shutter (bottom).*

(b) *Plan view with the lid removed showing the two spherical mirrors (left) and the grating (right).*

Figure 3.4: *The HELIOS Spectrometer - a* $0.6m$ *Czerny-Turner device (Rank-Hilger M600), fitted with a* $300lmm^{-1}$ *grating.*

utilises an EEV back-illuminated sensor (CCD02-06-2-232). The chip was Peltier cooled to $200K$ to reduce the current arising from thermal noise which is present even in the absence of light. The typical *dark current* for this chip was $0.6\ e\ s^{-1}\ pixel^{-1}$. The chip was divided into two sections; the image region and the storage region. When photons hit the pixels in the image region, they cause an increase in the charge of that pixel, dependent on the product of the number of photons and the quantum efficiency of the chip, which peaks at 60% for a wavelength of $650nm$. Accumulated charge could be shifted in the image and storage regions independently; the chip had a $1\mu s$ vertical transfer time. In order to capture multiple time frames, the charge from each viewing chord, which occupied about 30 rows in the image region, was concentrated or *binned* into a single row of the storage region. This enabled an entire time frame to be stored in as may rows as there were chords, usually 10. In total, 30 frames of 10 chords could be stored per discharge.

The camera had a 16-bit, dual speed analogue to digital converter (ADC) with either a $5.2\mu s$ or $34\mu s$ digitisation time. The camera was controlled by a PC running bespoke Windows© based software written by Conway (1998), through an interface card which allowed the operator to define arbitrary binning regions and timing sequences. The storage region was read out after each discharge, there was typically $5.6er.m.s.$ noise generated during readout. There was a pre-amplifier which matched the full-well capacity of the sensor, which was $3.7 \times 10^5 e$, to the range of the ADC. This resulted in 20 electrons per count for 15-bit data.

3.3.1 Time resolution issues with HELIOS

The time taken to bin the data from the image region into the storage region, τ_{bin} was the sum of the vertical transfer times of the two regions, τ_v $(1\mu s)$ and the time taken to switch between modes, τ_m $(2\mu s)$. Mathematically,

$$\tau_{bin} = \sum_{i=1}^{N} \left[(h_i + 1)\, \tau_v + 2\tau_m \right], \tag{3.1}$$

where h_i is the height in pixels of row i, and N represents the number of used rows in the image region. When the image occupied the entire region, the binning time was $322\mu s$.

In the initial incarnation of HELIOS and in the first implementation of the hybrid diagnostic, no shutter system was used. This meant that the image region of the chip continued to be illuminated whilst the charge was being clocked into the storage region. There was also a contribution from residual charge left from chords further

from the storage region during the previous binning period. This form of spatial *smearing* was found to be of the order of τ_{bin}/τ_{fr}, where τ_{fr} is the reciprocal of the frame rate. Although the smearing was removed numerically (Field et al., 1999a), it was found that changes in intensity of the lines between the measuring and binning period caused errors, with larger errors being associated with faster frame rates. A frame rate of $500s^{-1}$ was typically chosen, corresponding to a $\tau_{fr} = 2ms$.

A shutter system was designed and implemented to increase the time resolution to $1ms$ and faster. After careful consideration, a Ferroelectric Liquid Crystal (FLC) shutter was chosen and driven by a modified Displaytech DR-50 FLC driver (Displaytech Inc, 1991). The FLC driver was controlled by external timing pulses generated by the camera, to synchronise the shutter with the binning of the charge.

Several modifications had to be made to the driver before it could be used. The first issue was that of closing the shutter between discharges. According to the driver manual, the duty cycle should be kept as close to unity as possible. Keeping the shutter either open or closed for long periods would lead to *"the generation and migration of ions in the liquid crystal material and can lead to shortened life or degraded performance"* (Displaytech Inc, 1991). The problem was solved by using a protection circuit that would inhibit shutter activation if its state was not changed for a given amount of time. The second issue was that when the shutter was left in an indeterminate state for any length of time, the orientation of the liquid crystals would *wander* and regions of clear and dark would appear. These patches would disappear after the state of the shutter was changed three or four times. Two seconds before the plasma discharge began, a control signal was sent to allow diagnostics to be initialised. This pulse was used to initialise the protection circuit and a series of pulses were sent to the FLC shutter to align the crystals before data were taken.

3.3.2 Setup and Calibration

In the case of HELIOS, which was a low dispersion spectrometer, the calibration was less demanding than for high dispersion spectrometers, such as CELESTE.

An integrating sphere, which produces white light at a selected intensity was used for the intensity calibration. The collection lens at the tokamak was placed at the exit of the integrating sphere and the spectra were recorded using the CCD camera. The resulting image showed the variations in intensity across the fibres and the spectrum as a result of the entire optical system. The sensitivity of the entire system for each camera pixel, $(S(pi))$ could be ascertained from the intensity of the light from the integrating sphere, (I_s) and the number of photons counted, $(N(pi))$ after subtracting

the *dark current*,

$$S(pi) = \frac{I_s}{N(pi)}. \tag{3.2}$$

This information was used to correct for variations in the quality of transmission for each chord across the spectral band of interest.

For the wavelength calibration, a helium lamp was used, which generated several lines in the spectral region that HELIOS covered. The central wavelength of the spectrometer (λ_{pi0}) was set by rotating the grating until a suitable spectral line ($671.2nm$) was imaged at the centre of the CCD chip. The wavelength separation between the spectral lines was compared to the separation in pixels at the CCD camera to calculate a dispersion relation for the system,

$$D = \frac{\Delta\lambda}{\Delta pi}. \tag{3.3}$$

In the above, $\Delta\lambda$ is the wavelength separation of two given spectral lines and Δpi is the number of pixels between the same lines. The dispersion relation was used in conjunction with the central wavelength of the spectrometer to calculate the exact wavelength of each pixel so that the relevant spectral lines could be identified for analysis. The wavelength associated with a given pixel (λ_{pi}) is calculated using,

$$\lambda_{pi} = \lambda_{pi0} + (D \times pi), \tag{3.4}$$

where pi is the pixel number. A particular pixel was designated $pi = 0$, this was where the centre of the line used to define λ_{pi0} was observed.

3.4 The CELESTE Spectrometer

The CELESTE (*cf.* figure 3.5) was similar to the HELIOS spectrometer, but there were a few important differences. It was also a Czerny-Turner device (Hliger-analytical) but had a longer focal length at $1m$ and a higher f-number, $F/10$. It had a grating of $2400l/mm$. The spectral, spatial and temporal resolution are all higher for CELESTE than HELIOS.

CELESTE had a multiple entrance slit design, which catered for each of the 20 views of the plasma with a separate slit. The arrangement of the slits can be seen in figure 3.1. As can be seen, the slits were arranged in a 4×5 staggered grid. The slits were typically $400\mu m$ in width and made from laser cut metal foil. Nineteen of the slits were fed by sets of two fibres originating at the tokamak, with one slit being

Figure 3.5: *The CELESTE spectrometer - a* $1m$ *Czerny-Turner device fitted with a* $1200lmm^{-1}$ *grating.*

fed by a pair of fibres that originated at a helium spectral lamp which was used as an absolute wavelength reference.

At both the entrance and exit of the spectrometer, there were custom designed zoom optics (Carolan et al., 2001) that matched the light from the fibre bundles to the F-number of the spectrometer and focused the dispersed spectrum onto a CCD camera. An anamorphic lens system was used at the exit of the spectrometer which caused a demagnification of 3 in height and of 2 in width *i.e.* the spectral dispersion direction. The anamorphic quality increased the *etendue* of the system whilst maintaining the high spectral resolution. The image was also better fitted to the image region of the CCD. The lens system was astigmatic to correct for the astigmatism of the spectrometer.

At the spectrometer exit, CELESTE had an interference filter which only allowed the light from a narrow spectral band to pass; in this case the region around the HeII line $(468nm)$ was selected. Referring to figure 3.1, it can be seen that there were five slits per row in the slit array. By eliminating polychromatic light, the filter ensured that there was no interference between neighboring slits due to dispersion by the spectrometer.

The high temporal resolution was the result of two factors. The CCD camera used, although similar to the one used on HELIOS, had a faster row-shifting time, $0.3\mu s$. Combined with the staggered slit arrangement, which caused only two spectral lines to be imaged on any given column, the fast camera allowed CELESTE to run at frame rates as high as $4000s^{-1}$.

3.4.1 Setup and Calibration

For the CELESTE intensity calibration, the collection lens was again placed at the exit of the integrating sphere so that light of a known intensity entered the optical fibres. After the *dark current* was subtracted, the number of counts for each chord and each wavelength (horizontal pixel) could be used to calculate the total efficiency of the system from fibres to camera. The method was the same as that described in section 3.3.2.

For the wavelength calibration, a zinc lamp was used as the calibration source. The spectrometer grating was rotated so that a spectral line ($468.2nm$), close to the $HeII$ line of interest ($468.6nm$), was imaged onto the CCD. Two lines, including the line of interest were used to measure the dispersion of the spectrometer in terms of camera pixels. The method was similar to that described in section 3.3.2.

This technique was adequate for the wavelength calibration of HELIOS, which is a relatively low dispersion spectrometer. CELESTE was used to measure Doppler shifts (section 4.5) at high spectral resolution. Such measurements are problematic because high resolution spectrometers, such as CELESTE, are very sensitive to thermal drift and mechanical vibrations. The shift in the position of components caused by thermal expansion due to large temperature variations is sufficient to cause serious errors. A line of known wavelength ($468.2nm$) was observed simultaneously with the data to minimise this effect. This was the role of the zinc lamp discussed in section 3.4. The line from the spectral lamp that corresponded to the observed line in the plasma was used as an absolute wavelength reference,

$$\Delta\lambda_{\text{final}} = \Delta\lambda_{\text{obs}} - \Delta\lambda_{\text{ref}}, \tag{3.5}$$

In the above, $\Delta\lambda_{\text{ref}}$ is the shift in wavelength of the reference chord, and $\Delta\lambda_{\text{obs}}$ is the shift in the observed central wavelength of the measurement chords.

It will be explained in section 4.5 that the temperature of an ion can be calculated from the width of its spectral lines. A systematic error in the temperature measurements is introduced because any optical system will cause a spectral line to broaden (Hutchinson, 1987). This error can be corrected for by measuring the *instrument function*, which is the shape of the intensity function recorded when observing an infinitesimally-narrow spectral line. This function was obtained by illuminating the ends of the fibres at the tokamak using a zinc lamp, which emits lines of very narrow spectral width, with one at $468nm$, and recording the data using the CCD camera. An equivalent temperature due to the instrument function (T_{instr}) was calculated and

used to correct for the error using,

$$T_i = T_{\text{raw}} - T_{\text{instr}}, \tag{3.6}$$

where T_i is the final ion temperature and T_{raw} is the uncorrected value.

Chapter 4

Analysis

In section 1.6, mention was made that by observing the light emitted from an impurity ion in a plasma, it is possible to indirectly measure properties of the plasma. In this section, the physics principles that were used in the analysis of the data from both HELIOS and CELESTE is described. A description of the method of analysis for diagnostics is presented and a brief discussion of errors is given. Finally, there is a description of how the two diagnostics work together in synergy to measure the radial electric field.

4.1 Atomic data

As described in section 3.1, neutral helium is injected into the COMPASS-D plasma by means of custom-designed array of nozzles. The collisional excitation rate coefficient for collisions between helium atoms and background electrons from any given energy state state, j to any other given excited state, k, where $j \neq k$ is given by,

$$C_{jk} = \langle \sigma_{jk} \cdot v_e \rangle \, n_e. \tag{4.1}$$

In the above, σ_{jk} represents the collisional cross-section for an excitation from state j, to state k. The velocities of the electrons is given by v_e. Since the mass of the atom is much larger than that of the electron, the atoms can be considered to be stationary. The electrons represent a background field which, provided they are in thermal equilibrium, obey Boltzmann statistics. The angular brackets in the expression refer to the velocities being averaged over a Maxwell-Boltzmann distribution. The density of the electrons is given by n_e.

If the electron density is sufficiently low, the excitation rate, C_{jk} will be lower than the spontaneous relaxation rate, given by the Einstein coefficient, A_{kj} (Alonso

and Finn, 1968). For any two states,

$$\sum_{j \neq jk} \langle \sigma_{jk} \cdot v_e \rangle \, n_e \ll \sum_{j<k} A_k. \tag{4.2}$$

In this case, there will be a negligible number of atoms in excited states (Kornejew, 1996). By a simple re-arrangement, a critical electron density n_e^* can be found,

$$n_e^* = \frac{\sum\limits_{j<k} A_{kj}}{\sum\limits_{j \neq k} \langle \sigma_{jk} \cdot v_e \rangle}. \tag{4.3}$$

Below this critical density, the so-called coronal model can be applied whereby the intensity of the emission of a given line is considered to be dependent only on the excitation rate, given by equation 4.1.

Above this critical density, it can no longer be assumed that there are a negligible number of atoms in excited sates and other processes like collisional de-excitation must be taken into consideration. The more complete theory of atomic transitions is known as the Collisional Radiative model (Kornejew, 1996; Brix, 1998; Summers, 1994).

The COMPASS-D edge plasma has a temperature of $\approx 75eV$. At this temperature, the critical electron density n_e^*, is $\approx 10^{17} m^{-3}$, which is two orders of magnitude lower than the expected electron densities (Field et al., 1999a).

4.1.1 The coronal model

For the coronal model, it is assumed that the only source of population of any excited state is the result of excitation from the ground state, i. It is also assumed that the only source of de-population is spontaneous relaxation which is given by the product of the density of atoms in a particular energy state multiplied by the Einstein coefficient for all allowed transitions, (A_j). For equilibrium, the rate of excitation must balance the rate of relaxation,

$$\langle \sigma_{ij} \cdot v_e \rangle \, n_i n_e = A_j n_j. \tag{4.4}$$

The intensity of light emitted as a result of any particular transition can be calculated using the Branching ratio A_{jk}/A_j which is the ratio of probabilities of the transition in question to all allowed transitions,

$$I_{jk} = \langle \sigma_{ij} \cdot v_e \rangle \, n_i n_e \frac{A_{jk}}{A_j}. \tag{4.5}$$

It can be seen that the intensity of the light is dependent on the density of the background electrons, the density of the helium and the temperature of the electrons, which enters equation 4.5 as the Maxwellian averaged electron velocity.

4.1.2 The Collisional radiative model

As mentioned above, the edge conditions in COMPASS-D are such that the coronal model is inadequate to describe the line intensities for a neutral helium jet. A full collisional radiative model must be used which takes into account both electron collisional excitation and de-excitation, as well as electron collisional ionisation. Details of collisional radiative models for helium have been presented by several authors, (Cunningham, 1955; Fujimoto, 1979; Summers, 1994; Kornejew, 1996; Sasaki et al., 1996; Brix, 1998).

Electron collisional excitation and de-excitation

The generalised expression for collisional excitation and de-excitation for any given level j, is determined by the sum of all collisional excitations and de-excitations into that level, minus the sum of all collisional excitations and de-excitations out of the level;

$$\left(\frac{\partial}{\partial t}n_j\right)_{\text{collisional}} = \sum_{k\neq j}\langle\sigma_{kj}\cdot v_e\rangle\, n_e n_k - \sum_{k\neq j}\langle\sigma_{jk}\cdot v_e\rangle\, n_e n_j. \tag{4.6}$$

Spontaneous transitions

The generalised expression for spontaneous transitions is similarly found to be the sum of all spontaneous decay into level j, minus the sum of all spontaneous decay out of the level,

$$\left(\frac{\partial}{\partial t}n_j\right)_{\text{spontaneous}} = \sum_{k>j}A_{kj}n_k - \sum_{k<j}A_{jk}n_j. \tag{4.7}$$

Electron collisional ionisation and re-combination

Finally, the rate of change of population for level j due to ionisation and recombination caused by electron collisions is;

$$\left(\frac{\partial}{\partial t}n_j\right)_{\text{ionisation}} = \langle\sigma_{j.rec}\cdot v_e\rangle\, n_e n_{ion} - \langle\sigma_{j.ion}\cdot v\rangle\, n_e n_j. \tag{4.8}$$

The rate equation

The sum of all these effects gives the collisional radiative description of the given state, j,

$$\begin{aligned}\left(\frac{\mathrm{d}}{\mathrm{d}t}n_j\right) &= \sum_{k\neq j}\langle\sigma_{kj}\cdot v_e\rangle\, n_e n_k - \sum_{k\neq j}\langle\sigma_{jk}\cdot v_e\rangle\, n_e n_j \\ &\quad + \sum_{k>j} A_{kj} n_k - \sum_{k<j} A_{jk} n_j \\ &\quad + \langle\sigma_{j.rec}\cdot v_e\rangle\, n_e n_{ion} - \langle\sigma_{j.ion}\cdot v\rangle\, n_e n_j. \end{aligned} \tag{4.9}$$

Equation 4.9 can be expressed for any energy state and is therefore representative of a system of rate equations. To solve the system, a matrix of the rate coefficients for each process and each level, $\underline{\boldsymbol{C}}$ must be assembled,

$$\frac{\mathrm{d}}{\mathrm{d}t}\boldsymbol{n_j} = \underline{\boldsymbol{C}}\cdot\boldsymbol{n_j}. \tag{4.10}$$

Each row of the vector product of $\underline{\boldsymbol{C}}$ and the population density vector, $\boldsymbol{n_j}$, corresponds to a balance equation of the form of equation 4.9. Equation 4.10 can be solved numerically and an *effective emission rate coefficient* $C^{eff}(\lambda)$ may be defined for each emission line, as a function of n_e and T_e (Sasaki et al., 1997). The emission rate coefficients for this work were produced by Summers (1994).

4.1.3 Atomic Data Analysis Structure (ADAS)

The atomic data analysis structure (ADAS) (Summers, 1994) is a suite of numerical codes and databases which produce atomic data for a variety of applications. ADAS includes a collisional-radiative model of helium accounting for 19 atomic states of neutral helium with one electron in ground state and the other in every level up to and including $n = 4$, where n is the principal quantum number.

4.2 The principle of electron temperature and density measurement from helium line ratios

The density and temperature of the background electrons affect the intensity of each emission line. The intensity is also proportional to the density of neutral helium. It is clear that the absolute intensity measurements of any given single line do not yield sufficient information to deduce the value of any of the electron parameters. In order to make a measurement that was invariant of the density of the test gas, it was necessary to use line intensity ratios.

To separate the density dependence from the temperature dependence, two ratios were chosen and a consistent solution for both ratios was found. In order to make clear and unambiguous measurements, one ratio that has a strong temperature dependence and one that has a strong density dependence were chosen.

Figure 4.1 shows the energy levels for helium with one electron in the ground state. Some of the allowed quantum transitions are shown. Line pairs commonly used for this type of measurement are from the $n = 3$ to $n = 2$ levels, they are $667.8nm/728.1nm$ or λ_2/λ_1, corresponding to $3d^1D - 2p^1P$ / $3s^1S - 2p^1P$ which has a strong n_e dependence and $728.1nm/706.5nm$ or λ_1/λ_3, corresponding to $3s^1S - 2p^1P$ / $3s^3S - 2p^3P$ which has a strong T_e dependence. These ratios have been used successfully elsewhere by Schweer et al. (1992); Davies et al. (1997); and Behrendt et al. (1997). The equivalent transitions from the $n = 4$ level are discussed in the literature (Sasaki et al., 1997) but are generally found to be too weak to be of practical use.

4.2.1 Determining temperature

The Measurement of electron temperature from helium line ratios was first proposed by Cunningham (1955). As an aid to understanding the temperature dependence of λ_1/λ_3, a simple model is presented here, although this methodology was not used for this investigation. The key to the strong temperature dependence of λ_1/λ_3 lies in the collisional excitation rate from singlet to triplet state *cf.* figure 4.2. The transition $1s^1S - 2s^3S$ requires a spin exchange with a free electron due to conservation of parity. The singlet to triplet excitation rate varies with T_e and develops a negative dependence above $\approx 10eV$ (Kornejew, 1996).

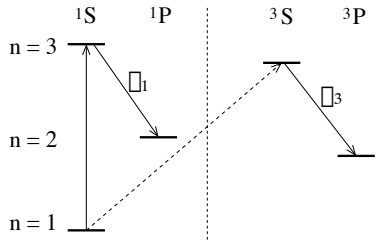

Figure 4.2: *Spin exchange leads to T_e dependence of R_1.*

The different energies of the equivalent singlet and triplet transitions must also be considered. According to Boltzmann statistics, the collisional transition rate from state j to state k is described by (Kornejew, 1996),

$$C_{jk} = \frac{8.01 \times 10^{-8}}{\omega_i \sqrt{T_e}} \, \gamma_{jk} \, \exp\left\{-\frac{\Delta E}{kT_e}\right\}. \tag{4.11}$$

where γ_{jk} is the collision strength. The ratio of the two intensities is proportional to

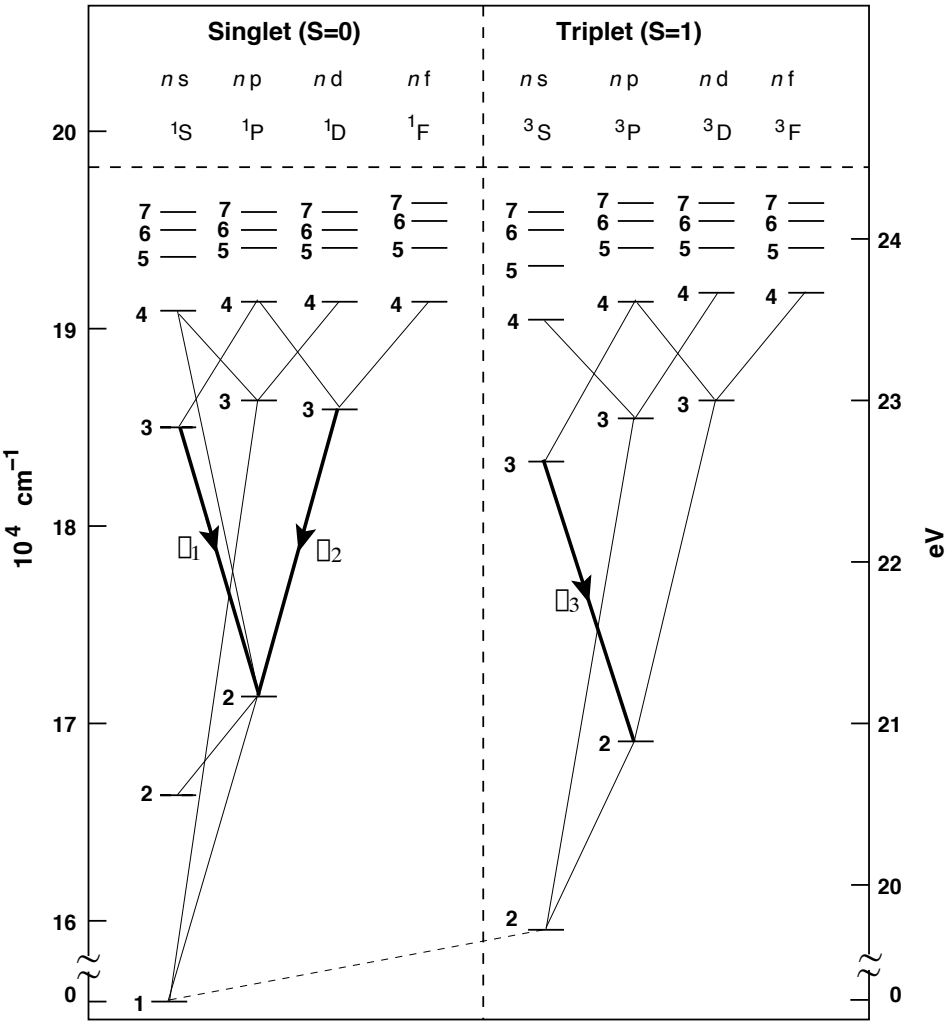

Figure 4.1: *Energy levels of helium with one electron in the ground state, showing some of the allowed transitions. The transitions in bold are recorded by HELIOS for extracting T_e and n_e. $\lambda_1 = 728.1nm$, $\lambda_2 = 667.8nm$, and $\lambda_3 = 706.5nm$. The dotted line shows the singlet-to-triplet transition that requires a spin-exchange excitation.*

the ratio of the transition rate,

$$R_1 = \frac{I_3}{I_1} \propto \frac{\gamma_3}{\gamma_1} \exp\left\{-\frac{(\Delta E_3 - \Delta E_1)}{kT_e}\right\}, \tag{4.12}$$

which contains an explicit temperature dependence.

As explained above, the simplified model shown here was not used to determine the T_e dependence of the three spectral lines. Instead, effective rate coefficients were taken from ADAS (section 4.1.3). Figure 4.3a shows the T_e dependence of the three emission rate coefficients for the range of temperatures of interest. The *humped* characteristic of the $706.8nm$ line can clearly be seen. Figure 4.3b shows the dependence of the two ratios on T_e. The fall-off in C_{eff}, the effective emission rate of the $706.8nm$ line results in the strong T_e dependence of R_1, the emission rate ratio of the $728.3nm/706.8nm$ lines. It is also worth noting that the $728.1nm/706.5nm$ ratio (R_2), is not independent of T_e. This is the result of the difference in energies of the relevant levels and the weak negative dependence on temperature of the $667.8nm$ line above $\approx 50eV$, which can be seen in figure 4.3a. The cause of this negative dependence is the excitation into and then out of the triplet state, via the $2s^3S$ and onto the $2p^1P$ levels.

4.2.2 Determining density

A simplified atomic physics model is used to illustrate the density dependence of λ_1/λ_2. As above, this model is shown as an aid to understanding and was not used as the methodology for the the analysis. The principle of density measurement using the line ratio of λ_1/λ_2 relies on collisional redistribution of the electron population among levels with the same principle quantum number n, in this case 3, but in different orbital shells, in this case, S and D, see figure 4.4.

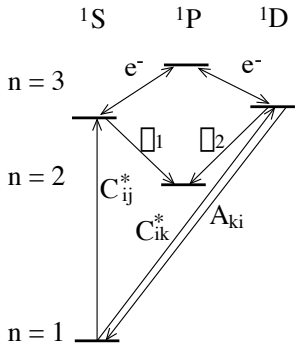

Figure 4.4: *Population redistribution leads to n_e dependence of R_2.*

The process is simplified so that only the collisional de-population coefficient from one of the levels to all other levels C^*_{km} is considered. Collisional excitation coefficients from the ground state to two levels may be represented by, C^*_{ij} and C^*_{ik}. The significance of the collisional depopulation of level $3d^1D$ will be dependant on the ratio of the collisional depopulation rate to the spontaneous relaxation rate to ground n_eC_{km}/Aki (Summers, 1994). The ratio, R_2 of the

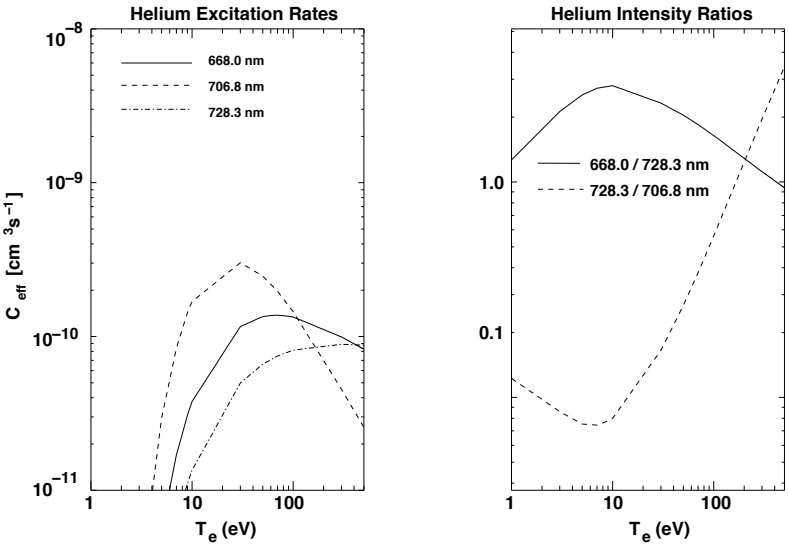

(a) *The temperature dependence of the three emission lines. The effective emission rate of λ_3 is shown by the dashed line, which has a peaked characteristic.*

(b) *The T_e dependence of the two ratios. The fall-off of C_{eff}, the emission rate of λ_3 results in a strong T_e dependence for R_1.*

Figure 4.3: *The T_e dependencies of the three effective emission rates and of the two ratios.*

two line intensities is given by,

$$R_2 = \frac{I_1}{I_2} \propto \frac{C^*_{ik}}{C^*_{ij}} \left(1 + n_e \frac{C^*_{km}}{A_{ki}}\right). \tag{4.13}$$

The effect becomes stronger as n_e increases, leading to an n_e dependence for ratio R_2.

Figure 4.5a shows the n_e dependence of the three emission coefficients which were taken from ADAS and not calculated using the above method. The effect of the collisional re-distribution of electrons can be seen. C_{eff} for λ_2 decreases only very slowly, until it begins to fall off at $n_e > 10^{14} cm^{-3}$ but for $\lambda_1, 667.8nm, C_{eff}$ falls off very quickly as the population of the $3d^1D$ level is collisionally re-populated at the expense of the $3s^1S$ level. The strong n_e dependence of R_2 can be seen in figure 4.5b

The dipped n_e dependence of R_1, is the result of a similar collisional redistribution affect among the triplet states that effects the electron populations at higher n_e.

4.2.3 Ratio inversion

From Figures, 4.3 and 4.5, it can be seen that the ratios R_1 and R_2 show strong dependence on T_e and n_e respectively but each ratio also has a weak, non-monotonic dependence on the alternate parameter.

Figure 4.6a shows a series of solutions for C_{eff} generated by ADAS. Each curve on the graph shows the predicted ratio of R_1 with respect to T_e at a range of fixed n_e. It can be seen that to make an exact measurement or T_e it is necessary to know the value of n_e.

The equivalent plot for the n_e dependence of R_2 for a range of T_e is shown in figure 4.6b. In symmetry with the above argument, a given ratio R_2 can only give an approximate result for n_e unless the value of T_e is known.

To return exact values of T_e and n_e, a self-consistent, simultaneous solution must be obtained. The HELIOS analysis programme works by obtaining a set of values for T_e and n_e for both R_1 and R_2 and spline fitting the two data-sets to give two loci in parameter space. Figure 4.7a shows two such data-sets and their spline fits. The near vertical curve, which gives an approximate result for T_e ,is generated by ADAS from R_1, the near horizontal curve, being the result for R_2.

The point where the two loci cross is the only consistent solution. Figure 4.7b is an output from the programme that was used to calculate the exact point of crossing

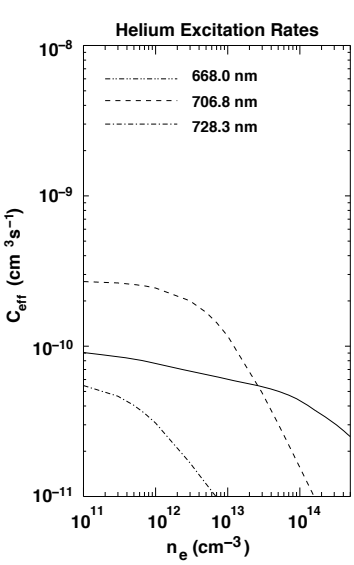

(a) *The effective excitation rates of the three emission lines with respect to n_e. The excitation rate of λ_2, (solid line) does not fall-off as quickly as the others, as a result of collisional redistribution of electron populations.*

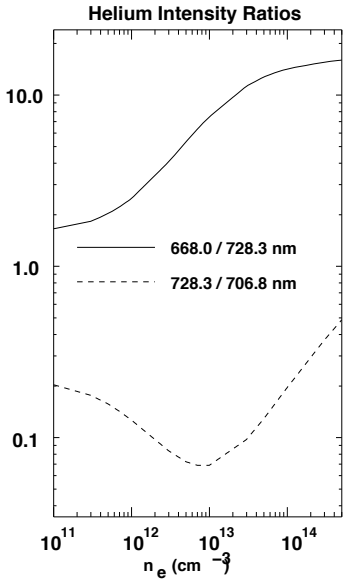

(b) *The n_e dependence of the two ratios. R_2 shows good n_e dependence over the range of interest.*

Figure 4.5: *The n_e dependencies of the three emission lines and the two ratios.*

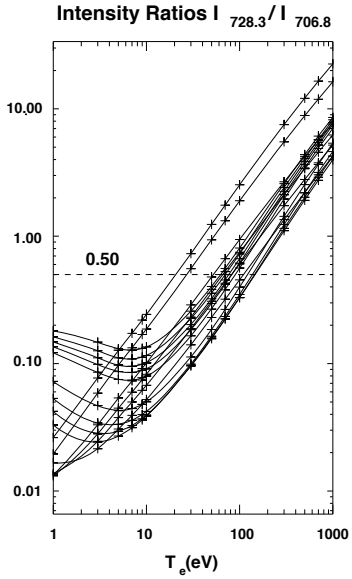

(a) *Solutions from ADAS for the T_e dependence of R_1 over a range of n_e, represented by each curve.*

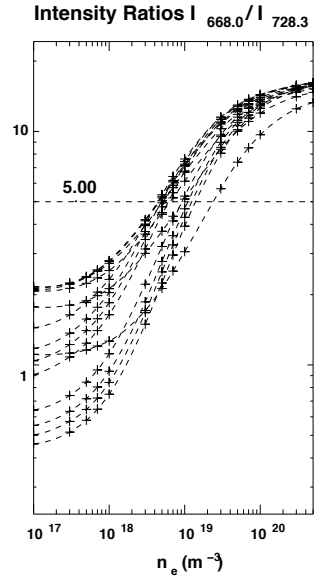

(b) *Solutions from ADAS for the n_e dependence of R_2 over a range of T_e, represented by each curve.*

Figure 4.6: *The T_e and n_e dependence of the two line ratios according to ADAS. It can be seen from figure (a), that a given ratio of $728.3/706.8nm$ will give an approximate value for electron temperature. Likewise, a particular value of $668.0/728.3nm$ will give an approximate value for electron density.*

for the two loci. For each point in parameter space, the horizontal distance to the near vertical line was calculated and added to the vertical distance from the near horizontal line. The result was a two dimensional matrix of values with a minimum at the point of crossing.

4.3 Calculating neutral density and electron density gradient from D_α Emission

As mentioned in section 1.6.1, D_α light is emitted from a shell at or around the separatrix. As well as being a good measure of re-cycling and an important diagnostic for mode transitions and ELMs, it can also be used to extract both the neutral density (n_D) and the electron density gradient with respect to ψ (n_e') at the edge (Tournianski et al., 2001).

Unlike the Helium emission data, which originates from a plume of gas, D_α emission is not localised. Any measurement of the emission is, therefore, a line integrated parameter which needs to be inverted to obtain a radial emission profile, $\epsilon(\psi)$. The 10 chords of HELIOS are insufficient to perform a full tomographic inversion but by considering the D_α emission to be a flux function, *i.e.* constant on surfaces of constant poloidal flux, inversion is possible. This assumption, although not strictly correct, is valid over the limited observation region (Meyer et al., 2000).

The inversion can be formulated as a matrix equation,

$$\boldsymbol{I} = \boldsymbol{L} \cdot \boldsymbol{\epsilon}, \tag{4.14}$$

where $\boldsymbol{I}$ is the intensity vector, $\boldsymbol{\epsilon}$ is the emissivity vector and $\boldsymbol{L}$ is the length matrix. The flux function is divided into j shells, determined by the radial positions for which the emissivity ϵ_j is required. The matrix element L_{ij} is given by the length of the i-th line of sight in the j-th flux shell, the shape of the flux shells being calculated using an EFIT reconstruction.

Emissivity was calculated as a function of flux and the neutral density calculated using a collisional radiative model formulated by Sawada et al. (1993). A full description of the method used for extracting n_e' and n_D from the D_α emission was presented by Tournianski et al. (2001). The method involves formulating a simple $1-D$ analytical model of the behaviour of the Full Width Half Maximum (FWHM) of the D_α emission profile,

$$\frac{\mathrm{d}n_e}{\mathrm{d}r} \approx \frac{v_0}{\langle \sigma v \rangle_{\mathrm{ion}}} \left(\frac{1.6}{\Delta_\alpha}^2 \right), \tag{4.15}$$

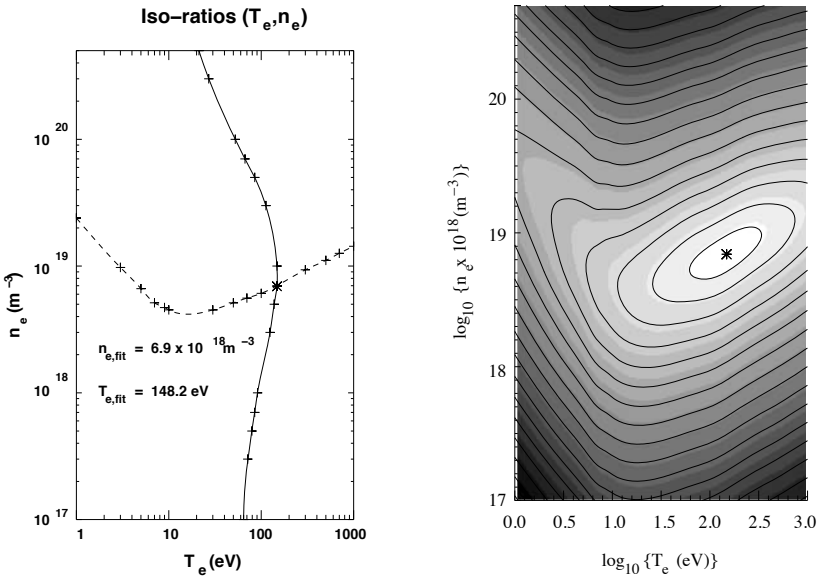

(a) *Loci in $n_e - T_e$ space generated by ADAS from R_1 (solid) and R_2 (dashed). The point of intersection is the consistent solution.*

(b) *Output from the analysis programme that identifies the point of intersection.*

Figure 4.7: *The values for the intensity ratios as loci in $T_e - n_e$ parameter space. The point at which the two loci cross is the self consistent solution for both parameters.*

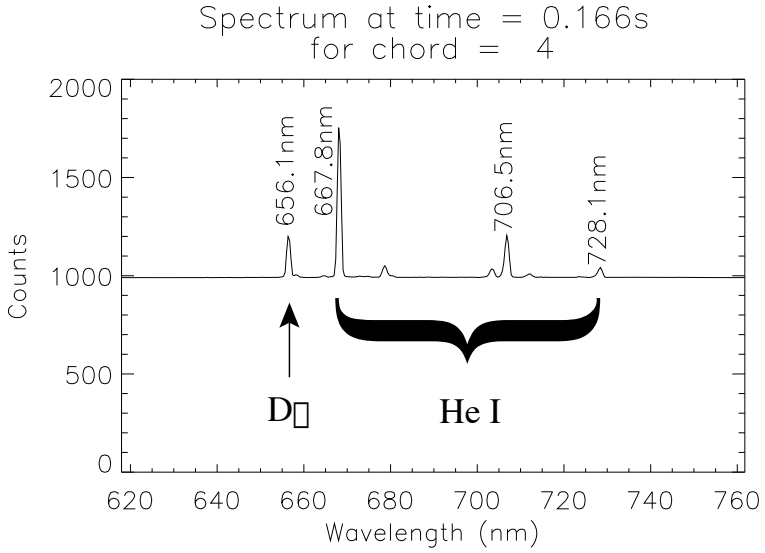

Figure 4.8: *A spectrum measured by the HELIOS spectrometer from discharge number 29759. For a description of the instrument, see chapter 3.*

where Δ_α is the FWHM of the emission profile. By neglecting charge-exchange recombination, and assuming that neutrals at the plasma edge can only be lost to ionisation, the D_α emission profile can be approximated,

$$D_\alpha = \frac{\mathrm{d}n_e}{\mathrm{d}r} \cdot r \cdot n_D(0) \exp\left\{ -\frac{\langle \sigma v \rangle_{\text{ion}}}{2v_0} \frac{\mathrm{d}n_e}{\mathrm{d}r} r^2 \right\} \langle \sigma v \rangle_{\text{ex}} . \tag{4.16}$$

In the above, $n_D(0)$ is the neutral density at the edge, and $\langle \sigma v \rangle_{\text{ion}}$ and $\langle \sigma v \rangle_{\text{ex}}$, which are the ionisation and excitation impact parameters respectively are assumed constant over the D_α emission range, *i.e.* a weak temperature dependence was ignored.

4.4 HELIOS analysis

An example of a spectrum for a single time point and single chord is shown in figure 4.8. The spectral lines for D_α and the three helium lines are marked. The initial analysis was done automatically using a bespoke analysis programme written by Anthony Field. The general method was to first remove the *dark current* (section 3.3) background signal pedestal. Next, the centre and edges of the spectral lines were identified and the regions identified as the lines were integrated across to give the line intensities and ratios. T_e and n_e were extracted either by using atomic emission tables from ADAS or, more usually, fast look-up tables generated beforehand. Since the spectral light was emitted from a localised plume of gas, it was considered that

an inversion to account for the curvature of the flux surfaces would be both overly complicated and unnecessary.

4.5 Doppler Spectroscopy

In addition to becoming excited, some helium atoms become ionised. The ions emit light at different characteristic wavelengths to neutral atoms. The CELESTE spectrometer was used to measure the poloidal velocity of these ions which were used as an indication of the poloidal velocity of the plasma and to calculate the radial electric field (Meyer et al., 2000).

The velocity of a particular ion can be measured in the laboratory frame of reference by comparing the observed wavelength of a spectral line with its known stationary wavelength (λ_0). Using the equation $v = c\Delta\lambda/\lambda$, which can be extended to a population by considering the effect on the centroid of the observed spectral line (Carolan et al., 1998),

$$v_i = c\frac{\Delta\lambda_0}{\lambda_0}. \tag{4.17}$$

In the above, v_i is the velocity of the species and c is the speed of light.

It is possible to use the width of the spectral line to calculate the temperature (T_i) of a light emitting species. The temperature is obtained by assuming that the ions have a Maxwellian velocity distribution, which is given by,

$$f(v) = \left(\frac{m_i}{2\pi k_b T_i}\right)^{3/2} \exp\left\{-\frac{v_i}{v_{th}}\right\}^2. \tag{4.18}$$

In the above, k_b is Boltzmann's constant, m_i is the mass of the ions and the thermal velocity (v_{th}) is defined by,

$$\frac{1}{2}m_i v_{th}^2 = k_b T_i. \tag{4.19}$$

Considering equations 4.18 and 4.17, the Gaussian line-shape is,

$$I(\lambda) = I_0 \ \exp\left\{-\left(\frac{c(\lambda-\lambda_0)}{v_{th}\lambda_0}\right)^2\right\}. \tag{4.20}$$

The corollary being that (Carolan et al., 1998),

$$T_i = \frac{m_i}{2k}\left(\frac{c\Delta\lambda}{\lambda_0}\right)^2, \tag{4.21}$$

where $\Delta\lambda$ is the full width, half maximum of the spectral line.

4.6 CELESTE analysis

The CELESTE analysis programme was written by Hendrik Meyer. In the same way as for the HELIOS diagnostic, the first step was to remove the *dark current* pedestal and perform the intensity calibration, mentioned in section 3.4.1.

Before analysing the raw data further, a simple geometrical inversion was necessary to account for the shape of the helium plume which was assumed to be conical, causing the path length to be longer, further into the plasma (Meyer et al., 2000). The inversion was simply,

$$\epsilon = \frac{I}{l \cos \vartheta}, \tag{4.22}$$

where I was the measured intensity, l was the distance from the nozzle, and ϑ was the divergence angle (30°). The result, ϵ, was the emissivity.

The initial analysis involves applying a Gaussian curve fit to the observed spectral lines. The full width, half maximum (FWHM) and the central value can be extracted from the final fit parameters. The shift of the central value from its known position was substituted into equation 4.17 as $\Delta\lambda_0$ to calculate the poloidal velocity of the impurity helium ions (v_z, $z = HeII$). The FWHM was substituted into 4.21 which was used to extract ion temperature (T_z).

The observed temperature must be corrected for the instrument function. The rigorous method would be to de-convolve the instrument function from the observed spectral line (Hutchinson, 1987). In this case, the rigorous method was deemed unnecessary as the instrument function was narrow and a good approximation to Gaussian. The convolution of two Gaussian is another Gaussian of width equal to the sum of the two previous widths (Press et al., 1992). An equivalent temperature was calculated for the instrument function using a negligibly narrow spectral line from a zinc lamp and equation 4.21, which was subtracted from the observed temperature of the $HeII$ in the plasma.

The absolute intensity of the line was used to calculate the $HeII$ density scale length, $L_n = (\nabla \ln n)^{-1}$, the method will be explained in section 4.7.

4.7 Diagnostic synergy

CELESTE was capable of directly measuring both V_θ and T_z in the region around the separatrix and HELIOS can measure n_e and T_e.

As mentioned in section 4.6, CELESTE records the absolute emissivity of the $468.6nm$ $HeII$ line which can be used to calculate the $HeII$ impurity density. The

line intensity is given by,

$$I_z = n_e n_z \chi, \tag{4.23}$$

where χ is the excitation rate. HELIOS supplied the value for n_e and was also used, in conjunction with ADAS to calculate χ.

The impurity ion velocity is not necessarily related to the bulk ion velocity. A more fundamental quantity that can be calculated is the electric field. Using radial force balance for z=$HeII$ from (Meyer et al., 2000),

$$\boldsymbol{E} = \underbrace{-\boldsymbol{v}_z \times \boldsymbol{B}}_{\text{Lorentz}} + \underbrace{\frac{\nabla p_z}{Z_z e n_z}}_{\substack{\text{diamag-}\\\text{netism}}} + \underbrace{\frac{m_z n_z (\boldsymbol{v}_z \cdot \nabla)\boldsymbol{v}_z}{Z_z e n_z}}_{\text{inertia}} + \underbrace{\frac{\nabla \cdot \bar{\boldsymbol{\pi}}}{Z_z e n_z}}_{\substack{\text{perpen-}\\\text{dicular}\\\text{viscosity}}} + \underbrace{\frac{\boldsymbol{R}_{z0}}{Z_z e n_z}}_{\substack{\text{neutral}\\\text{friction}}} + \underbrace{\frac{\sum_\beta \boldsymbol{R}_{z\beta}}{Z_z e n_z}}_{\substack{\text{coulomb}\\\text{friction}}}. \tag{4.24}$$

Only the contribution from the Lorentz force and pressure gradient need to be considered. The other terms can be neglected as they scale, normalised to the pressure gradient, as follows;

$$\begin{aligned}
\text{inertia} &\propto M_z^2 \approx 0.04, \\
\text{perpendicular viscosity} &\propto \frac{M_z \rho_z}{L_\perp} \approx 0.07, \\
\text{neutral friction} &\propto \frac{M_z L_\perp}{\lambda_{zn}} \approx 3 \times 10^{-6}, \\
\text{Coulomb friction} &\propto \frac{M_z L_\perp}{\lambda_{zi}} \approx 5 \times 10^{-5}.
\end{aligned}$$

In the above, $M_z = v_{z\theta}/v_{zth}$, ρ_z is the Larmor radius for the impurity species, $L_\perp$ is the typical pressure gradient scale length, and $\lambda_{\alpha\beta}$ is the mean free path for collisions between particles of species α and β. The contribution from the toroidal velocity can also be neglected since, on COMPASS-D, $v_\phi \ll v_\theta$ (Carolan et al., 1995) and owing to the cross-product with $\boldsymbol{B}$, the toroidal velocity was weighted by $B_\theta/B_\phi \approx 0.1$, making the contribution negligible. The resulting approximation was given by,

$$E_\psi = \frac{\nabla p_z \cdot \boldsymbol{e}^{\boldsymbol{\psi}}}{Z_z e n_z} - v_{z\theta} B_\theta, \tag{4.25}$$

where e^ψ is the unit vector (Hazeltine and Meiss, 1992),

$$e^\psi = \frac{\nabla \psi}{|\nabla \psi|}. \tag{4.26}$$

The final outstanding issue was the diamagnetic velocity contribution, $v_{z,dia}$, to the observed poloidal velocity, $v_{z\theta}$, which arises from the helium ion pressure gradient,

∇p_z. This can be obtained from the $HeII$ temperature, toroidal magnetic field and scale lengths of the $HeII$ density and temperature,

$$v_{z,dia} = -\frac{T_z}{Z_z eB}\left(\frac{1}{L_{n_z}} + \frac{1}{L_{T_z}}\right). \tag{4.27}$$

The $HeII$ ion density scale length can be taken from equation 4.23, rearranging gives,

$$v_{z,dia} = -\frac{T_z}{Z_z eB}\left(\frac{1}{L_{I_z}} + \frac{1}{L_{T_z}} - \frac{1}{L_{n_e}} - \frac{1}{L_\chi}\right). \tag{4.28}$$

The two diagnostics, when intimately coupled in this way, are greater than the sum of their parts. They represent a powerful tool for diagnosing plasma parameters and have proven particularly useful in L-/H- mode transition studies (Carolan et al., 2001).

4.8 Errors

4.8.1 Statistical errors

HELIOS

Photon statistics obey the Poisson distribution since they are events occurring at a constant rate but independent of one another (Bevington, 1969). The standard error in any such measurement is given by,

$$\sigma = \sqrt{\mu}, \tag{4.29}$$

where σ is the standard deviation and μ is the mean number of counts. These statistics are applicable to the actual number of counts registered at the CCD camera and so should not include the *dark current* in the calculation of μ. Once the background had been subtracted, the square root of the number of counts was taken and designated σ. Now at every step of the analysis, the error must be taken into account. Through most steps, standard error propagation equations can be used.

The ratio inversion stage of the analysis was numeric rather than analytic, and so error propagation equations cannot be applied. For each of the two ratios, the inversion routine was run three times. The first run used the unadulterated data and supplied the results for n_e and T_e. For the second run, the numerator for each ratio used was the sum of the signal and the error for the line in question, $\mu_{l1} + \sigma_{l1}$, and the denominator used was the difference between the signal and the error for the appropriate line $\mu_{l2} - \sigma_{l2}$. The result was the upper limit for n_e and T_e. The lower

limit was obtained by a similar method and the difference used to ascertain the new errors, σ_{T_e} and σ_{n_e}.

CELESTE

CELESTE, was subject to the same statistical errors in line intensity as HELIOS. The error in intensity of the spectral line is given by equation 4.29. The intensity error was propagated through the analysis programme, the error for the $HeII$ density scale length, $L_{n_z} = (\nabla \ln n_z)^{-1}$, was calculated using a similar technique to that employed for the the line ratio errors from HELIOS. For this case there were no ratios, just a simple upper and lower limit calculation.

The statistical error in the velocity measurement was calculated using the error in the line shift measurement. The position error is not proportional to the wavelength shift or absolute wavelength but to the width of the spectral line as its the random nature of the Maxwellian distribution that causes the error. Once the width of the instrument function was subtracted, the error was given by,

$$\sigma_{position} = \frac{W_{\text{FWHM}}}{\sqrt{8N \ln 2}}, \tag{4.30}$$

(Conway, 1998).
In the above, W_{FWHM} is the width of the spectral line at half the maximum value. The error in the width, which was related to the temperature by equation 4.21, was given by the same author to scale as,

$$\sigma_W = \frac{W}{\sqrt{2N}}, \tag{4.31}$$

where W is the width of the spectral line.

4.8.2 HELIOS Systematic Errors and difficulties

Two systematic errors were identified and addressed on HELIOS.

The spatial *smearing* that was discussed in section 3.3.1 caused the charge on the CCD camera from the outer chords to be clocked through the area illuminated by the inner chords. Since the signal strength for the outer-most chords was weaker than that of the chords near to the separatrix, the line ratios for the outermost chords were distorted in such a way as to overestimate both T_e and n_e. The effect of the error became more severe as the temporal resolution was increased. The installation of the FLC shutter not only allowed access to higher time resolution, as stated in section 3.3.1, but also alleviated this source of error.

Data on the inner side of the separatrix was found to have unphysically low n_e and T_e. In many cases, the signal was strong enough to give low statistical errors, nevertheless a *roll-over* in n_e and T_e was measured. The data used by ADAS to identify line ratios for a thermal helium jet partially relies on semi-empirical data like that published by Fujimoto (1978). Cross-sections relevant to the injection of neutral helium were obtained by injecting the gas into a plasma with known parameters. Although the line ratios were assumed to be time-independent, it might be the case that large amounts of recycled background helium could cause distortion of the results. Recycled helium would have a different time history to the injected helium, in particular a larger number of atoms would be in the triplet state. this would lower the temperature dependant ratio R_1. There would also be more atoms in higher excitation states than $n = 3$, thereby affecting the density dependant ratios through collisional or spontaneous de-excitation. A full collisional-radiative review of the atomic physics of helium would be needed to verify this source of error and quantify the effects, but was beyond the scope of this investigation. This *swamping* of the signal by background helium radiation was addressed by reducing the back pressure in the plenum (section 3.1), to reduce the total influx of helium. Generally, it was found that reducing the influx resulted in weaker signals and larger statistical errors.

The CELESTE systematic errors are discussed in section 4.6.

Chapter 5

Diagnostic Validation and Results

5.1 Validating the HELIOS results

To validate the data from HELIOS, a self-consistency check was performed; the profile of the measured light from the $667\ nm$ helium line, which is shown as λ_3 in figure 4.1, was compared with a prediction of the profile using the analysed data from HELIOS itself.

A discharge with HELIOS data over L-mode, ELMy H-mode and ELM-free H-mode was selected, and n_e and T_e were interpolated for many spatial points across the measurement region, for each time-slice. The ionisation rate for the helium with respect to the penetration depth was estimated using,

$$\frac{\mathrm{d}n_{He}}{\mathrm{d}x} v_{th} = \langle \sigma_{He,e} v \rangle \, n_{He} n_e, \tag{5.1}$$

where n_{He} is the number density of helium ions, $\mathrm{d}/\mathrm{d}x$ is the rate of ionisation with distance, and $\langle \sigma_{He,e}, v \rangle$ is the electron-helium ion collision frequency averaged over the Maxwellian, thanks to Bell et al. (1982). The jet was assumed to diverge conically by $30°$. The population of the $3s^1S$ level, which is the upper level of the transition, was estimated using the simple coronal model (section 4.1.1),

$$n_i = n_{He} \ \exp - \frac{\Delta E}{k T_e}, \tag{5.2}$$

where n_i is the population of the level, ΔE is the energy gap between the $3s^1S$ level and the ground state, and k is Boltzmann's constant.

The density of the excited state was taken to be proportional to the emission and the shape of the emission profile was predicted. Figure 5.1 shows the calculated profile normalised to and plotted against the measured profile. The predicted profiles match the measured profiles fairly well. Any discrepancies could be due to the assumptions made in the calculated profile. The level of the calculated light on the

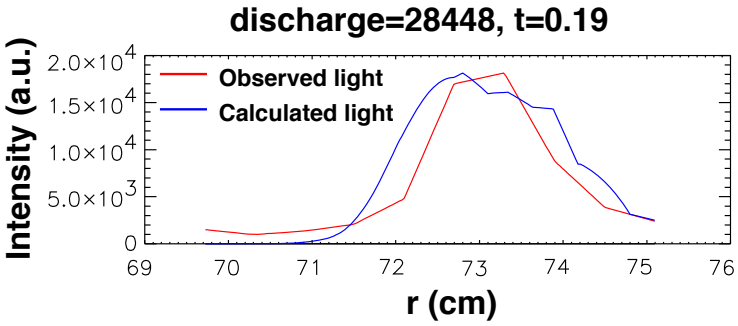

(a) *For a time-slice during which the discharge is in L-mode.*

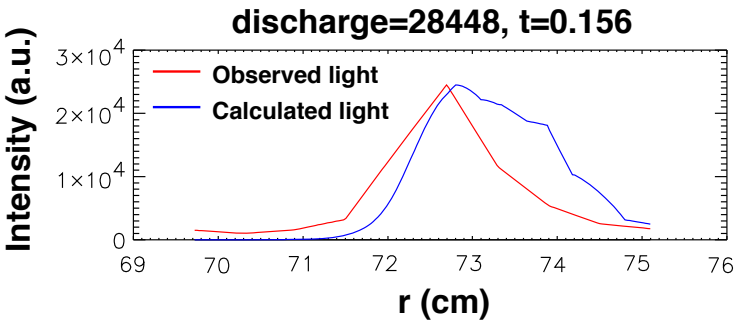

(b) *For a time-slice during which the discharge is in ELM-free H-mode.*

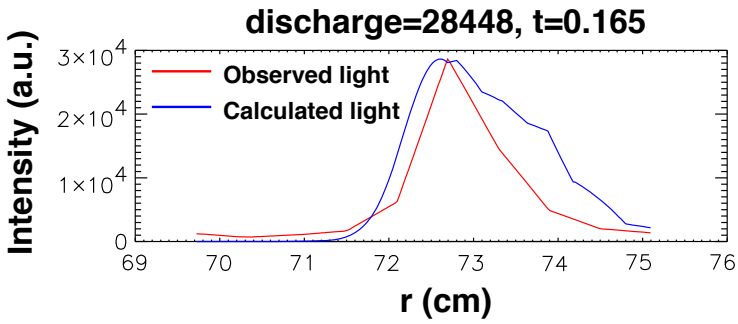

(c) *For a time-slice during which the discharge is in ELMy H-mode.*

Figure 5.1: *Emission profile of the* $667nm$ *Helium line shown with the predicted emission profile from the analysed data.*

outboard side of the peak in the profile is consistently higher than for the observed light. A simulation was run with the ionisation rate set higher than predicted by equation 5.1. Results showed that the peak and inner edge of the emission shell moved further out without significantly reducing the predicted signal level on the outer edge of the profile. A more likely explanation for the discrepancy is that the coronal model used for the excitation rate lacks sufficient sophistication to accurately predict the excitation rate. It is interesting to note that the emission profile is narrower in H-mode than in L-mode and most narrow for ELM-free H-mode for both the observed and calculated profiles, which supports the validation of the HELIOS data.

5.2 Benchmarking of HELIOS results

Benchmarking of a helium beam diagnostic similar to HELIOS has been previously performed by Schweer et al. (1992), who compared T_e profiles from ECE, n_e profiles from an HCN- interferometer, a $20kV$ Li-beam diagnostic, and a laser ablation diagnostic, with profiles from the thermal He-beam diagnostic on TEXTOR. Schweer et al. (1992) found good agreement between the diagnostics, which lends confidence to our analysis.

Thomson Scattering (TS) (Hutchinson, 1987) is a commonly used diagnostic that supplies multi-point, multi-time n_e and T_e measurements. The diagnostic consists of a high powered laser with a short pulse length and a spectrometer which measures the intensity and line broadening of the light scattered by the electrons in the plasma. A set of optics is placed so that a number of viewing chords intersect the beam as close to orthogonally as possible and are focused on sections of the beam. The scattered light is broadened by the kinetic electron motion convolved with the instrument function of the spectrometer (Carolan et al., 1998), T_e can be extracted by measuring the broadening of the spectral line (Griem, 1974) and n_e can be calculated from the emissivity (Meyer et al., 2000).

During this investigation, two separate TS diagnostics were implemented on COMPASS-D (Private communication, M J Walsh). The earliest of the two diagnostics was a core TS system that measured T_e and n_e over up to 9 vertically aligned points around the magnetic axis, above the centre of the plasma. The second system, which was implemented towards the end of this investigation, measured the same parameters over a region on the same vertical axis but on up to 10 points close to the nominal separatrix.

Figure 5.2 shows a contour plot of normalised, poloidal flux, ψ_N showing the

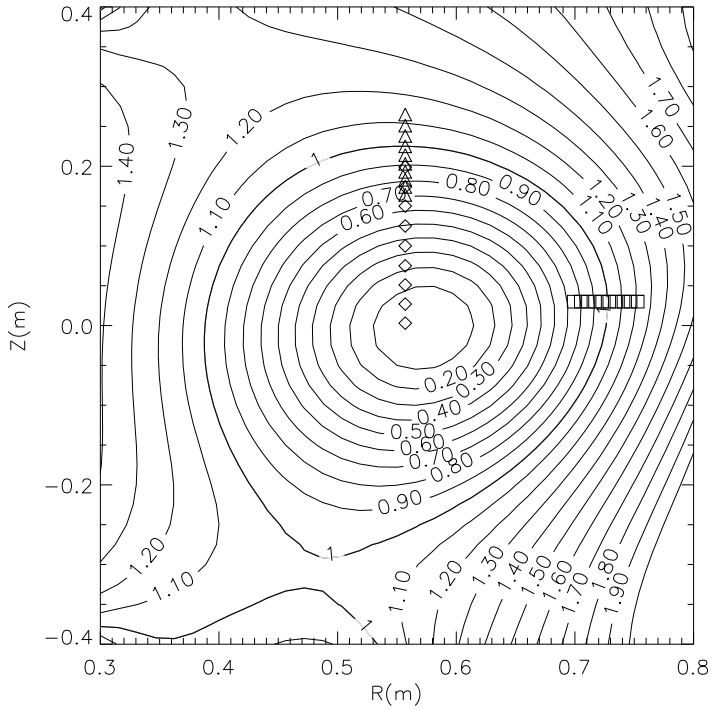

Figure 5.2: *Contour plot of ψ_N for discharge* 30865 *at time=* $170ms$ *showing the locations data is taken for HELIOS (□), core TS (◊), and edge TS (△).*

locations of the data points for HELIOS, and both TS diagnostics. Comparison of diagnostics on the same flux surface is possible because n_e and T_e are flux quantities to the first order (section 1.3) since electrons can move freely at thermal velocity along magnetic field lines. As can be seen, core TS had very little overlap in flux space with HELIOS and so correlation was not possible. The profiles were plotted together and typical results can be seen in figures 5.3(a,b,c,d). Figures 5.3(a,b), show the comparison of data from discharge number 28448, which was taken before the installation of the FLC shutter, (section 3.3). The data from HELIOS appears physical and reasonable over a narrow range of points between $\psi_N \approx 1.0 - 1.2$. As was explained in section 5.1, the strength of the spectral lines is dependent on the ionisation rate and excitation rates to the atomic levels of interest. Outside the region where the spectral line is strong, the relative random errors (section 4.8.1) are higher than in the strong signal region and the instrument is more susceptible to the systematic errors due to the *smearing* described in section 3.3.1, which affects the outer measurements most strongly, and the *swamping* of the signal caused by helium recycling described in section 4.8.2 that affects the inner chords most strongly.

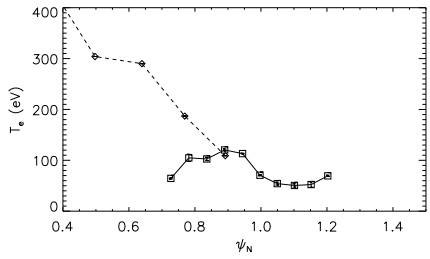

(a) *HELIOS and core Thomson Scattering T_e for discharge 28448.*

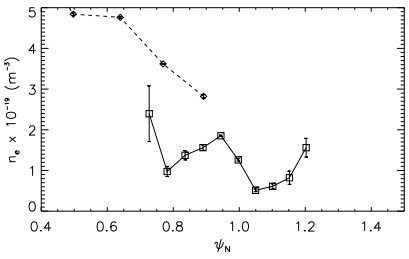

(b) *HELIOS and core Thomson Scattering n_e for discharge 28448.*

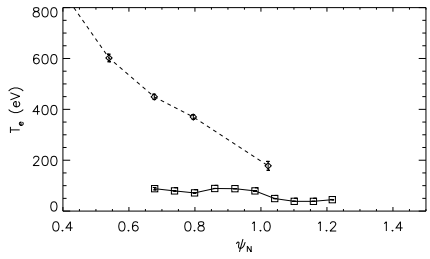

(c) *HELIOS and core Thomson Scattering T_e for discharge 29759.*

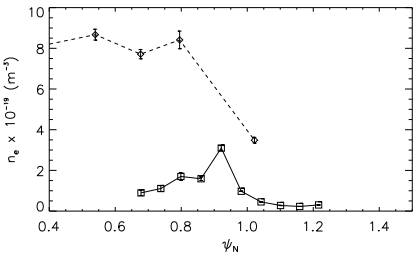

(d) *HELIOS and core Thomson Scattering n_e for discharge 29759.*

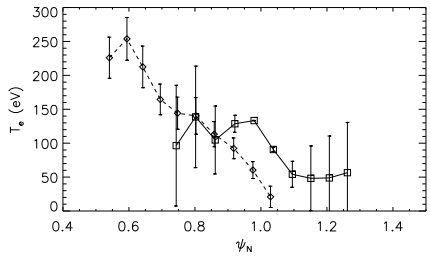

(e) *HELIOS and edge Thomson Scattering T_e for discharge 30930.*

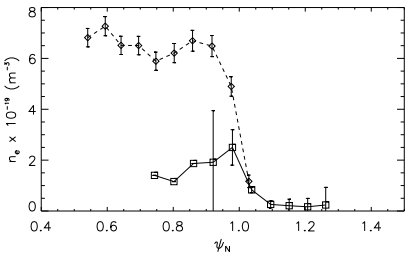

(f) *HELIOS and edge Thomson Scattering n_e for discharge 30930.*

Figure 5.3: *Comparison of n_e and T_e results from HELIOS (□), core TS (◊), and edge TS (△). The data is plotted against normalised flux.*

Figures 5.3(c,d) show the data for core TS and HELIOS for discharge number 29759. This data was taken immediately following the installation of the FLC shutter, (section 3.3.1). The spatial smearing problem that affected the outer chords has been alleviated but the *swamping* of the signal for the inner chords is still limiting the achieved penetration.

The final set of comparisons, figures 5.3(d,e) utilised the edge TS system that was installed towards the end of this investigation. The back pressure used for the plenum (section 3.1) was lowered to $\approx 1bar$, to reduce the total influx of helium into the plasma, reduce the helium recycling, and alleviate the *swamping* effect. In this case, the lower influx caused a reduction in line strength resulting in larger statistical errors. In the case of the inner n_e results which have no error bars, the errors were so large that they exceeded the limits of the look-up table (section 4.4) and no error could be calculated.

A statistical analysis comparing the results from HELIOS and edge TS was conducted over many shots and the results are represented in figure 5.4. The comparison of T_e appears good. The correlation is high (0.82) and the points are well clustered around the $T_e(HELIOS) = T_e(TS)$ line shown as the diagonal dashed line. In keeping with figure 5.3e, at low temperatures, the values for T_e from HELIOS are consistently higher than those from TS. For higher temperatures, which correspond to points further into the plasma, where the relative errors are higher, the error bars are very large. The comparison of n_e shows good correlation (0.83) although HELIOS measures consistently lower n_e than TS, with the discrepancy getting worse at higher densities.

The reason for the imperfect correlation is most likely due to inaccuracies in the equilibrium reconstruction (section 1.3.2). The errors in EFIT on COMPASS-D were never quantified, however a variance in space of $2mm$, which is within the expected error bars of EFIT (private communication, L Appel, UKAEA), would result in a range in normalised poloidal flux of ≈ 0.02 which, as can be seen from figure 5.3 can account for a difference of up to 50% in either T_e or n_e in the edge region of the plasma.

Upon inspection of the HELIOS spectrometer, the cause for the discrepancy between HELIOS and edge TS became apparent. The FLC shutter that was installed to reduce spatial smearing and allow access to faster time resolution had developed patches of damage, presumably due to the generation and migration of ions in the liquid crystal (section 3.3.1). Patches of the shutter had become translucent and failed to change phase when biased.

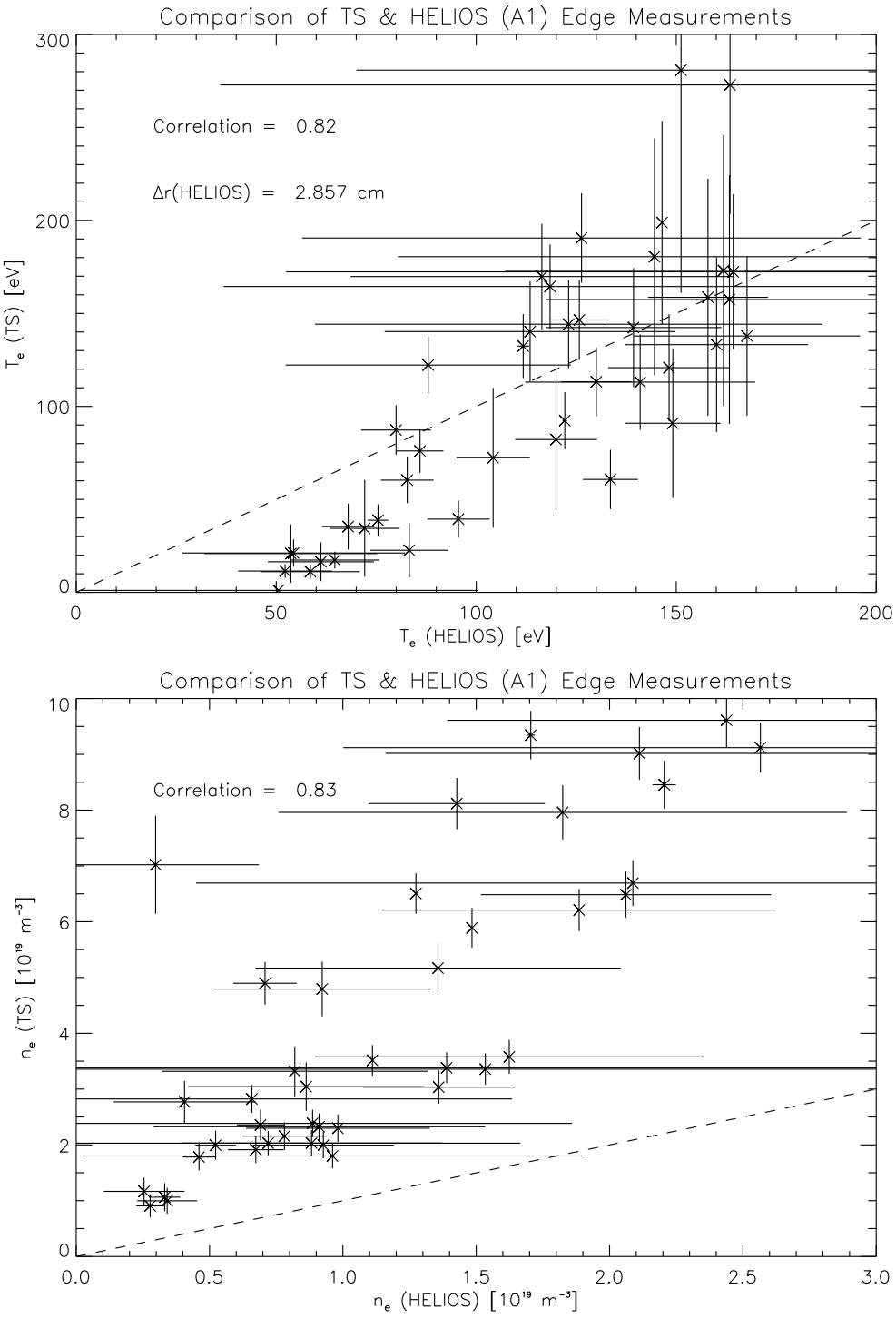

Figure 5.4: *Statistical comparison of HELIOS and edge Thomson scattering results. Thanks to Anthony Field.*

A calibration was performed after it had become known that the shutter was damaged and it was found that the mean relative change to the sensitivity ratios were, $\Delta R_1 = 1.25$, $\Delta R_2 = 0.79$. These systematic errors would cause HELIOS to measure T_e to be too high and n_e to be too low, in agreement with the trends observed. The agreement between HELIOS and TS at high temperatures is the result of the combination of two competing systematic errors. As explained in section 4.8.2, the *swamping* of the helium signal by radiation from re-cycled helium tends to result in low results for both T_e and n_e, the combination of this error and the artificially high results for T_e, from the shutter damage, resulted in rough agreement with the TS results.

Due to the second calibration being performed when the HELIOS diagnostic was connected to MAST, thereby utilizing different optical fibers and lens, and a lack of knowledge of the rate at which the damage had occurred and when it started, it is impossible to correct for the error.

Data from experiments that were conducted immediately after the installation of the shutter are unaffected by the damage as the shutter was tested and inspected thoroughly before use. Measurements from later in the investigation are reliable as a relative measure of n_e and T_e; as can be seen from figure, 5.4, the results correlate well. For the measurement of the radial electric field, as described in section 4.7, the electron density scale length $L_{n_e} = (\nabla \ln n_e)^{-1}$ is required. The natural log term makes the scale length relatively insensitive to changes in the electron density or density gradient of less than an order of magnitude. The scale length measurement and therefore the electric field measurement can be used with confidence.

5.3 Initial results from the HELIOS-CELESTE hybrid

The HELIOS-CELESTE hybrid was used to show the changes in edge parameters as the discharge evolved from L-mode to H-mode and back. (Meyer et al., 2000; Carolan et al., 2001). Figure 5.5 shows plots of various plasma parameters for discharge number 28448. The abscissa is $\sqrt{\psi_N} \sim r/a$. The vertical lines correspond to the 90%, 95%, and 100% flux surfaces. To illustrate the various phases of the discharge, the D_α emission is plotted vertically at the side of each plot. The horizontal lines mark the transitions from L- to H-mode and from H- to L-mode. The data is plotted at the end of each signal-integration interval to avoid confusion with the causality of events.

During discharge number 28448, the plasma is in L-mode during the first part of

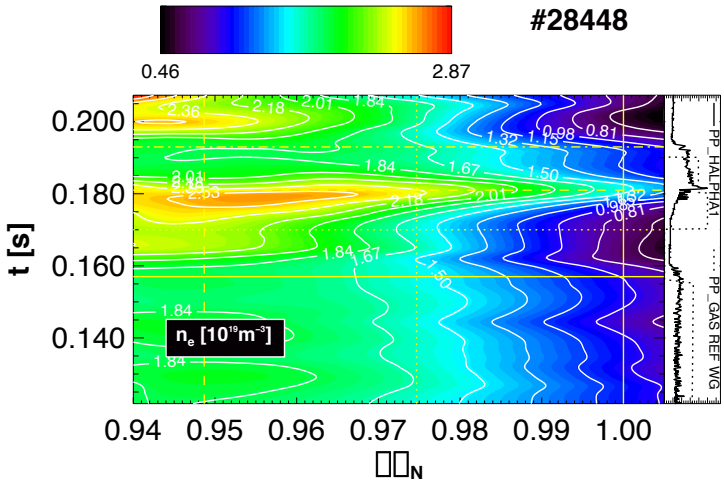

(a) *Evolution of n_e.*

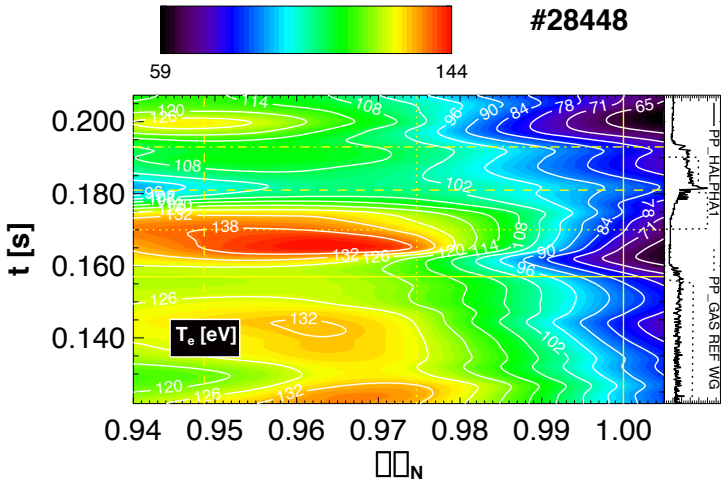

(b) *Evolution of T_e.*

Figure 5.5: *Evolution of various plasma parameters during discharge number 28448. D_α emission is also shown.*

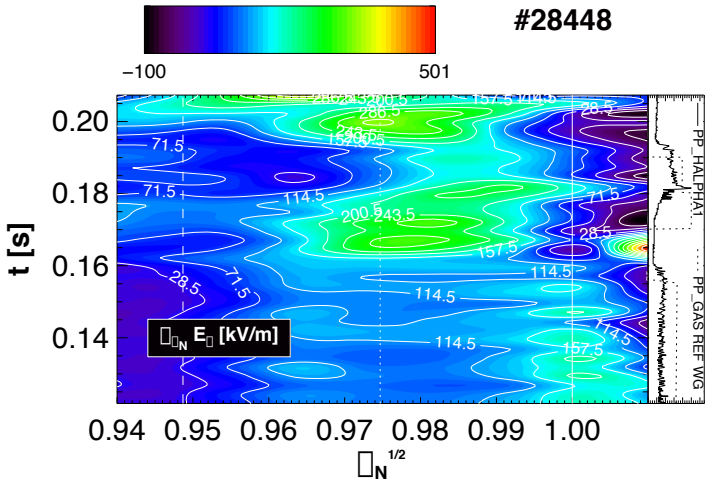

(c) *Evolution of* E'_{ψ}.

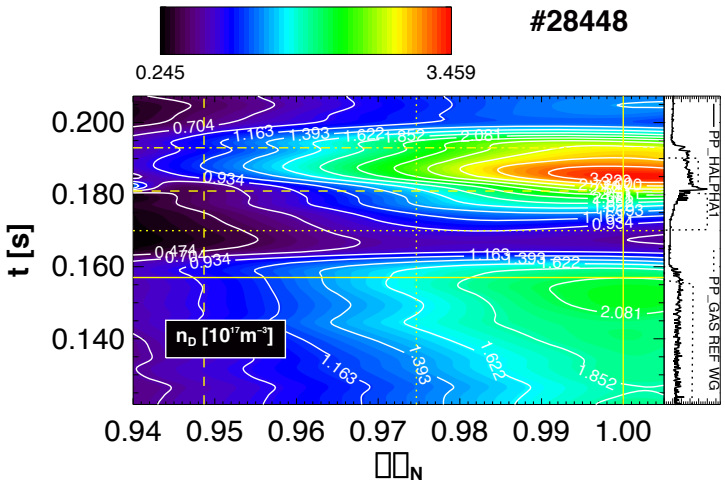

(d) *Evolution of* n_D.

Figure 5.5: *Evolution of various plasma parameters during discharge number 28448.* D_α *emission is also shown. (cont.)*

the data window. At $t \approx 160ms$, there is a steepening of the temperature and density gradient, associated with the transition into H-mode, that lasts until $t \approx 180ms$. The discharge returns to H-mode at $t \approx 190ms$. The formation of the pedestal in n_e and T_e can be seen to occur after the transitions into H-mode with the collapse occurring before the transition back into L-mode. The evolution of the electric field shear is shown in figure 5.5c. Within the confined region, E_ψ points inwards *i.e.* is negative, with higher values in the H-mode phase and a maximum change of $\Delta E_\psi \approx 12kVm^{-1}$. The most striking feature of this data is that the electric field shear does not increase until after the transition into H-mode. The neutral density profile is shown in figure 5.5d. It can be seen that the profile extends further into the plasma during L-mode than in H-mode. This observation is expected as recycled neutral helium is ionised more quickly by the steep n_e profile.

The first attempt at intimately combining the two diagnostics yielded new insights into H-mode physics, particularly the role of the radial electric field in transport barrier formation.

5.4 Experimental ELM Studies

5.4.1 Behaviour of $\mathrm{d}P_e/\mathrm{d}\psi$ during inter-ELM periods

In section 2.6, the trajectory in parameter space that was previously thought to apply to type III ELMs was described. The theory describes the locations of the stability boundaries but does not specify the trajectory of the discharge through parameter space. Although the suggested trajectory is the most intuitive, experimental verification is required.

5.4.2 Results from HELIOS on COMPASS-D

Discharge number 29759, from COMPASS-D, was selected for in-depth analysis of inter-ELM behaviour. Various parameters of the discharge are shown in figure 5.6. This shot was particularly suitable as there was a long period of slow type III ELMs, where the inter-ELM time was $\tau_{\mathrm{ELM}} \approx 4 - 5ms$. The low frequency ELM activity coincides with the period during which HELIOS data was being taken ($0.138s - 0.166s$), at fast time resolution ($= 1ms$). The discharge was ECRH heated (Fielding et al., 1988) with 4, fixed frequency gyrotrons operating at $60GHz$, which is resonant at $\approx 2.14T$. For this discharge, the resonance was around the $\psi_N = 0.45$ surface. The total plasma current was $I_p = 190kA$. There was steadily increasing line averaged density ($\langle n_e \rangle$), as measured by the interferometer (Edlington and

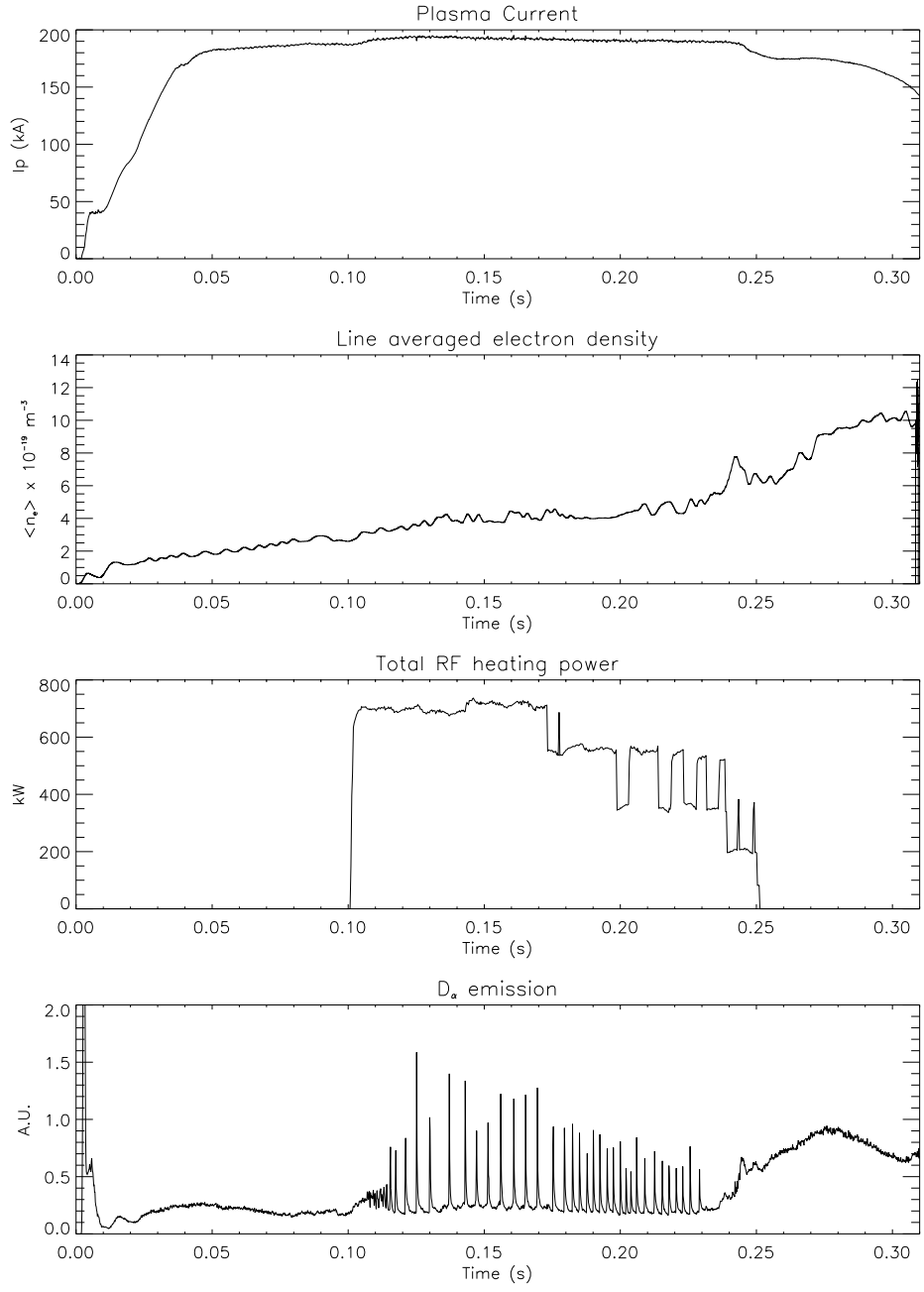

Figure 5.6: *Characteristics of discharge number 29759.*

Wylde, 1992). The ELM frequency was $\nu_{\text{ELM}} \approx 200 - 250Hz$, during the period of interest. A dithering H-mode begins at $\approx 0.11s$ with ELMing H-mode beginning at $\approx 0.13s$. At $t \approx 0.175$, the RF heating power decreases by $\approx 100kW$ and a clear increase in ELM frequency is seen, proving that the ELMs are type III. There is no period of ELM-free H-mode for this discharge and so the ELMs could not be the large type III ELMs discussed in section 2.3.

The data from HELIOS for this shot can be seen in figure 5.7. There are changes in the values, and gradients, of both T_e and n_e, between the ELMs. These changes occur on a relatively slow time-scale.

Profiles of the usable data from around the separatrix can be seen in figure 5.8. The data was mapped onto flux surfaces and fit with polynomials. The pressure and density profiles are fit with a forth order polynomial as this gave the best fit to the data in the region of interest. For the temperature profile, a quadratic was used as a higher order polynomial became unpredictable as a result of the T_e profile being somewhat flatter than that of P_e or n_e. Figure 5.8a shows data from $T = 0.1516s$, which is immediately after an ELM, figure 5.8b shows data in the middle of an inter-ELM period at $t = 0.1525s$, and figure 5.8c shows a time-scale immediately before an ELM, at $t = 0.1565s$. In section 5.2, the limitations of HELIOS due to the limited penetration depth of the helium, leading to *swamping* of the signal by background helium, is discussed.

For comparison of the data over multiple time-scales, values for the three parameters were taken at the ψ_{95} flux surface. The results are shown in figure 5.9a. The three parameters are fairly constant for the duration of the data, which suggests that the data is unaffected by variations in the helium penetration depth, which would affect the validity of points further into the plasma.

The edge gradients were calculated by taking the analytical differentials of the polynomial fits to T_e, n_e, and P_e. Figure 5.9b shows P'_e, T'_e and n'_e, where prime refers to the gradient with respect to ψ, at the ψ_{95} flux surface. Contrary to expectations, a drop in P'_e, was observed prior to the onset of each ELM.

The description of the method for calculating the errors for T_e and n_e can be found in section 4.8.1. For an estimate of the errors at ψ_{95}, a linear interpolation was performed between two points either side of ψ_{95}. To estimate the error in the gradient, the assumption was made that $dx/d\psi = \Delta x/\Delta\psi$ where x is one of the three parameters. It was assumed that there was no error in flux coordinate transformation.

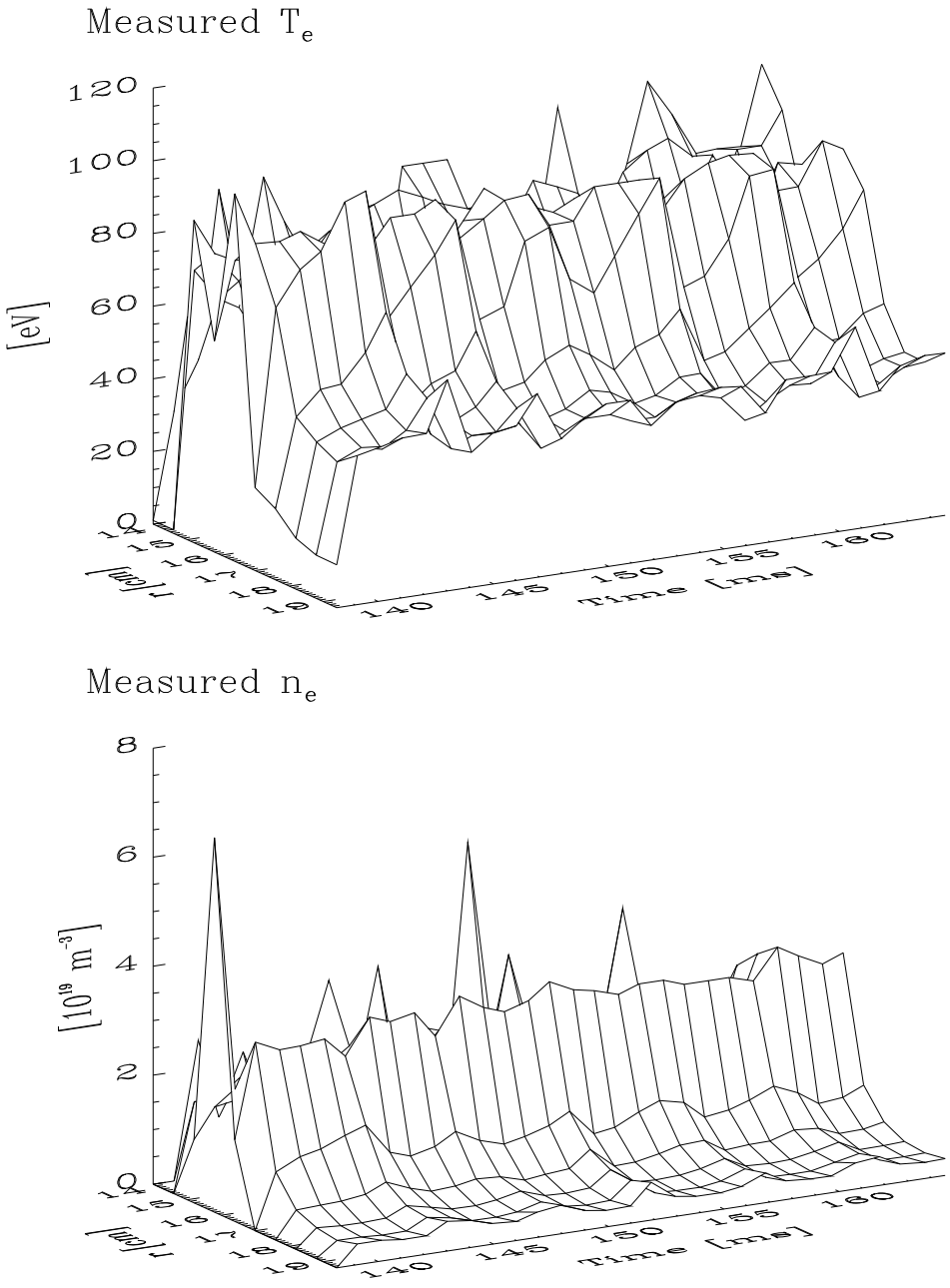

Figure 5.7: *Data from HELIOS for discharge* 29759. *Fluctuations in* T_e *and* n_e *can be seen clearly, on slow, periodic time-scales*.

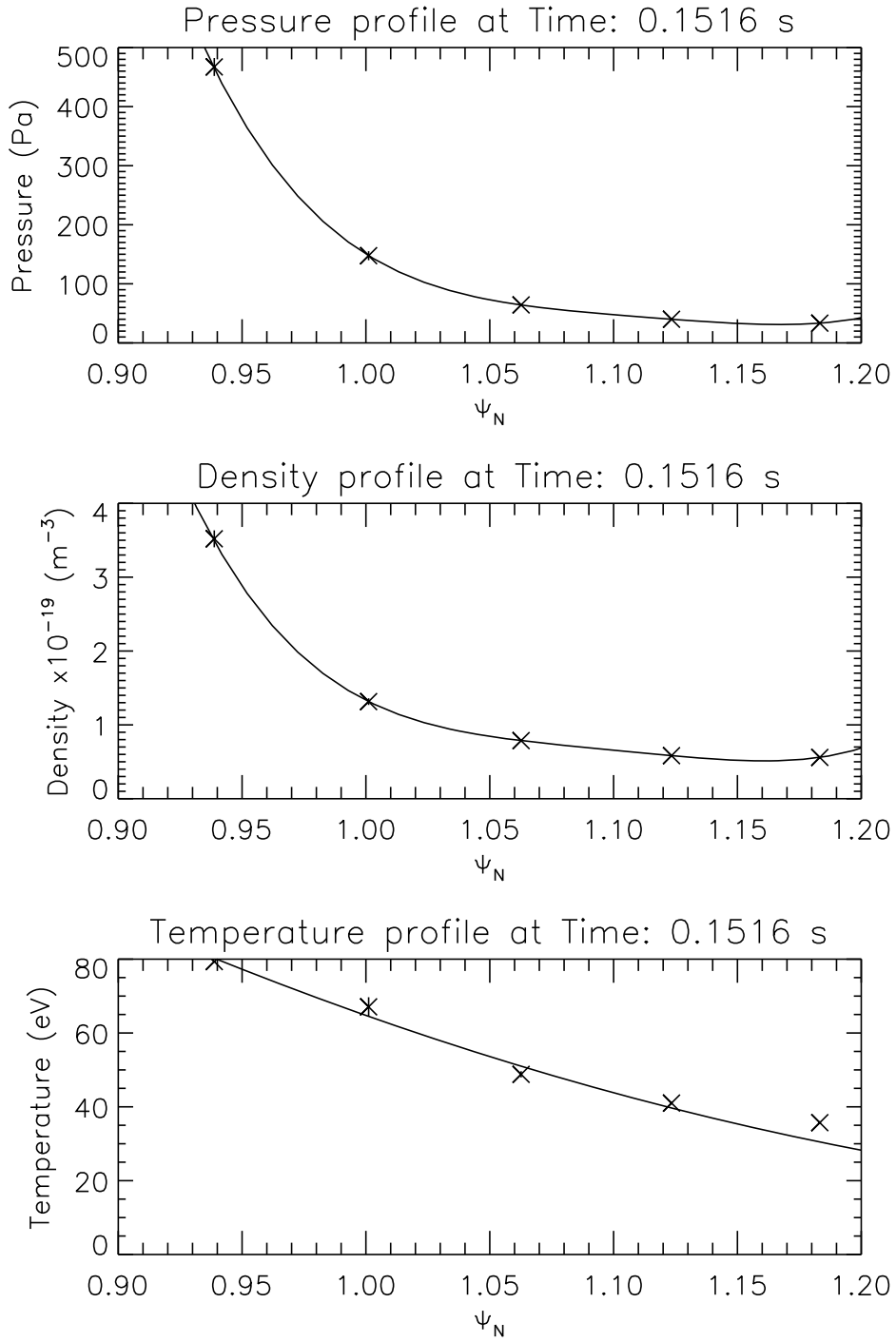

(a) *Time* $= 0.1516s$*, immediately after an ELM.*

Figure 5.8: *Profiles of* P_e*,* n_e*, and* T_e *from HELIOS plotted against* ψ_N *at various points during an inter-ELM period.*

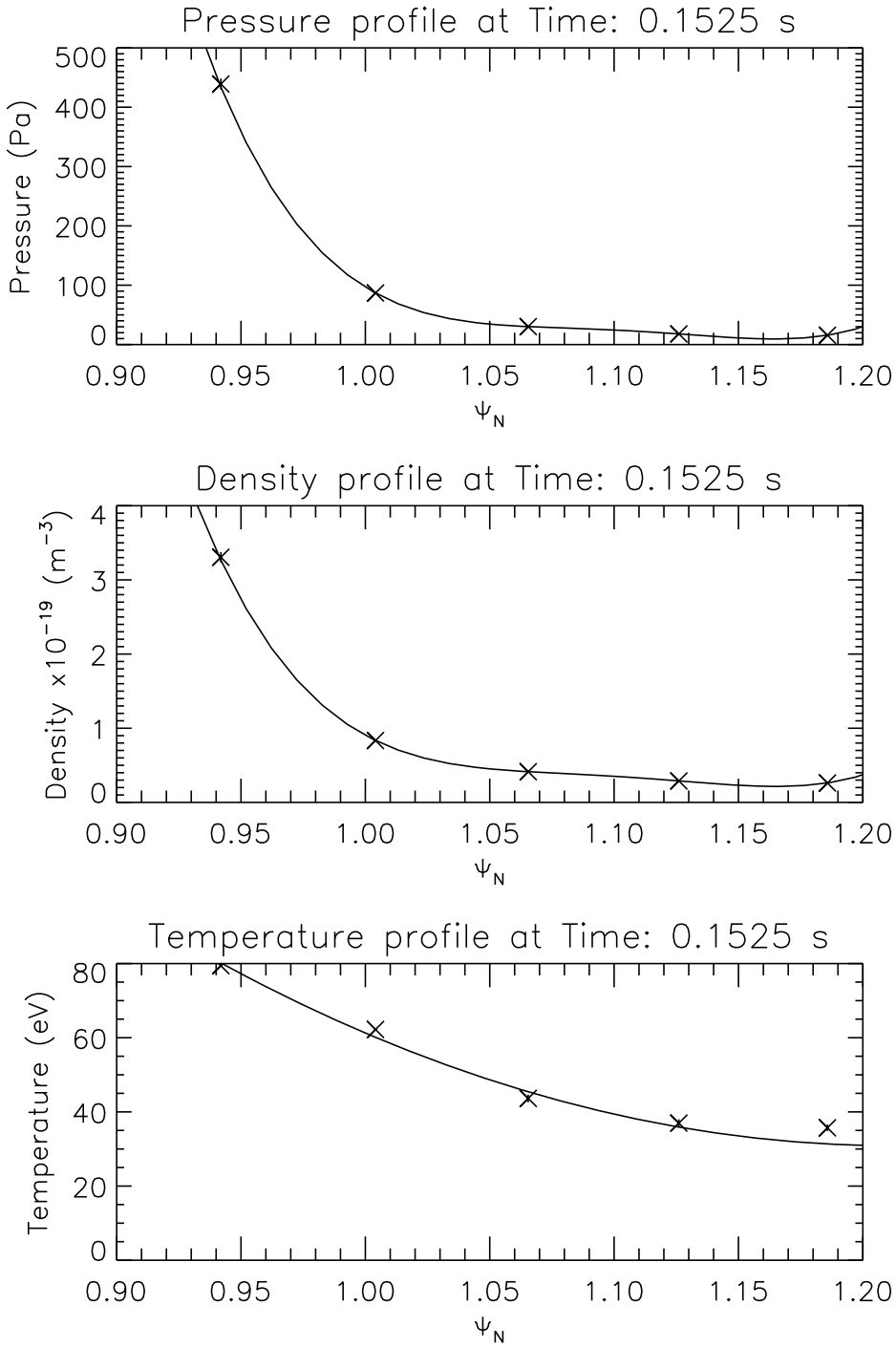

(b) *Time* $= 0.1525s$*, in the middle of an inter-ELM period.*

Figure 5.8: *Profiles of* P_e*,* n_e*, and* T_e *from HELIOS plotted against* ψ_N *at various points during an inter-ELM period. (cont.)*

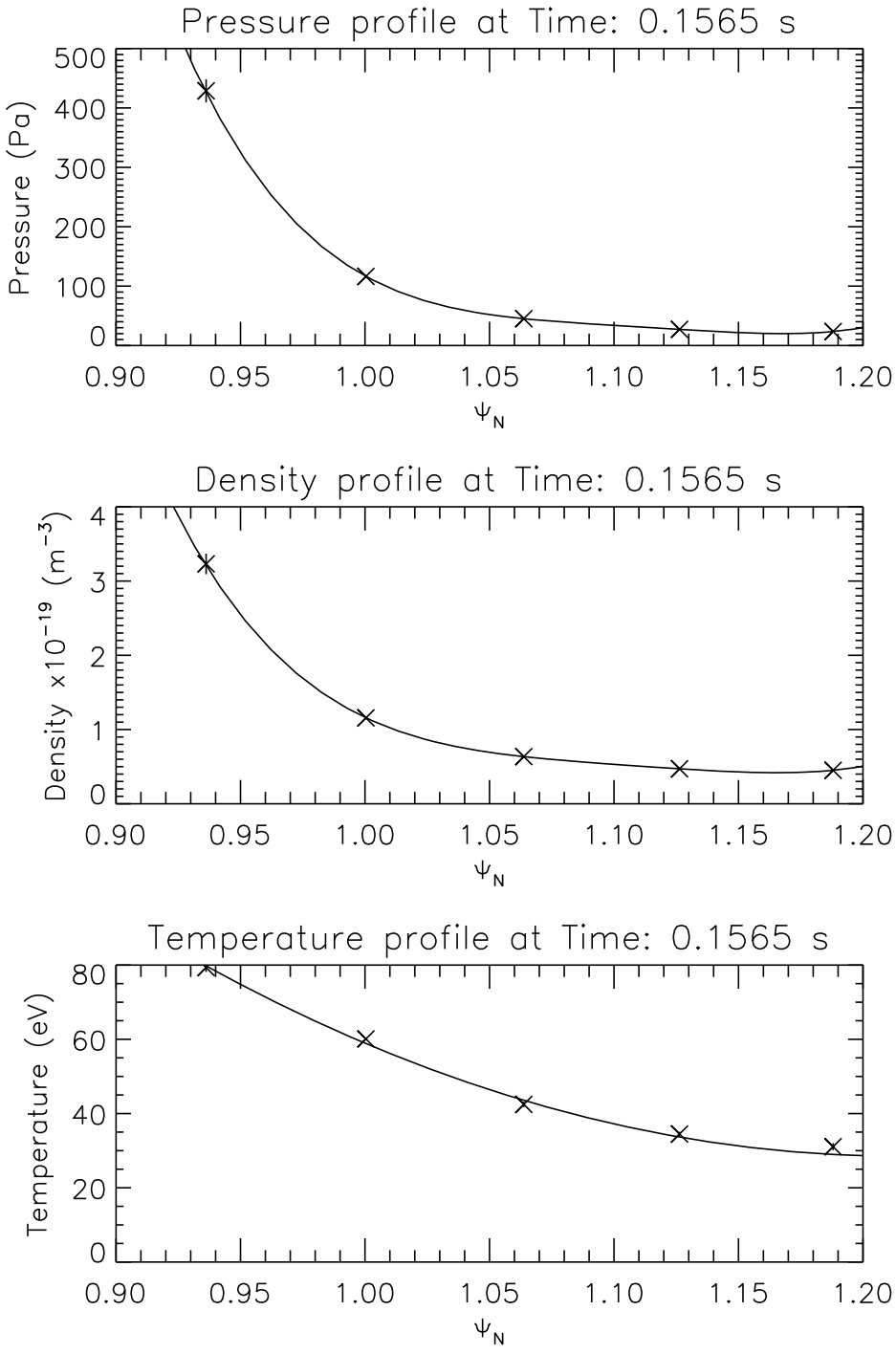

(c) *Time* $= 0.1565s$*, immediately before an ELM.*

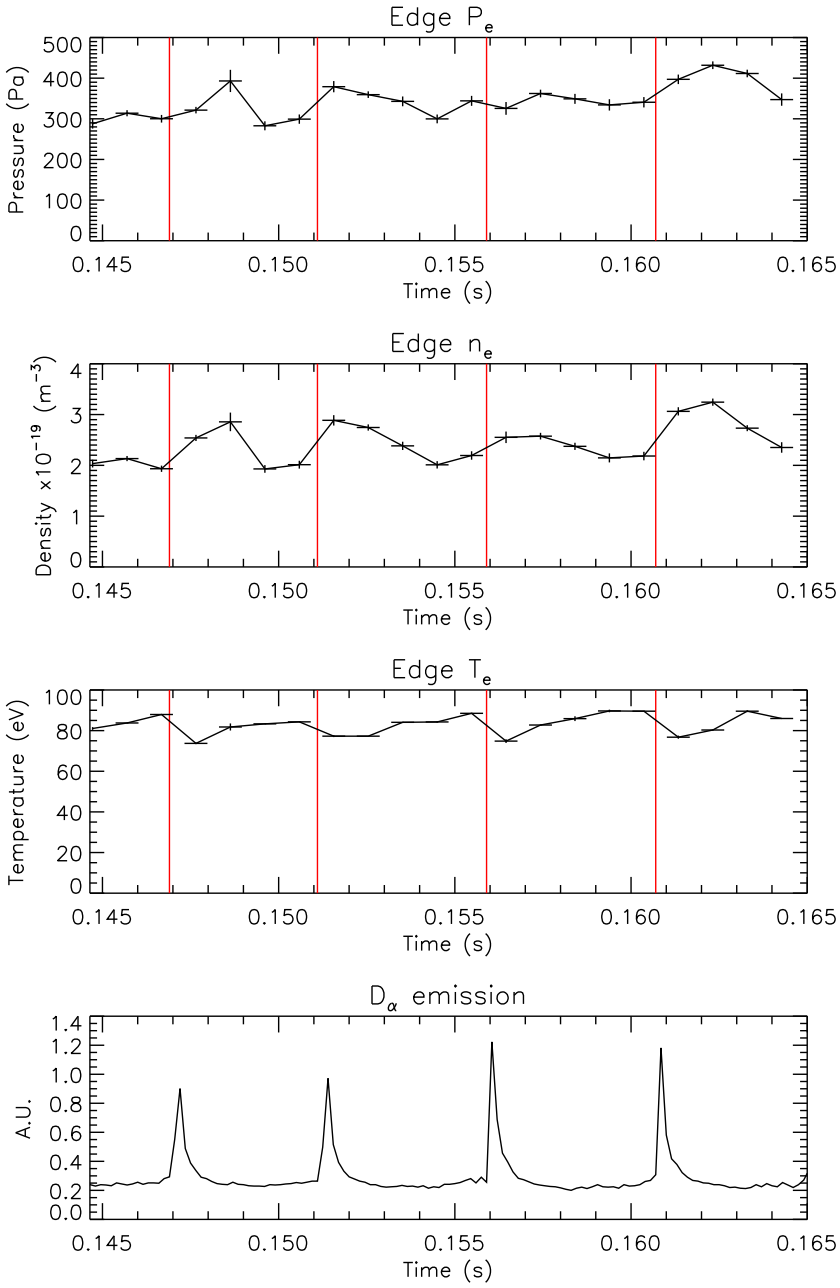

(a) *Evolution of the absolute values. Notice how the three parameters are fairly constant with n_e showing a slight fall before the ELMs.*

Figure 5.9: *Data from HELIOS showing the evolution of P_e, n_e, and T_e and the gradients of those, at the 95% flux surface. The horizontal bars show the time over which the data is collected. D_α emission is also shown.*

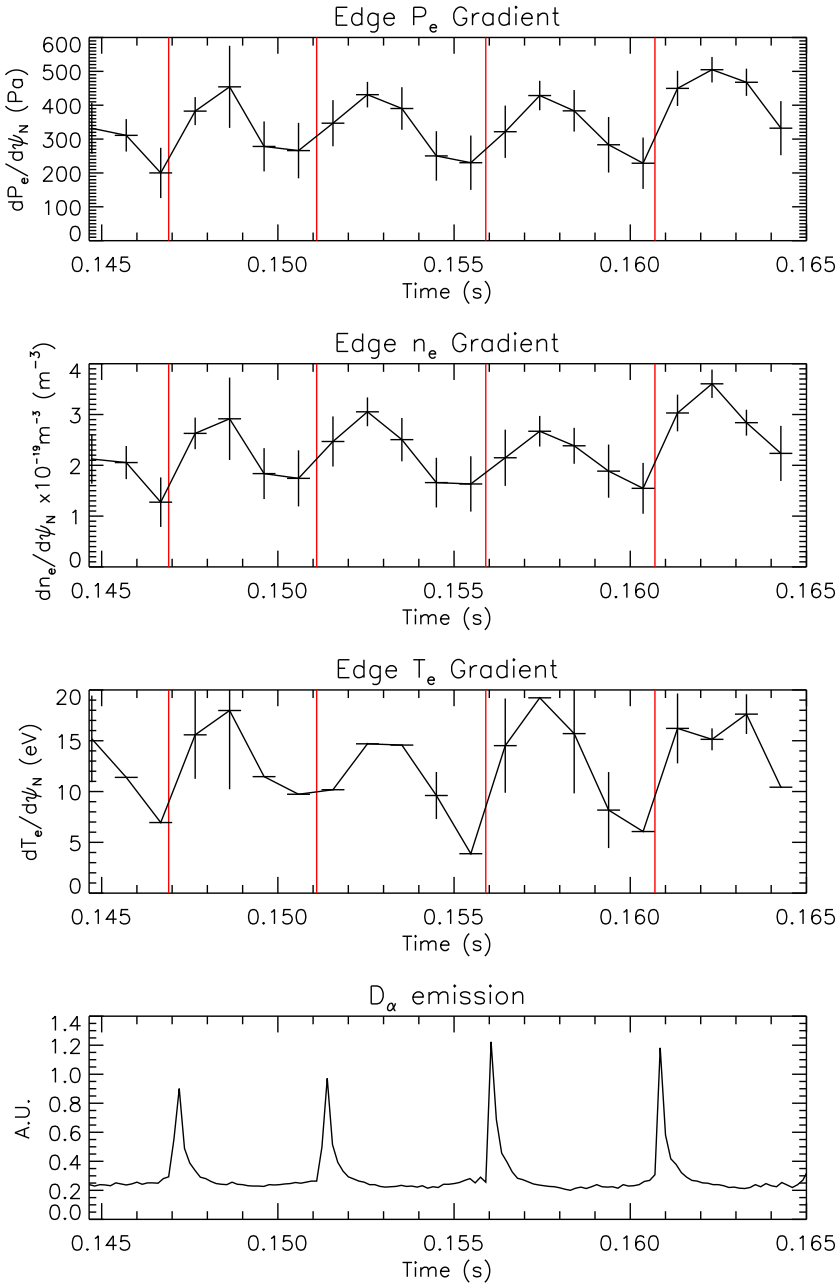

(b) *Evolution of the gradients. A drop in P'_e, n'_e, and T'_e prior to the onset of each ELM is clearly visible.*

The resulting error propagation formula becomes,

$$\sigma_{x'} = \frac{\sqrt{\sigma_{x_2}^2 - \sigma_{x_1}^2}}{\Delta\psi}, \tag{5.3}$$

(Bevington, 1969). This error was taken to be the error for all points over the region between the experimental points used.

The innermost points shown figure 5.8 correspond to the innermost points of HELIOS that were considered reliable. It is worth noting that the data may be affected by the *swamping* effect even though the data is increasing monotonically over the region. In this case, the results of all three parameters for the innermost point may be lower than the true values and so the data represents a lower limit for the innermost points and for the edge pressure gradient.

Immediately after each ELM, n_e' and T_e' rose in most cases, resulting in the peak in P_e' roughly half way through each inter-ELM period. In the period after *recovery* and prior to the next ELM, n_e' and T_e' fell causing a drop in P_e'.

5.4.3 Energy loss during the ELMs

The diamagnetic loop is a magnetic diagnostic which measures the toroidal magnetic flux, which can be integrated to yield the toroidal magnetic field. The energy stored within the plasma can be calculated from a force balance between the magnetic field and kinetic pressure (Wesson, 1997) (Castle et al., 1996). Figure 5.10 shows the plasma energy as measured by the diamagnetic loop. In the upper graph, energy is plotted along with D_α emission to show that there is a drop in the plasma energy after each ELM. In the lower graph, the energy is shown as a function of time, relative to the nearest ELM, for each ELM shown in the upper graph. As can be seen, the drop in energy appears to take place during the millisecond following the onset of the ELM. Although this might imply that there was a slow loss of energy, in fact, there is a smoothing function applied to this signal to remove the noise generated by the $500Hz$ ripple on the toroidal field coil power supplies. This smoothing function is sufficient to cause the drop in energy to be *smeared* over $1ms$. In conclusion, there is a drop in plasma energy associated with the ELMs but the temporal resolution of the diagnostic is insufficient to draw any conclusions about the timing of the event.

It is interesting to compare the energy loss from the ELMs as measured by the diamagnetic loop, to an estimate of that which might be expected due to the change in edge density gradient shown in figure 5.9b. Taking the change in pressure gradient at the ψ_{95} surface, a variation in pressure at the top of the pedestal can be estimated

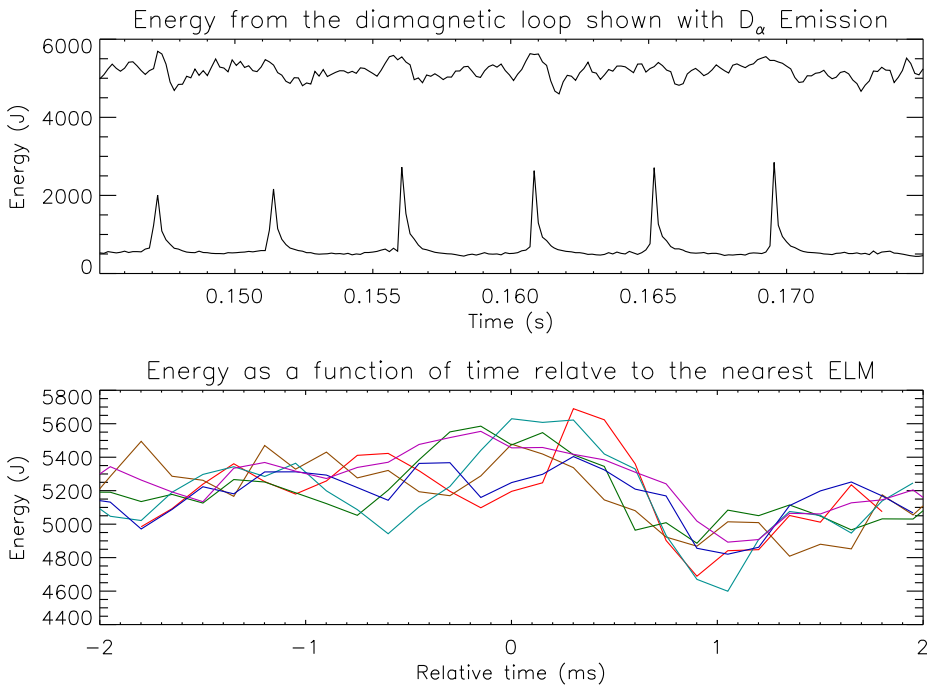

Figure 5.10: *Plasma energy as measured by the diamagnetic loop. The energy appears to drop during the millisecond after each ELM. The time delay is most probably caused by smoothing of the data.*

to first order. $\Delta P = 1.5kPa$. If the pedestal is assumed to be a separate confinement region, the change in pressure can be considered uniform over the entire plasma and as such the change in energy is calculated simply by,

$$\Delta W = \Delta PV, \tag{5.4}$$

where ΔW is the variation in energy over the ELM period. Using this method a change in energy of $\sim 12\%$ is estimated. As can be seen from figure 5.10, the above result is in rough agreement with the data from HELIOS. Although it should be noted that the temporal resolution of HELIOS may be such that the rapid energy loss caused by an ELM cannot be detected. In this case, the agreement between the diamagntic loop and HELIOS may be partly co-incidental.

5.4.4 Thomson scattering measurements on COMPASS-D

To validate the results, Thomson scattering (section 5.2) data from a number of other discharges on COMPASS-D were used. The Thomson scattering diagnostic does not have fast time resolution and so direct measurement of the inter-ELM pressure gradient is impossible. Several nominally similar ERCH heated plasma discharges (30863, 30864, 30865, 30866, 30868, 30869, 30870), with slow type III ELMs, recorded in succession, were used. Details of the discharges are given in the table below.

Discharge #	$I_p(kA)$	$\langle n_e \rangle\,(m^{-3})$	$P_{\text{ECRH}}(kW)$	$\nu_{\text{ELM}}(Hz)$
30863	170	2.6×10^{19}	0.60	250
30864	170	2.4×10^{19}	0.57	150
30865	170	2.2×10^{19}	0.58	200
30866	170	2.0×10^{19}	0.72	200
30868	170	2.3×10^{19}	0.72	300
30869	170	2.2×10^{19}	0.70	300
30870	170	2.2×10^{19}	0.71	300

Since the times of the ELMs are not exactly the same for each discharge, the use of the same absolute time for Thomson scattering resulted in a series of time points, each relative to its nearest ELM. The results can be seen in figure 5.11. The data from HELIOS is also shown in the figure and has been normalised to the Thomson scattering data so that the behaviour of T_e', n_e', and P_e' as measured by the two diagnostics can be easily compared.

As can be seen, there is a significant drop in the density gradient, although when compared to the results from HELIOS, the onset appears to take place much later. There is also a possible late drop in T_e' although the error bars are too large to be certain.

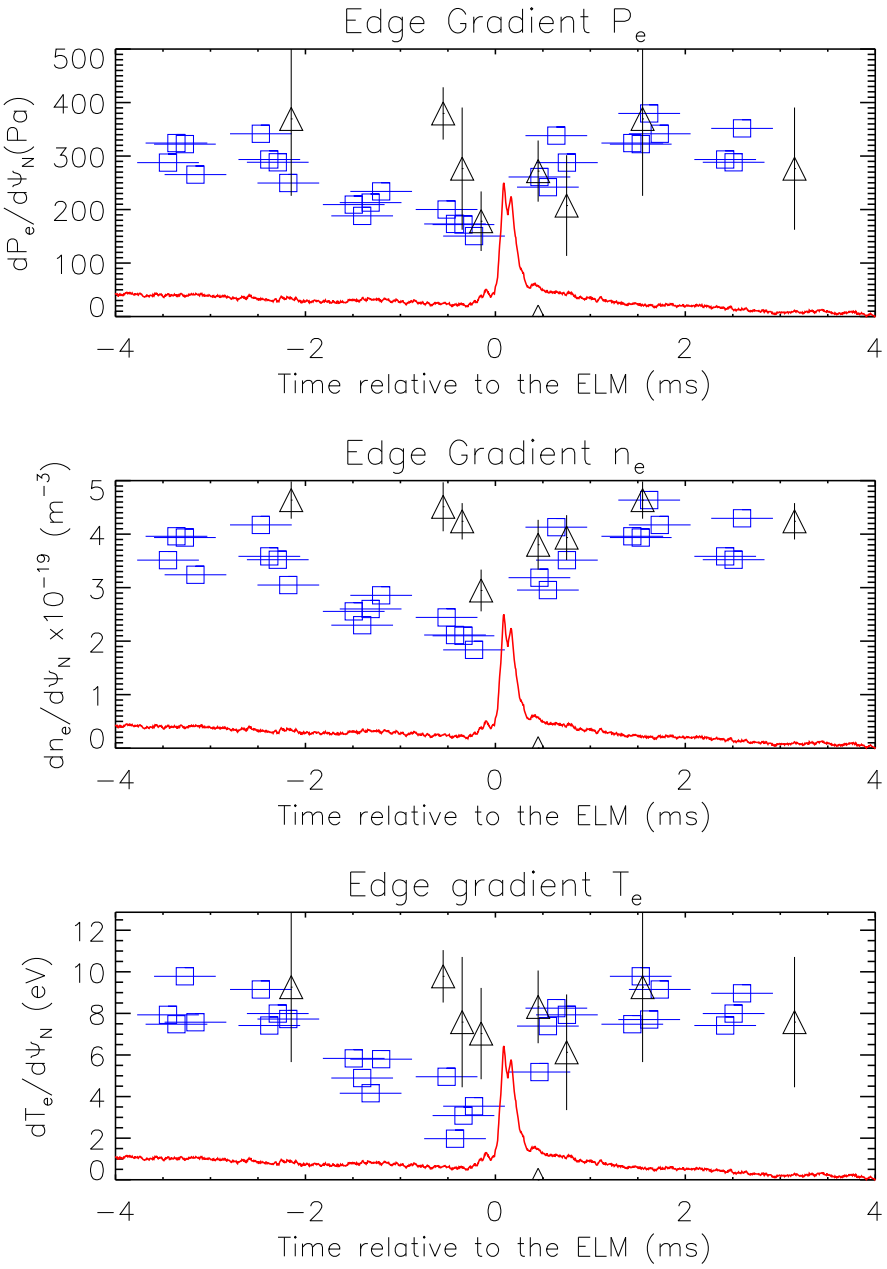

Figure 5.11: *Comparison of P_e', n_e', and T_e', from Thomson scattering (△) and HELIOS (□). The data or Thomson scattering was taken from shots;* 30863, 30864, 30865, 30866, 30868, 30869, *and* 30870. *The HELIOS was taken from shot* 29759.

In conclusion, the data from the shot to shot Thomson scattering analysis supports the measurements made by HELIOS.

5.4.5 Results from MAST

A dedicated Linear Camera for the measurement of edge density gradient was implemented on MAST by Tournianski et al. (2001).

Because of the fast time-scales involved and the uncertainties over the exact timing of the data points, it was necessary to correlate the total intensity from the linear camera with the intensity from the fast D_α camera that was used to show the times of the ELMs.

A series of NBI heated discharges (Akers et al., 2000) with slow type III ELMs were analysed, the details of which are presented in the table below. Plots of n'_e, along with D_α are shown in figure 5.12.

MAST Discharge #	$I_p(kA)$	$\langle n_e \rangle\ (m^{-3})$	$P_{\mathrm{NBI}}(kW)$	$\nu_{\mathrm{ELM}}(Hz)$
4415	800	2.0×10^{20}	0.88	550
4472	930	1.6×10^{20}	1.10	400
4477	950	1.7×10^{20}	0.97	300
4512	580	1.7×10^{20}	1.69	250
4537	750	2.0×10^{20}	1.60	N/A
4540	770	2.2×10^{20}	1.67	350
4558	780	2.3×10^{20}	1.67	200-300
4559	750	2.5×10^{20}	1.67	170

In figure 5.12a, a clear drop in n'_e can be seen prior to the beginning of each ELM. In each case, a gentle drop in n'_e was observed preceding the ELM, followed by a sharper drop that took place at the beginning of the ELM event, to within the time resolution of the diagnostic. This data is compatible with the data taken by HELIOS on COMPASS-D (figure 5.9b), where the steady drop was seen but the sharp loss of gradient at the ELM happens on a shorter time-scale than the resolution of HELIOS.

Figure 5.12b shows the data from discharges that did not display the same behaviour. In these cases, n'_e could not be seen to drop significantly before the onset of each ELM. During discharge number 4559, a slight drop was seen prior to the second ELM but the decline was in line with the general trend at that time.

In all but one of the first set of discharges, $\langle n_e \rangle$ is 30% lower than in the second set. The NBI heating power (P_{NBI}), is significantly lower in all but one of the discharges that did display a drop in n'_e before the ELMs ($P_{\mathrm{NBI}} \approx 0.9 - 1.1kW$) than for the discharges that did not display the phenomenon ($P_{\mathrm{NBI}} \approx 1.6 - 1.7kW$). The second set of discharges had less regular ELMs than the first. In some cases, it was

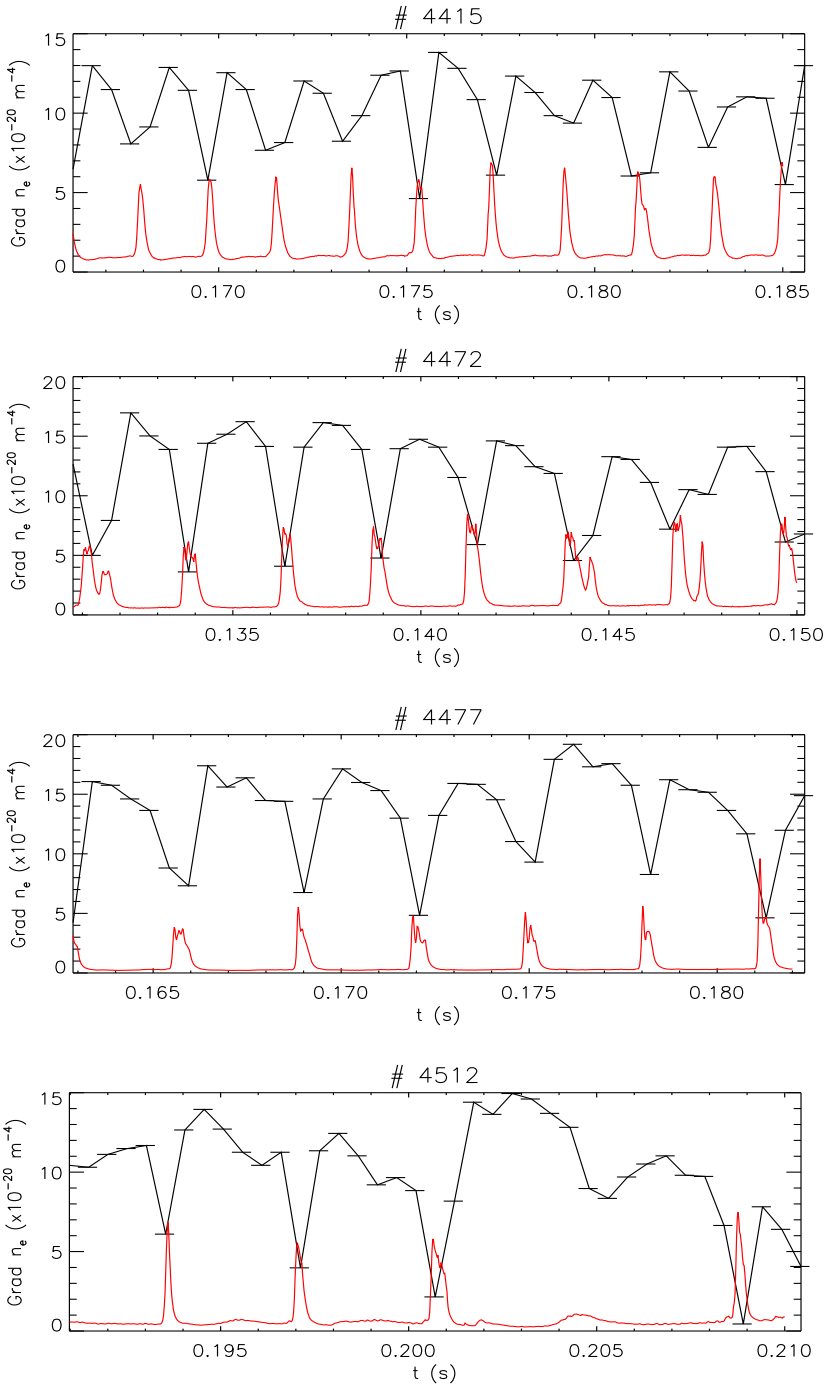

(a) *These data show a drop in n'_e prior to the ELMs.*

Figure 5.12: *Data from the Linear camera on MAST (black),shown with D_α emission (red).*

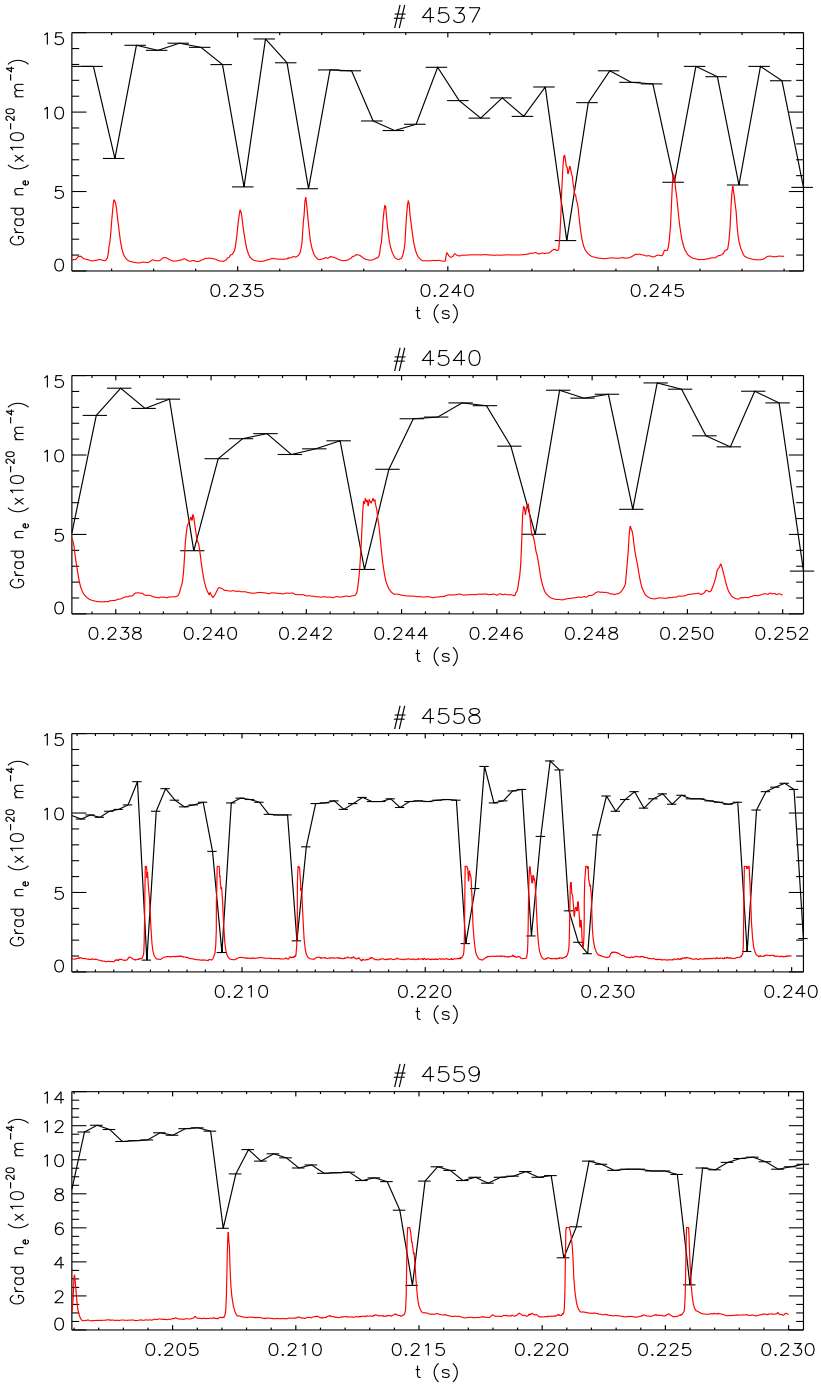

(b) *These data do not show a drop in n'_e prior to the ELMs.*

Figure 5.12: *Data from the Linear camera on MAST (black),shown with D_α emission (red). (cont.)*

difficult to define an ELM frequency and for the case of discharge number 4537, the ELMs were so irregular that no value for ν_{ELM} could be identified.

Although it is not possible to identify a single parameter that separates the two sets of discharges, it may be possible that the low P_{NBI} of discharge 4415 mitigates the higher $\langle n_e \rangle$.

The two contrasting sets of data show that n'_e, and therefore possibly P'_e, sometimes fell prior to the onset of ELMs but that the drop was not an inherent feature of type III ELMs on MAST.

5.5 Conclusions

The emission profile of the $667\ nm$ helium line, was compared to a calculated profile, using a simple coronal model. The profiles agreed fairly well. A discrepancy between the calculated and measured level of light on the outer side of the profile might be explained as a result of the assumptions used in the coronal model. The favourable outcome of this self-consistency check lends certainty to the analysis method.

A statistical comparison of the HELIOS and Thomson scattering diagnostics was performed over many discharges. The results were relatively good, with correlations of 0.82 for T_e and 0.83 for n_e. A systematic under-estimation of n_e by HELIOS, by a factor ≈ 3.6 was found, compared to Thomson scattering. The cause of the systematic error was most likely a degradation in the FLC-shutter that was installed to increase the temporal resolution of HELIOS. The results for discharge number 29759 were taken immediately after the installation of the shutter and are considered reliable. Results taken after are considered acceptable as relative measures of the parameters. The electric field calculation can be used with confidence as the parameter scale lengths are used.

Data from the Thomson scattering diagnostic of the T_e and n_e profiles was gathered on a shot-to-shot basis to supply multiple time-slices relative to an ELM event. This study showed a drop on the density gradient prior to the onset of the ELMs although the time-scale of the drop was different to that observed by HELIOS. There was a possible drop in the T_e gradient but the error bars were too large for a statistically significant result. Differences in time-scale may be due to differences in other, unidentified plasma parameters.

Data from the linear camera on MAST showed some discharges that demonstrated a drop in n'_e prior to ELMs. Other discharges did not show the drop. This observation suggests that edge pressure gradient can drop prior to the onset of type II

ELMs but it is not an inherent feature of the phenomenon.

5.6 Further Work

It would be interesting to see if a cause for this drop in edge pressure could be found. Initial attempts to find a cause have focused on the Mirnov magnetic detector coils, although no candidate MHD activity has been found. It is thought that a resistive ballooning mode might have been the cause for this drop, which would tie in with the lack of magnetic evidence as resistive ballooning modes can be electrostatic in nature and therefore undetectable using magnetic coils.

A cause of the drop in edge pressure gradient might help explain why some discharges show the drop before ELMs and some do not. It might also be useful to conduct a larger scale experimental study on MAST in an attempt to identify the conditions under which the phenomenon occurs.

Chapter 6

Preliminary stability analysis of COMPASS-D discharge 29759

To better understand the role of instabilities in relation to ELMs in COMPASS-D, a stability analysis of discharge number 29759 was needed. As can be seen from chapter 2, stability analysis is complicated and no simple method exists to analytically assess stability. In this chapter, a preliminary attempt is made to analyse the stability of the discharge and a model is proposed for the behaviour of the discharge during inter-ELM periods.

6.1 The first attempt at generating the equilibria (GS2D)

It was necessary to reconstruct the plasma equilibria (section 1.3.2) so that factors like plasma shape could be considered. For this stability analysis, it was important to account for changes over time to the edge pressure gradient. The first attempt at this involved reconstructing equilibria for each time-slice that incorporated the measured pressure profile. Pressure data for the edge was taken from HELIOS and for the core, the core TS diagnostic described in section 5.2 was used. Although the TS diagnostic does not have fast time resolution, the assumption that the core pressure is constant over several ELMs is justified. Type III ELMs are small edge phenomena that eject particles and energy only from edge (Snyder et al., 2002). Data from TS for a time during the ELMy H-mode ($t_{TS} = 0.164s$) was used.

Several difficulties were encountered when using GS2D. GS2D is a free boundary code, meaning that it changes the shape of the separatrix in order to converge, making it difficult to converge a stable, physical solution. It is also very computationally intensive, in terms of determination of the metrics for stability calculations.

GS2D contains no model for the bootstrap current and so to correctly specify the

profile of ff' (equation 1.14), the equilibrium would need to be iteratively solved until a consistent solution was found.

Despite much effort to resolve these issues, it was eventually decided that the solution to these problems would be better resolved by using an equilibrium solver that had a model for the bootstrap current built in and was less computationally intensive, thereby allowing greater resolution. Full details of the first attempt to generate the equilibria are presented in appendix A.

6.2 Second attempt at generating the equilibria (SCENE)

The SCENE (Simulation of Self-Consistent Equilibria with Neoclassical Effects) numerical code (Wilson, 1994) was used in a second attempt to ascertain the equilibria. Like GS2D, SCENE is an equilibrium solver however there are several important differences. SCENE is not a free boundary code. Instead, values for the major radius (R), inverse aspect ratio ($\epsilon = r/R$), triangularity (δ), and elongation (κ) are given together with the magnetic field at the magnetic centre of the plasma. A series of parameters that specify the shape of the ion density and temperature profiles with the function

$$x = x_{\text{edge}} + \left(x_{\text{ped}} - x_{\text{edge}}\right)\left[\frac{E^2-1}{E^2+1}\right] + x_c\left\{(1+\psi_N)^{\alpha_x} - (1+\alpha_x\psi_N)\right\}, \quad (6.1)$$

where

$$E = \exp\left\{\lambda_x\left(1 - \frac{\psi}{\psi_N}\right)\right\}, \quad (6.2)$$

are also input. In the above, x is either n_i or T_i. The ion temperature profile was calculated using the electron temperature profile and the Artsimovich scaling law (Artsimovich, 1972a). The ion density profile was estimated from the electron density profile, by assuming quasi-neutrality, with the mean atomic number taken to be $Z_{eff} = 2$.

The first term in equation 6.1 is the value of the parameter at the edge. The second term gives the shape of the pedestal region, with x_{ped} being the value at the top of the pedestal. This term is a $\tanh$ function similar to that invoked in the previous section, with λ_x being the width of the pedestal. The third term of equation 6.1 is a power law that describes the shape of the core region of the plasma. When $\alpha_x = 1$, the term disappears and the entire profile becomes a $\tanh$ function. For values of α_x greater that 1, a peaked profile is the result; values of less than 1 generate a hollow profile.

This method of representing the profile shape is very much more flexible than EFIT's simple polynomial fit and allows proper representation of the edge pedestal however the method does not have the flexibility that the method employed by GS2D has, as SCENE cannot be supplied with an arbitrary pressure profile. The extra rigidity of the SCENE code has both advantages and disadvantages. The code is computationally much less demanding, which allows for higher resolution of the output equilibrium. Since the boundary is fixed, it becomes easier to make alterations to the profiles without making the output equilibrium unphysical. In addition, SCENE contains a model for the pressure driven current and so the profile of ff' is properly specified in the equilibrium (Section 6.2.1). The key disadvantage of the code is that fine tuning of the edge pressure gradient to match the pressure profiles of each time-slice becomes difficult. Figure 6.1 shows the raw temperature and density data together with the profiles that were generated using equation 6.1 and used to generate the equilibrium for time-slice $t = 0.164s$.

Instead of using multiple time-slices to map out the stability boundary, a typical time-slice was chosen for stability analysis. As will be explained, perturbations were made to this typical time-slice in order to map out the stability boundary.

Figure 6.1 shows the raw temperature and density data together with the profiles that were generated using equation 6.1 and used to generate the equilibrium for time-slice $t = 0.164s$. As can be seen, HELIOS acts as a constraint on the edge T_e and also acts to define the edge density gradient. The limitations imposed by the particular function used by SCENE to fit the profiles means that the fit, especially in the core of the plasma, is not as good as a custom designed profile, making use of a modified tanh function, would be (Appendix A).

6.2.1 How SCENE calculates the current profile

In general, the driven current in a plasma discharge is known but additional current contributions from the bootstrap (section 1.4.1), diamagnetic and Pfirsch-Schlüter (section 1.4.2) currents, are not. The dependence of the total current profile on these contributors is dependent on the equilibrium configuration. This issue represents a circular logic problem and is the cause of the problems with specifying ff' for the GS2D equilibria, as mentioned in section 6.1.

The major advantage of SCENE over GS2D for this work is the presence of models for bootstrap, diamagnetic, and Pfirsch-Schlüter currents within the code itself. SCENE employs an iterative procedure whereby an initial guess at the total current profile is used to calculate the equilibrium. The total current profile of this equilib-

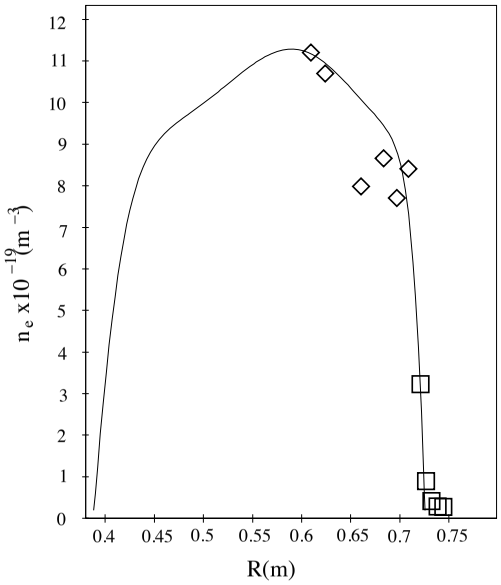

(c) *The raw density profile, shown as points with the fitted profile*

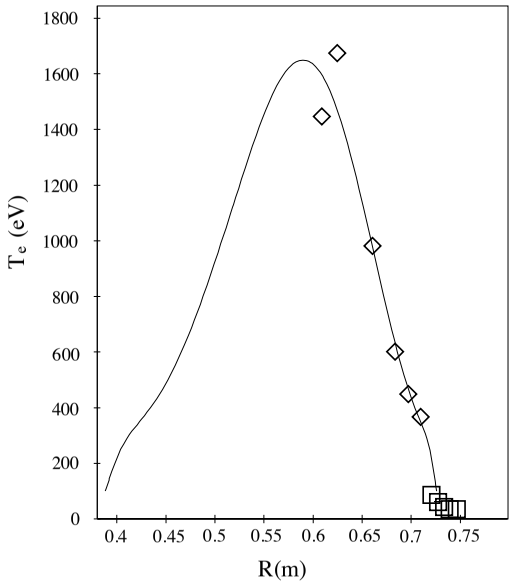

(d) *The raw density profile, shown as points with the fitted profile*

Figure 6.1: *The raw density and temperature profiles taken from HELIOS (□) and Thomson Scattering (◊) shown as points, together with the fitted profiles as described by equation 6.1 and used by SCENE to calculate the equilibrium for discharge* 29759*, at* $t = 0.164s$

rium, as the sum of the driven and intrinsic currents, is then compared to the initial guess. In general, the two profiles will be different and so a second equilibrium is generated using the updated current profile. This process is repeated until the current profile does not change by more than a specified accuracy, which in this case was 1%. Figure 6.2 shows the contributions to the current of the three internally generated current sources. Sub-figure 6.2d shows the externally imposed current that is induced by the magnetic field and the sum of the internally and externally generated currents.

6.3 Analysis of ballooning stability

The first step towards testing if the results from discharge number 29759 supports the ELM model explained in section 2.6 is to ascertain if the equilibrium is ballooning limited. In section 2.4.3, it was explained that the ballooning mode is a pressure driven instability that can represent a soft limit to the pressure gradient. The reasoning for the softness of the limit is that any loss of pressure gradient or edge current density will tend to stabilise the plasma. This is due to the shape of the stability curve shown in figures 2.8 and 2.9. A corollary of this observation is that it is impossible to approach the ballooning boundary by reducing P_e' and thereby reducing α. For a discharge where P_e' reduces prior to the onset of the ELM, as it does here, it is impossible for the equilibrium to be at the ballooning limit at the time of the ELM.

It is interesting to see how far away from the ballooning limit the equilibrium is. To this end, a numerical analysis was performed. The magnetic flux (ψ), as a function of r and z is output from SCENE as well as the pressure profile. A numerical code, IDBALL (based on the method proposed by Greene and Chance (1981)) was used to plot the $s - \alpha$ stability curves for the $n = \infty$ approximation to the ballooning limit (section 2.4.2), at varying values of ψ. The plots also show the values of α and s at the surfaces analysed. Four example plots that illustrate the results are shown in figures 6.3.

The analysis was conducted on 10 surfaces of ψ, between the ψ_{90} and ψ_{99} surface. The code is incapable of dealing with a separatrix and so analysis must be conducted up to but not including the plasma edge. Ignoring the last few flux surfaces could potentially cause errors in the analysis if these surfaces were unstable. In this case however it is the ballooning mode which is of interest which, as explained in section 2.4.3, is relatively radially extended. As such, the relevant flux surfaces are tested for stability by this method. All of the surfaces were shown to be in the stable region.

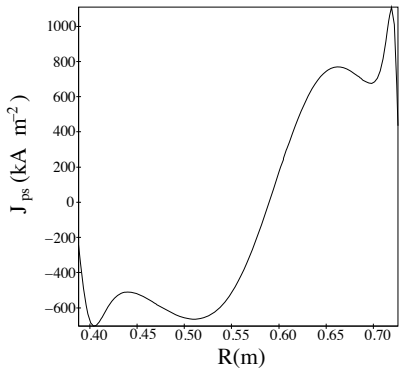

(a) *The Pfirsch-Schlüter current*

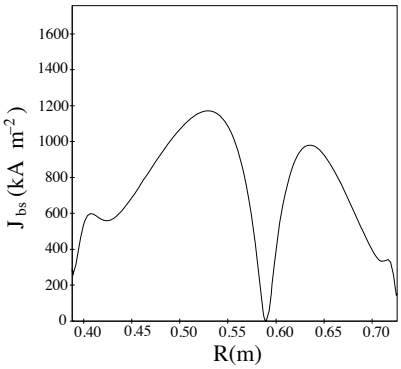

(b) *The bootstrap current*

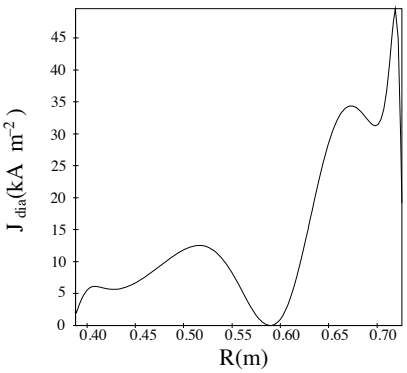

(c) *The diamagnetic current*

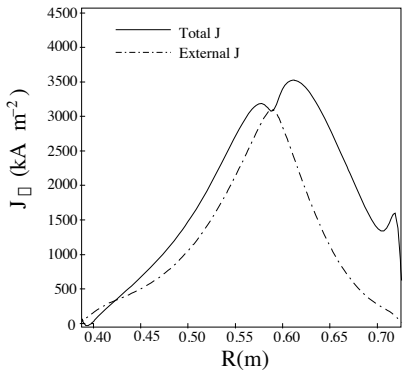

(d) *The total current (solid) and externally imposed current (dash-dot)*

Figure 6.2: *The internally generated current profiles and total current profile as calculated by SCENE*

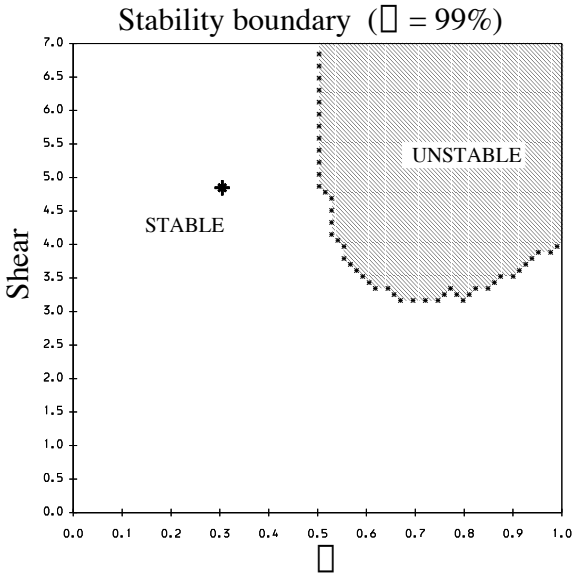

(a) *Stability analysis for ψ_{99} flux surface.*

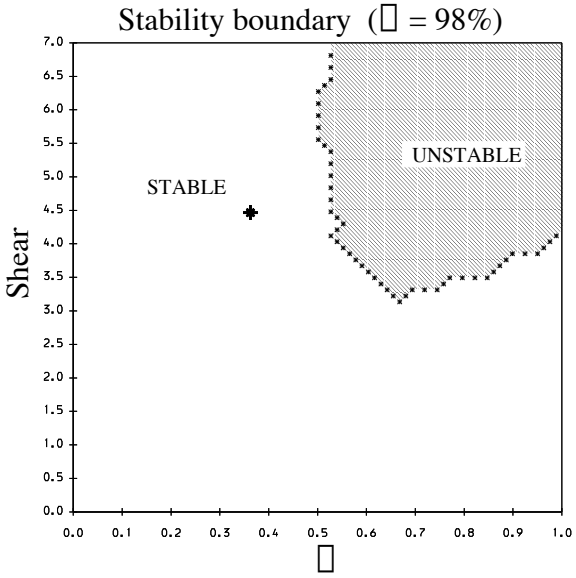

(b) *Stability analysis for ψ_{98} flux surface.*

Figure 6.3: *Results from the IDBALL numerical ballooning analysis showing that discharge 29759 is stable to the ballooning mode at $t = 0.164s$. The boundary between the $n = \infty$ ballooning stable and unstable regions are shown with the location of the plasma in $s - \alpha$ space.*

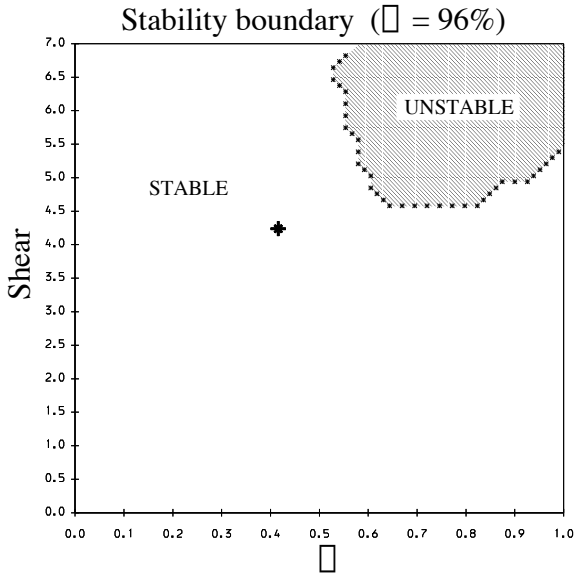

(c) *Stability boundary for ψ_{96} flux surface.*

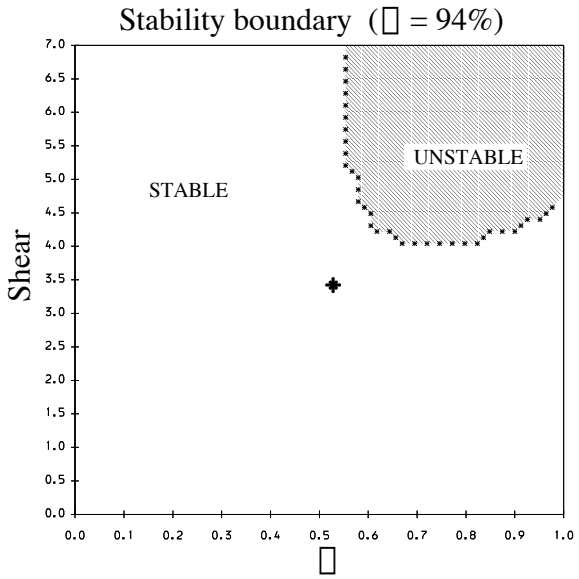

(d) *Stability boundary for ψ_{94} flux surface.*

Figure 6.3: *Results from the IDBALL numerical ballooning analysis showing that discharge 29759 is stable to the ballooning mode at $t = 0.164s$. The boundary between the $n = \infty$ ballooning stable and unstable regions are shown with the location of the plasma in $s - \alpha$ space. (cont.)*

As explained in section 2.4.5, for every value of edge current or shear, there are two marginally stable values of α. The lower value represents the upper limit of first stability with the upper value being the lower limit of second stability, leading to a forbidden region of instability. As can be seen from figure 6.3, for surfaces close to the separatrix, the plasma is in the region of first stability. Further into the plasma, the discharge has higher values of α, but the decreased shear allows the plasma to avoid the forbidden region of instability.

6.3.1 Analysis of peeling stability

The method for this analysis was similar to that used for the ballooning stability analysis except for the final step. Instead of using the IDBALL code to asses stability, the ELITE code (section 2.4.5) was used. ELITE (Wilson et al., 1999) is a numerical code that calculates the growth rates for the ideal eigenmodes of a particular equilibrium. From this, the stability to edge localised modes of any type, peeling, ballooning, or coupled peeling-ballooning, can be assessed.

The equilibrium for time-slice ($t = 0.164s$) was tested for stability using the ELITE code and found to be unstable. The value of $j_{\|}/\langle j \rangle$ for this discharge was 0.1983 and α was found to be 0.3019 using the IDBALL code. The eigenfunction of the instability can be seen in figure 6.4. As can be seen, the instability is concentrated at the edge with a single dominant mode. This mode is the one closest to the separatrix and therefore the discharge can be considered to be unstable to the peeling mode. The abscissa shows ψ_N rather than rational surfaces counted in from the separatrix, as was shown in figure 2.7, as the mode structure is more easily discernible in this case. By artificially removing current from the edge region of the discharge, the point of marginal stability was found ($j_{\|}/\langle j \rangle = 0.1745, \alpha = 0.2970$). It was necessary to alter the density profile by linearly scaling it to keep α constant to within two decimal places.

6.3.2 Curve of marginal stability

By scaling the density and then artificially manipulating the current at the edge of the plasma, a series of marginal stability points were found for the discharge. While testing for stability at low α, it was sufficient to test the stability of the closest mode to the separatrix as the current at the very edge of the plasma is what drives the peeling mode (section 2.4.4). At higher α, where ballooning and coupled peeling-ballooning modes are possible, it was necessary to check the stability of all likely modes, as

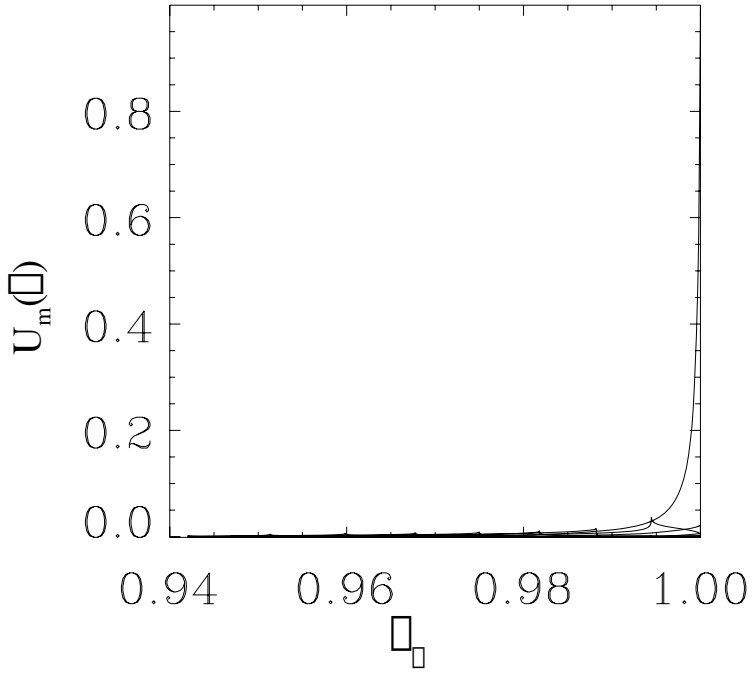

Figure 6.4: *Eigenfunction generated by the ELITE numerical code ($n = 6$). The dominant mode close to the separatrix indicates the peeling nature of the instability.*

these instabilities can be relatively radially extended into the plasma. In this case, up to and including $n = 20$ was considered sufficient.

It was hoped that the pressure could be increased to the point where the ballooning boundary could be found. Unfortunately, the equilibrium failed to converge when the pressure was raised significantly and so few points above the unperturbed equilibrium could be found. For all equilibria tested, the closest rational surface to the edge was the one found to be unstable. This result further supports the hypothesis that the ELMs were caused by the peeling mode.

Based on the belief that the discharge is far from the ballooning boundary, a linear fit to the marginally stable points was considered an acceptable way to establish a stability curve. For a pure peeling mode, the stability curve should be a straight line. Figure 6.5 shows the original unperturbed equilibrium ($*$) in $j_{\|}/\langle j \rangle$ - α space, the marginally stable values ($\diamondsuit$), and the linear fit to the marginally stable values.

There appears to be quite a large spread in the marginally stable values. This spread is due to the variable influence of the vacuum contribution to the stability equation (section 2.4.4) in the limiter approximation to the discharge. Points that are furthest above the straight line have their unstable flux surface very close to the

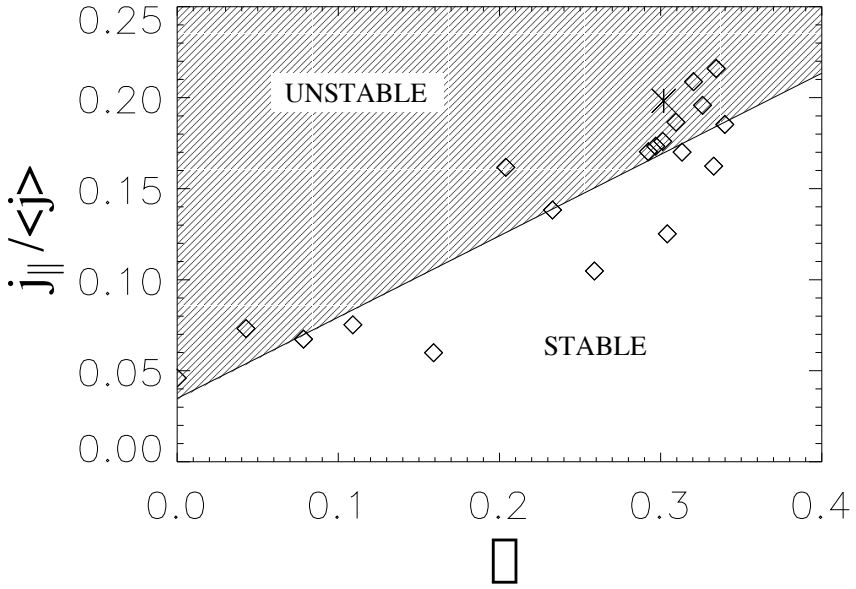

Figure 6.5: *Plot of marginal stability (◇) in α and $j_{\|}/\langle j\rangle$ space, fit with a straight line. The position of the unperturbed equilibrium is also shown (∗).*

plasma boundary, so that the vacuum appears to be heavily stabilizing. Those points further into the area marked as "STABLE" on the graph have their unstable flux surface comparatively deep into the discharge.

The fuzziness is an artifact of approximating the true, diverted equilibrium by discarding the extreme edge region to produce a limited plasma that can be modeled by SCENE/ELITE. This process discards the infinite number of flux surfaces, near the edge of the equilibrium, and leads to this apparent sensitivity to the exact value of edge q.

To verify this point, a study of the four most extreme points, that is points furthest from the linear fit, was performed to find their marginally stable values of $j_{\|}/\langle j\rangle$, without the vacuum contribution. The results can be seen in figure 6.6. From this figure, it can be seen that the points increase monotonically although the points do not lie in a good straight line.

There are two possible explanations for the points in figure 6.6 not being exactly linear. The form of $j_{\|}/\langle j\rangle$ output by SCENE is averaged over a flux surface. The form of $j_{\|}/\langle j\rangle$ used in the peeling criterion is averaged over a field line (equation 2.23). In a large aspect-ratio, circular approximation, these two quantities should be the same, however in a shaped plasma with finite aspect ratio, the flux surface average and field line average are generally not equal.

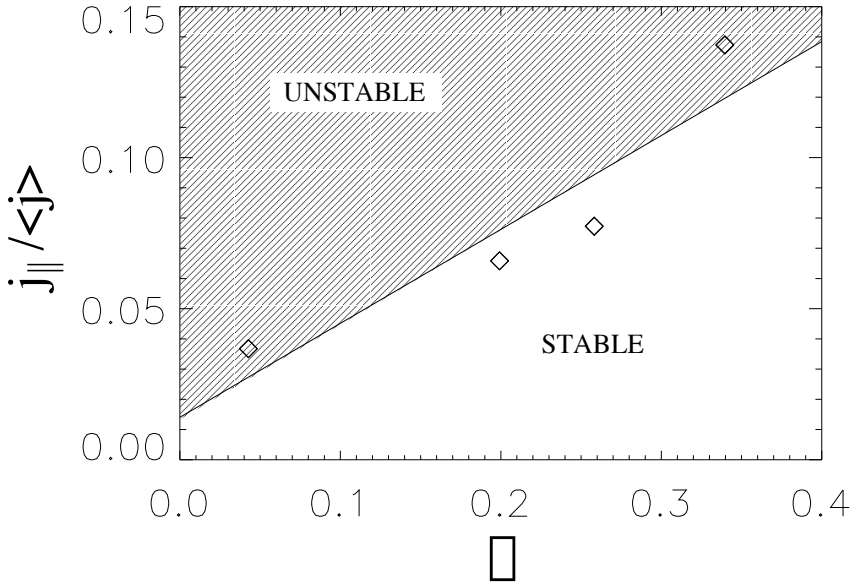

Figure 6.6: *Plot of marginal stability points with the vacuum contribution neglected for the most divergent points of figure 6.5*

A second problem is connected to the failure of the equilibrium to converge at high α. Scaling the pressure profile caused changes to the equilibrium itself, most noticeable was a movement of the magnetic axis of the plasma towards the outboard edge as the pressure increased. This phenomenon is known as the Shafranov Shift (Wesson, 1997). Changes in the equilibrium cause changes in the shape of the curve of marginal stability. It can be thought that the fit shown in figure 6.5 is *averaged* over multiple, slightly varying equilibria.

An avenue of further study would be to better perturb the equilibrium without altering the nature of the equilibrium as much. A better method of perturbation might include changing only the edge pressure gradient and not the core pressure by manipulating the pedestal region only. The second method of manipulating the pressure profile was not attempted during this investigation due to the time-scales involved in the work and the lack of certainty that there would be a positive outcome.

To test whether changes in the pressure profile alone would be likely to lead to stability for this discharge, the pressure was scaled and the SCENE programme used to calculate a number of values of α and $j_{\|}/\langle j \rangle$. Figure 6.7 shows the resulting values which nearly lie in a straight line. This result is not surprising, if it is considered that the pressure gradient can drive plasma current by means of the bootstrap, diamagnetic and Pfirsch-Schlüter currents (Section 1.4).

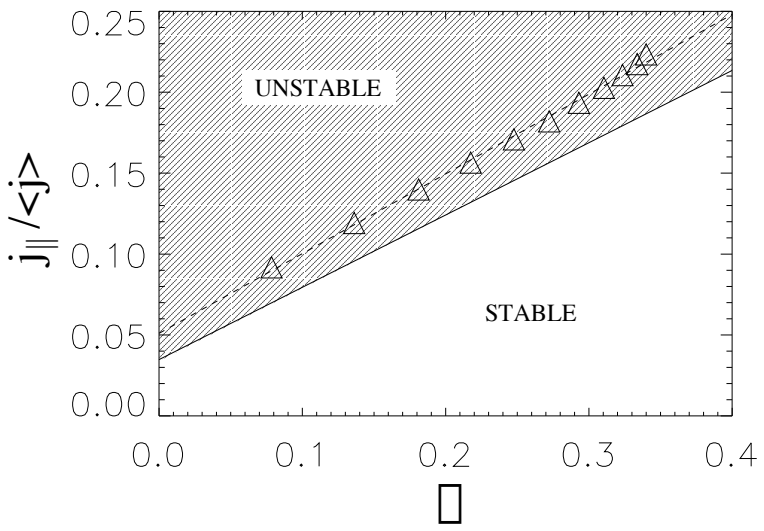

Figure 6.7: *Plot of predicted $j_{\|}/\langle j\rangle$ for a range of α ($\triangle$) fitted with a straight line (dashed). The regions of stability and instability are also shown.*

Although there were many difficulties and compromises made during this part of the investigation, the preliminary conclusion is that the equilibrium based on discharge number 29759 is slightly unstable to the peeling mode, irrespective of the actual value of α.

6.3.3 Possible trigger mechanisms for the ELMs

In section 2.6, two possible trigger mechanisms for type III ELMs were outlined. The first mechanism involves the suppression of the edge current density due to electron-electron collisions. SCENE has a model for the three internal sources of current that takes into account the changes in collisionality. Since changing the value of α did not result in crossing the stability boundary, this mechanism is unlikely to be the cause of a rise in $j_{\|}/\langle j\rangle$ prior to each ELM, for this particular discharge.

Further support for dismissal of the first mechanism comes from examining the edge collisionality of the discharge. Figure 6.8 shows the evolution of the edge collisionality of discharge number 29759 taken with HELIOS, using the same method as that used to produce figure 2.10. Normalised edge collisionality, ν_e^* varies between ≈ 1, immediately before each ELM and ≈ 2, immediately after. From figure 2.10, it can be seen that this data makes the discharge fairly typical for ELMing H-modes on COMPASS-D. Although high collisionality can causes a suppression of the destabilizing bootstrap current in favor of the partially stabilizing Pfirsch-Schlüter current

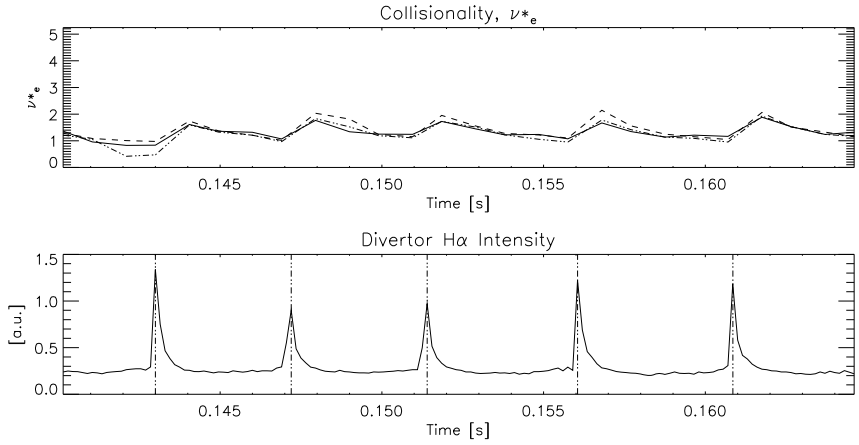

Figure 6.8: *Normalised electron collisionality shown with D_α emission at the 95% (dashed) and 90% (dotted) flux surfaces and for the radius of maximum electron pressure gradient (solid), for discharge number 29759 on COMPASS-D.*

as the percentage of trapped particles decreases (section 2.6), in this regime, current varies approximately as $1/\left(1 + a \times \sqrt{\nu^*}\right)$ where a is a constant of order 1. This means that a change in ν^* from 1 to 2 results in a decrease in bootstrap current of $\approx 20\%$. The suppression of the edge current due to increased collisionality is therefore a weak effect.

The second mechanism relies on the finite current penetration time. The normal trajectory discussed (Snyder et al., 2002) involves the pedestal pressure gradient rising to take the discharge into the stable region. Since the edge current cannot rise instantaneously, due to Lens' law, the discharge remains stable until the edge current rises towards the static equilibrium value, crossing the peeling boundary and destabilizing the discharge.

A preliminary attempt at modeling the second possible mechanism is described in the next section. The current is assumed to tend towards a target value, which is defined as the static equilibrium value shown in figure 6.7. The discharge is assumed to go unstable when it reaches the linear fit to the marginally stable points, averaging the effects of the *fuzzy* boundary.

6.3.4 Mapping the trajectory in $j_\parallel / \langle j \rangle$ - $\hat{\alpha}$ space

The trigger mechanism described in section 2.6 and summarised above could be modeled by assuming that the discharge evolves towards a target state but reaches the peeling boundary first, which results in the ELM event. Using the inter-ELM data

from HELIOS, a simple model was applied to the trajectory of the discharge between the ELM events.

In section 2.6, the resistive diffusion time was found to be,

$$\boxed{\tau_\eta = 4.5ms}.$$

The particle diffusion time, which might govern the rise in edge pressure is $\tau_p = 41ms$. The particle diffusion time is an order of magnitude longer than the resistive diffusion time. This might imply that the edge current density will follow the edge pressure gradient, driving the peeling mode and preventing access to H-mode. On the other hand, the pressure gradient might rise on a faster time-scale than the particle diffusion time if the change in edge pressure was the result of convection, rather than diffusion. This suggestion is supported by the data taken by HELIOS which shows the edge pressure gradient changing on a time-scale of the order of milliseconds.

If it can be considered that the pressure gradient is the primary source of current for the plasma edge, as suggested by the equilibrium reconstruction shown in figure 6.2, then it is clear that the current rise must lag behind the change in pressure gradient by the current rise time. The trajectory of the plasma in $j_\parallel / \langle j \rangle$ - $\hat{\alpha}$ space was modeled based on these assumptions.

The analytical approximation for normalised pressure gradient, $\hat{\alpha}$, for a large aspect ratio, circular cross-section plasma was calculated. The expression for $\hat{\alpha}$ that was given by Connor et al. (1978) and derived in section 2.4.3 was used. It is repeated here for ease of reference,

$$\hat{\alpha} = -\frac{2\mu_0 R q^2}{B^2}\frac{\mathrm{d}p}{\mathrm{d}r}. \tag{6.3}$$

All the parameters are available from HELIOS or the magnetic diagnostics. The result was fit with a spline and is shown in figure 6.9. Since $\hat{\alpha}$ is an analytical approximation to α (section 2.2), the two are related but are not exactly the same. The vertical lines represent the onset of the ELM events and each inter-ELM period is labelled with a letter; A, B, C, and D. The actual ELM event occurs too quickly to be observed by the diagnostic. Figure 5.7 shows that the rise in D_α occurs on a much faster time-scale than the resolution of HELIOS. Carolan et al (1994) measured the rise in D_α to take $\approx 20\mu s$. The decay in the signal is dependent on the rate of recycling, which is unrelated to the time-scale of the ELM event. This observation is supported by figures 5.12a and 5.12b. It is justified to ignore the actual ELM event, assuming that it was *smeared out*.

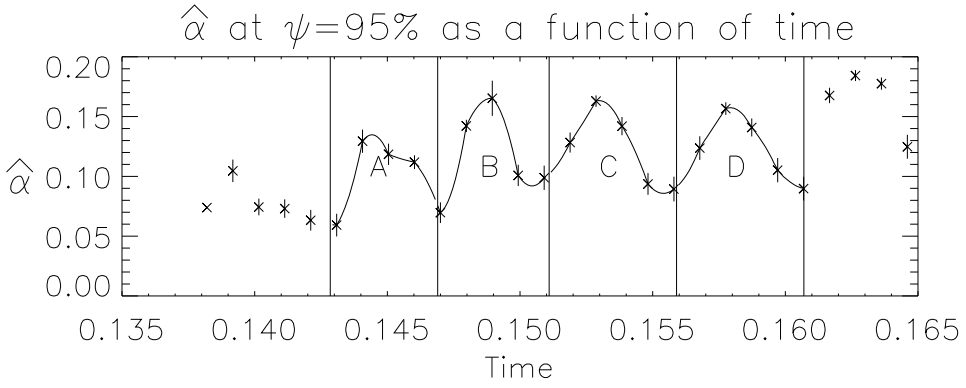

Figure 6.9: *Spline fit of normalised pressure gradient, $\hat{\alpha}$. The vertical lines represent ELMs. The four inter-ELM periods are labelled A, B, C, and D.*

The value of $j_{\|}/\langle j \rangle$ is more problematic. Local current densities were not measured on COMPASS-D or MAST.

Immediately following a change in the edge pressure gradient, there will be a change in the bootstrap current (section 1.4.1). Since current cannot change instantaneously because of finite resistivity, a back EMF is generated that will drive an equal and opposite current, (in accordance with Lenz's law,) that opposes the change in the current,

$$\boldsymbol{E}|_{t=0} = -\eta_{\|}\, \delta \boldsymbol{j}. \tag{6.4}$$

In the above, $\boldsymbol{E}|_{\boldsymbol{t=0}}$ is the electric field due to the back EMF immediately following the change in pressure gradient, $\eta_{\|}$ is the resistivity parallel to the current flow, and δj is the difference between the target current density (which is the current density after an infinite time or the current density were it not for Lenz's' law) and the actual current density. From Maxwell's equations,

$$\frac{\partial \boldsymbol{B}}{\partial t} = -\boldsymbol{\nabla} \times \boldsymbol{E}. \tag{6.5}$$

Taking the curl of both sides of the above equation gives,

$$\frac{\partial}{\partial t}(\boldsymbol{\nabla} \times \boldsymbol{B}) = -\boldsymbol{\nabla} \times (\boldsymbol{\nabla} \times \boldsymbol{E}), \tag{6.6}$$

$$\frac{\partial \boldsymbol{j}}{\partial t} = -\frac{1}{\mu_0}\nabla^2 \boldsymbol{E}. \tag{6.7}$$

The current which is generated by the back EMF must diffuse out of the edge region. The current density is assumed to tend towards the target on an exponentially

corrected resistive time-scale,

$$\nabla^2 \boldsymbol{E} = -\eta \frac{\delta j}{\mu_0 r l}\, e^{-t/\tau}, \tag{6.8}$$

where $\mu_0 r l/\eta = \tau_\eta$ (equation 2.27). Assuming that $\tau = \tau_\eta$ in the exponential gives,

$$\nabla^2 \boldsymbol{E} = \frac{\partial j}{\tau_\eta}\, e^{-t/\tau_\eta}. \tag{6.9}$$

In the above, l is a characteristic scale length which, in this case is the pedestal width. Integrating equation 6.8 gives,

$$j = -\delta j \left[\, e^{-t/\tau_\eta} + c \right]. \tag{6.10}$$

Imposing the limit that $j = j_0$, at $t = 0$ gives the final equation,

$$j = j_0 + \delta j \left[1 - e^{-t/\tau_\eta}\right], \tag{6.11}$$

where j_0 is the initial current.

This simple model was applied to discharge number 29759. Relationships between $j_\parallel / \langle j \rangle$ and $\hat{\alpha}$ for marginal stability and target currents were taken from straight line fits in figures 6.5 and 6.7 respectively. As mentioned above, α and $\hat{\alpha}$ are not generally the same and so the gradients of the marginal stability and target current lines were scaled accordingly. At time $t = 0.164$, values for $\alpha = 0.3019$ and $\hat{\alpha} = 0.1776$ were compared to give a correction factor of $c = 1.6999$.

At the point immediately before each ELM was initiated, the plasma was assumed to be at marginal stability. This is clearly an approximation compared to the actual stability calculation (figure 6.5), but is satisfactory for the purposes of examining the discharge evolution in $j_\parallel / \langle j \rangle - \hat{\alpha}$ space. The normalised edge current density was extrapolated backwards and plotted against the normalised pressure gradient to trace the trajectory of the discharge in $j_\parallel / \langle j \rangle$ - $\hat{\alpha}$ space.

The model was applied to each of the four inter-ELM periods using a range of time-scales. The results for a number of time-scales between $\tau = 4.0 - 5.5ms$, are shown in figure 6.10.

For time-scales, $\tau_{\text{EXP}} \leq 4.0ms$, the model predicts that the current falls to zero as the model tracks backwards. This result is clearly unphysical, the interpretation of this result is that the edge current density is changing too fast, therefore τ_{ELM} would be shorter than observed for the discharge in question.

It is difficult to put an upper limit on τ_{EXP} based on the model and temporal resolution of the data as it stands. Since an ELM is an instability, it might logically be assumed that some pressure is lost from the edge of the plasma during each

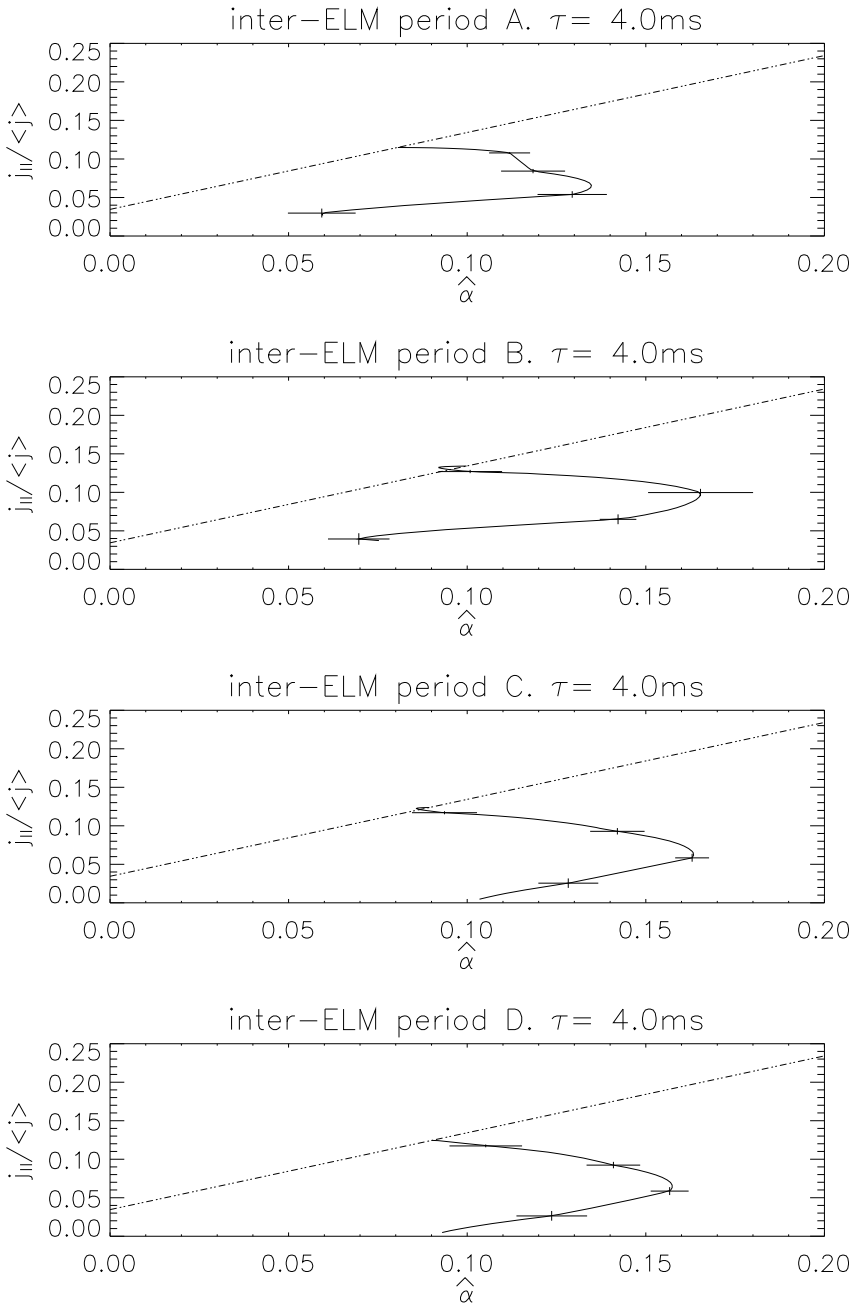

(a) *The trajectory for* $\tau = 4.0ms$

Figure 6.10: *The predicted trajectories in* $j_{\|}/\langle j\rangle$ *-* $\hat{\alpha}$ *space for* $\tau = 4 - 5.5ms$*. The dotted line represents the line of marginal stability.*

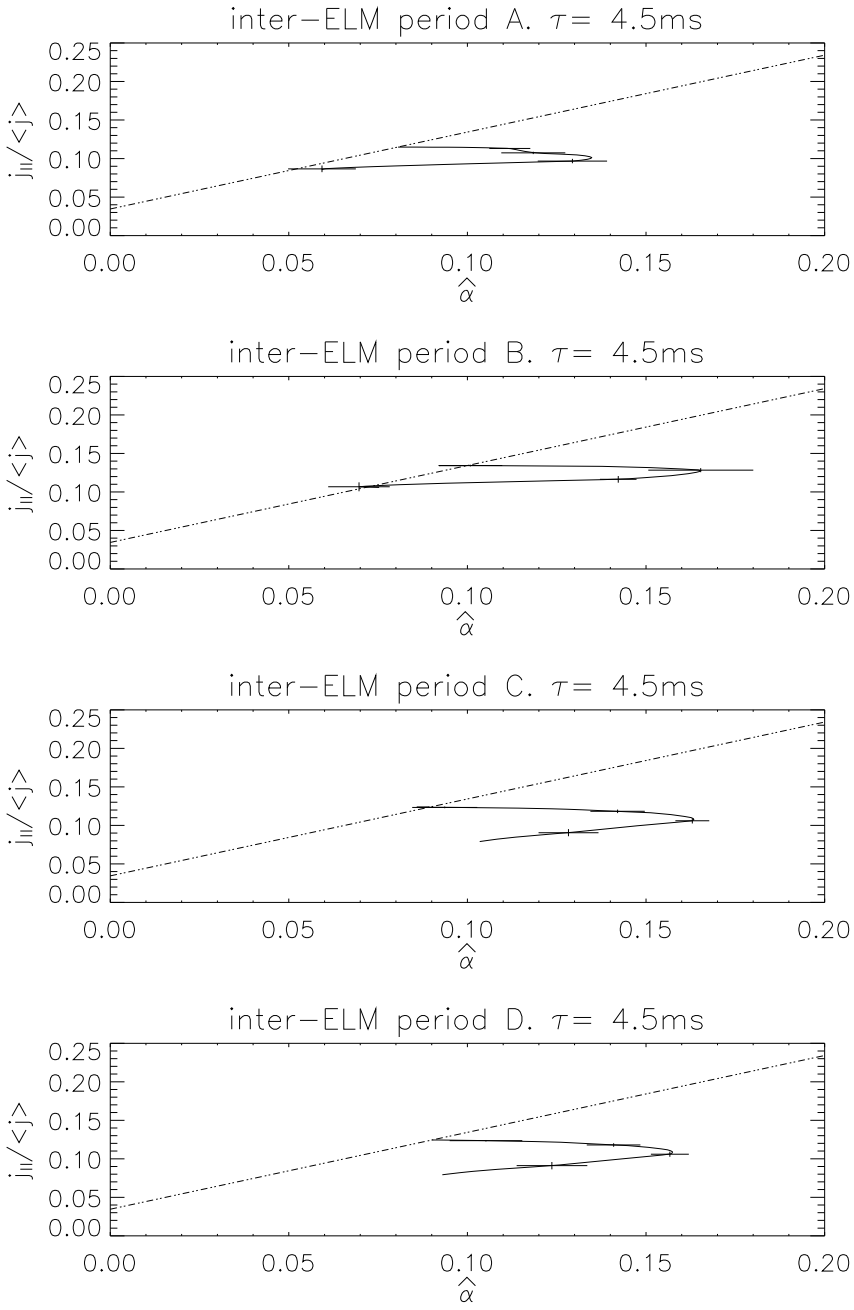

(b) *The trajectory for* $\tau = 4.5ms$

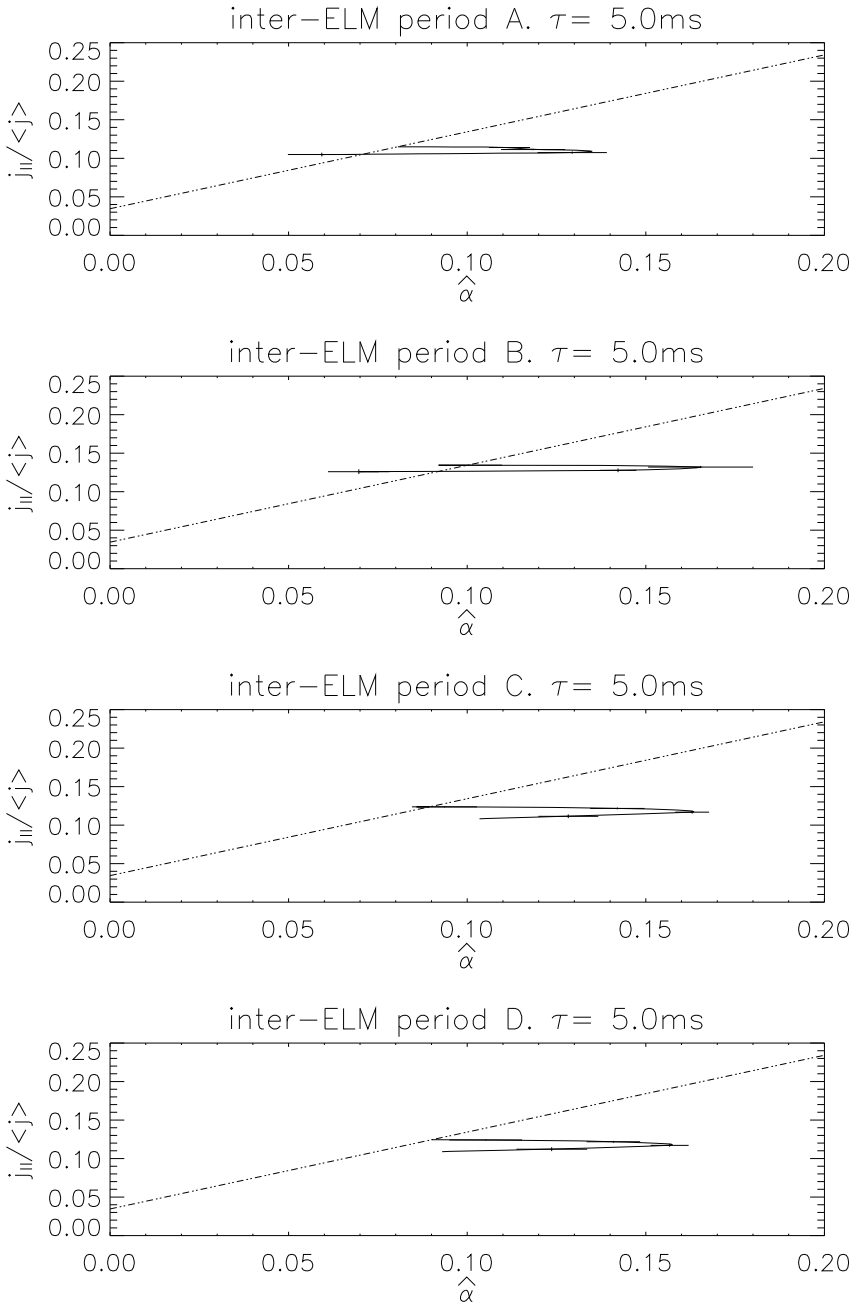

(c) *The trajectory for* $\tau = 5ms$

Figure 6.10: *The predicted trajectories in* $j_{\|}/\langle j\rangle$ *-* $\hat{\alpha}$ *space for* $\tau = 4 - 5.5ms$*. The dotted line represents the line of marginal stability. (cont.)*

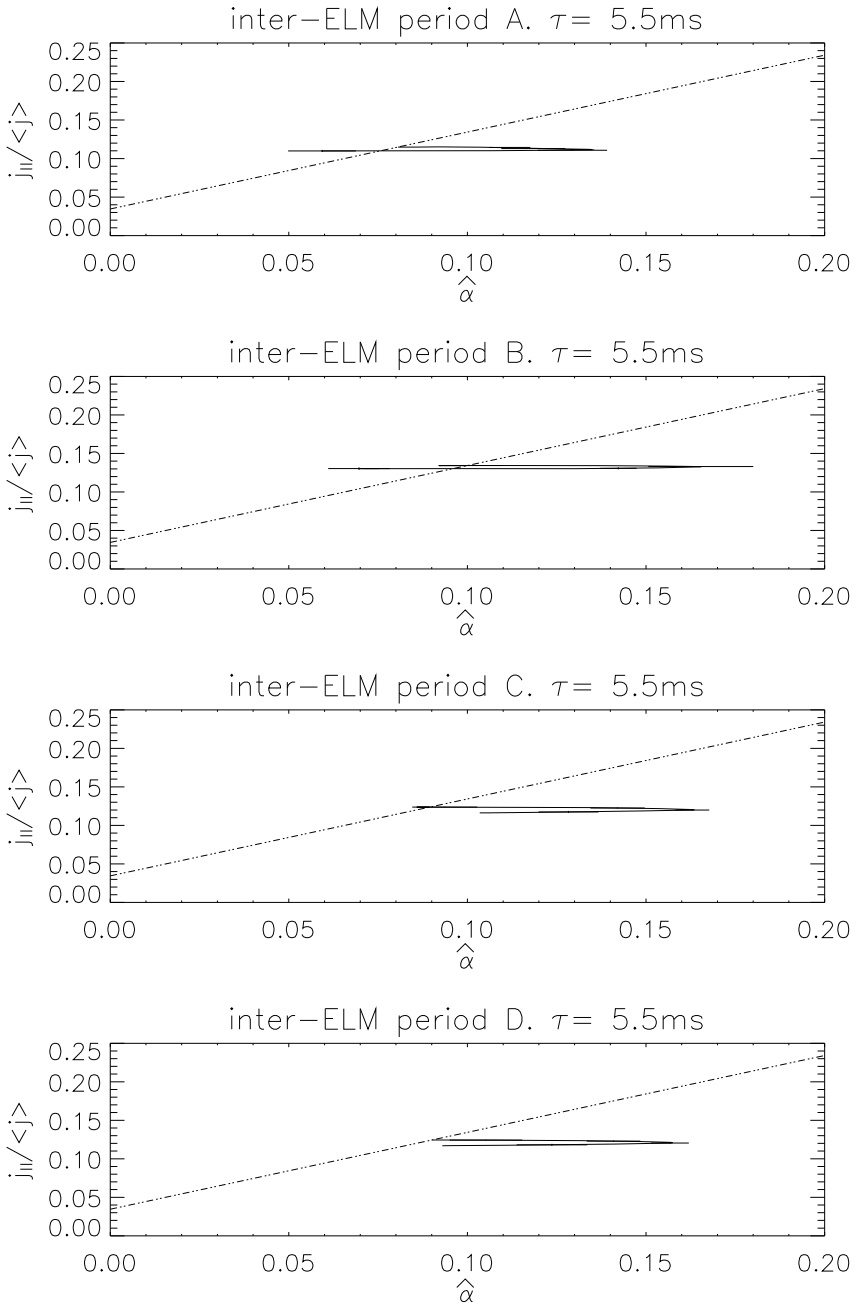

(d) *The trajectory for* $\tau = 5.5ms$

event. For the discharge to become stable again to the peeling mode, an equivalent or greater amount of normalised edge current density must be lost in order to stabilise the discharge. Since the data from HELIOS is of insufficient temporal resolution to measure how much the pressure gradient is degraded during the ELM event, an exact calculation of the magnitude of the edge current density loss is impossible.

It can be assumed that some edge pressure must be lost. By inspection of figure 6.10d, it can be seen that only a very small amount of the normalised edge current density is lost ($< 5\%$) for $\tau = 5.5ms$. It is difficult to see how such a small loss of edge current density could stabilise a significant loss of edge pressure as is likely to occur during an ELM event. It seems reasonable to suggest that the appropriate current diffusion time is approximately,

$$\boxed{\tau_{\text{exp}} \approx 4.5 - 5ms}.$$

The modeled current rise time ($4.5 - 5ms$) and resistive diffusion time ($4.5ms$) are in excellent agreement.

6.4 Conclusions

Results from the previous section showed that the electron pressure gradient could fall prior to the onset of type III ELMs on COMPASS-D.

The phenomenon can be interpreted in terms of the model described in section 2.6. The original work makes no prediction as to the inter-ELM trajectory in $j_{\|}/\langle j \rangle$ - α space. The assumption made by Snyder et al. (2002) is that the pressure gradient rises and the edge current density follows, as shown in figure 2.11 and repeated here as figure 6.11a.

It is possible for the plasma to approach the stability boundary from a drop in α as well as a rise in $j_{\|}/\langle j \rangle$. A simple model for the trajectory of the plasma in $j_{\|}/\langle j \rangle$ - $\hat{\alpha}$ space was suggested and a preliminary stability analysis conducted, including an attempt to map out the trajectory of discharge number 29759 during inter-ELM periods.

The stability study showed that the initial equilibrium was unstable. A linear fit to the marginal stability points gave the line of marginal stability. It was also shown that varying the pressure gradient could not lead to stabilisation of the equilibrium.

Two possible trigger mechanisms were considered for the ELMs in discharge number 29759. The first mechanism involves suppression of the edge current via electron collisionality. Since the equilibrium solver SCENE incorporates a model

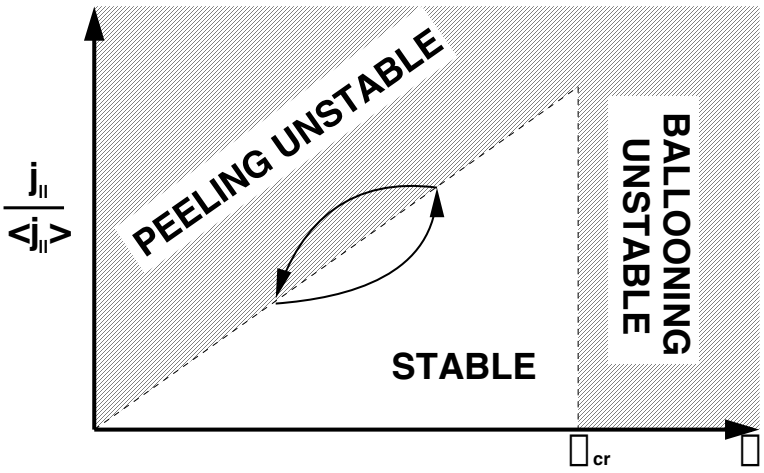

(a) *The original predicted trajectory.*

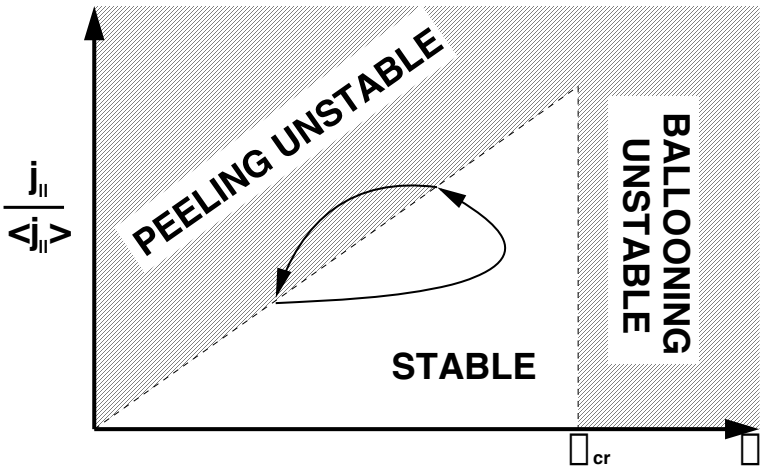

(b) *The second possible trajectory.*

Figure 6.11: *Schematic of the stability boundaries showing the two possible inter-ELM loci for type III ELM events*

for edge current that considers edge collisionality, this mechanism was dismissed as unlikely. Further evidence came from the HELIOS diagnostic that showed the normalised edge collisionality to only change by a factor of two, which would result in only a small change in edge current.

The second mechanism considered, relies on there being a finite current rise time in the plasma. An increase in edge pressure can result in temporary stability to the peeling mode if the current rises on a slow enough time-scale following the change in pressure. A simple model based on this premise was applied to the discharge, yielding good results. Comparison with the modeled current rise time and calculated resistive diffusion time showed excellent agreement. The inter-ELM trajectory of discharge number 29759 would look like the one shown in figure 2.11.

6.5 Further Work

Both the GS2D and SCENE codes make use of an (R, Z) coordinate system, on which they solve the Grad-Shafranov equation. For this work, it proved impossible to use a high enough resolution when using GS2D and computationally expensive when using SCENE to resolve the rational surfaces in the edge pedestal. Further work might involve the implementation of the CHEASE numerical equilibrium code (Lütjens et al., 1992) which solves the Grad-Shafranov equation in flux coordinates thereby automatically compensating for the concentration of flux surfaces in the edge region due to the steep pressure gradient in the pedestal.

More work should be directed to the shape of the marginal stability curve shown in figure 6.5. Due to the way in which the pressure gradient was scanned, the equilibrium became distorted and failed to converge when attempts were made to find marginally stable points with high α. Increasing the edge gradient without increasing the pressure in the core of the plasma is one possible method to avoid this problem.

Chapter 7

Summary and conclusions

There were two main aims of this work. The first aim was to upgrade the HELIOS diagnostic; improving its stand-alone capabilities as well as combining it in synergy with CELESTE. The second aim was to use the upgraded diagnostic to contribute to the developing areas of H-mode transition and ELM theory.

7.1 The HELIOS-CELESTE hybrid diagnostic

7.1.1 The HELIOS diagnostic

The HELIOS diagnostic is a multi-chord, multi-time, active helium line intensity ratio spectrometer. HELIOS provides measurements of electron density, (n_e) and electron temperature (T_e), at ten positions, radially spaced over $\approx 5\ cm$ around the separatrix. Originally, helium gas was injected into the plasma at the outboard mid-plane via a $4\ mm$ open pipe. This method, although partially successful resulted in a large flux of helium into the plasma, limiting the amount of time over which the diagnostic could take data. To resolve this problem, an array of three micro-nozzles of radius $20\ \mu m$ was installed. The new method of injecting helium involved flooding the nozzle manifold with helium and allowing the helium to be pushed out under the back pressure. After the discharge, the manifold was pumped down to vacuum again.

The collection optics were placed directly above the region where the neutral helium jet interacted with the plasma, focused light onto an array of 10 optical fibers which conveyed the light to the spectrometer. The spectrometer was a $0.6\ m$ Czerny-Turner with a $1200\ lmm^{-1}$ grating. The spectra were measured using a CCD camera and recorded using a PC. During the course of the work, the temporal resolution was increased by the installation of a liquid crystal shutter which was controlled by the same signal pulses that controlled the CCD camera. This development allowed us to

reduce cross-talk between chords in consecutive time-slices as the data was clocked into the storage region of the CCD chip.

7.1.2 The CELESTE diagnostic

The CELESTE diagnostic is a high-resolution, multi-chord, multi-time Doppler spectrometer. In the configuration that was used for this work, the diagnostic was used to measure the Doppler shift and Doppler broadening of the $HeII$ spectral line at $468\ nm$, to extract temperature and velocity information.

CELESTE made use of the same collection optics as HELIOS. At the tokamak end, 19 pairs of optical fibres were arranged in a 2×10 array, adjacent to and with the same extent as the HELIOS optical fibres. The two spectrometers were therefore, inherently aligned. At the spectrometer end, a wavelength calibration chord was added and the 20 pairs were arranged in a 4×5 staggered grid which minimised cross-talk between chords. The spectrometer was a $1\ m$ Czerny-Turner with a $2400\ lmm^{-1}$ grating. In common with HELIOS, a CCD camera, attached to a PC was used to record the spectra.

7.1.3 Diagnostic synergy

The combination of the two diagnostics, using the same collection optics allowed for a wide range of plasma parameters to be measured. In addition to the T_e and n_e profiles from HELIOS and V_{HeII} and T_{HeII} from CELESTE, combining the two diagnostics enabled the indirect measurements of a number of different parameters, including the radial electric field.

7.1.4 Validation of the HELIOS data

A self-consistency check was performed on HELIOS, which involved comparing the emission profile of one of the helium lines ($667\ nm$), as measured by the HELIOS spectrometer to a calculated profile, using a simple coronal model and the analysed data from HELIOS. The profiles agreed fairly well. There was a discrepancy between the calculated and measured level of light on the outer side of the profile. This discrepancy might be explained as a result of the assumptions used in the coronal model.

A statistical comparison was performed, over many discharges, between the HELIOS and Thomson scattering diagnostics. Good correlations were found of 0.82 for T_e and 0.83 for n_e. A systematic under-estimation of n_e by HELIOS, by a factor

≈ 3.6 was found, compared to Thomson scattering. Upon investigation, it was found that the cause of the systematic error was a degradation in the FLC-shutter that was installed to increase the temporal resolution of HELIOS.

Experiments conducted immediately after the installation of the shutter were assumed to be reliable as the damage most probably would have occurred slowly over time. For the purposes of calculating the electric field, the n_e and T_e scale lengths are required, these values are insensitive to the absolute values and so HELIOS data could still be used in synergy with CELESTE to measure the radial electric field.

7.2 ELM dynamics

Much work has been carried out in the field of ELM dynamics. In this thesis, one of the leading models of ELM stability theory was reviewed (section 2.6). The model includes the peeling and ballooning modes as possible sources of instability. The peeling mode is highly localised, current driven instability that is resonant on the closest rational surface to the edge of the plasma. It is destabilised by edge current but stabilised by the pressure gradient. The edge ballooning mode is slightly more radially extended than the peeling mode but is still localised at the edge. It is a purely pressure gradient driven mode. The combination of the two instabilities leads to a triangle of stability in α (normalised edge pressure) - $j_{\|}/\langle j \rangle$ (normalised edge current density) space. Large type I ELMs are thought to be a result of coupled peeling-ballooning modes whilst small type III ELMs are thought to be pure peeling modes.

7.2.1 Experimental ELM studies

Data from HELIOS on COMPASS-D showed that for discharge number 29759 which had slow, type III ELMs, the edge pressure fell prior to the onset of each ELM. The measurements were validated with data from the edge Thomson scattering diagnostic on COMPASS-D. Data from the linear D_α camera on MAST showed that the edge electron density gradient could sometimes fall prior to type III ELMs but sometimes did not. The conclusion of this part of the investigation was that a fall in edge pressure is possible prior to type III ELMs but is not an inherent feature.

7.2.2 Preliminary stability analysis

An equilibrium reconstruction of discharge number 29759 was performed using the SCENE numerical code. The equilibrium was used for a stability analysis using the

ELITE code. The discharge was found to be unstable to the peeling mode, in keeping with the model presented. A stability study, conducted by varying the values of α and $j_{\|}/\langle j \rangle$, showed that the discharge was such that varying the edge pressure affects the static equilibrium edge current in such a way that equilibrium cannot be made stable.

Two trigger mechanisms for the ELMs were proposed. The first mechanism is that high collisionality suppresses the pressure driven currents at the edge of the plasma. If the collisionality then falls, the current will rise and an ELM will result. This mechanism was dismissed as unlikely as the equilibrium solver used during the stability analysis took account of collisionality. Further evidence came from the calculation of edge collisionality for the discharge in question, which showed ν_e^* to vary by a factor of two which would result in a relatively small change in the edge bootstrap current.

The second possible mechanism relied on a finite current rise time giving temporary access to the stable region before the internally, pressure driven currents rise to cause the peeling mode to become unstable. An attempt to plot the trajectory in $j_{\|}/\langle j \rangle$ - $\hat{\alpha}$ space for COMPASS-D, discharge number 29759 was made. Straight lines were fit to the marginally stable and static equilibrium values. The static equilibrium values were taken as target currents that the discharge would evolve towards for any given value of $\hat{\alpha}$. The normalised edge pressure, $\hat{\alpha}$, was directly calculated from HELIOS measurements and the normalised edge current density, $j_{\|}/\langle j \rangle$, was predicted using a simple model. The model was used to predict a characteristic rise time which agreed extremely well with the neo-classical resistive diffusion time, which was $\tau_\eta = 4.5ms$.

7.3 Further work

Both equilibrium solvers that were used in the preliminary stability analysis solve the Grad-Shafranov equation on an R-Z grid. This method makes it computationally expensive to solve a sufficiently resolved equilibrium for the stability analysis. One way to address this problem would be to implement an alternative equilibrium solver such as the CHEASE code, which solves the Grad-Shafranov equation in flux coordinates. Solving the equilibrium in flux coordinates will automatically compensate for the clustering of flux surfaces near the plasma edge due to the steep edge pressure gradient. This will allow a full stability analysis of any discharge on either COMPASS-D or MAST using the ELITE stability code.

The MAST tokamak has recently had a 300-point Thomson scattering diagnos-

tic installed. This diagnostic is capable of producing n_e and T_e profiles across the entire radius of the plasma. A proposed future experiment on MAST will involve reconstruction of the entire profiles with many time-points relative to ELM events.

Due to the small database of data available for this investigation, it was not possible to see how the physics changed under varying conditions. It would be of interest to discover what caused the drop in pressure gradient observed before the ELMs. Preliminary studies using the Mirnov magnetic pick-up coils have yielded no clues. One suggestion is that a resistive ballooning mode is responsible. This mode may not show up on the magnetic diagnostics as it can be electrostatic in nature. A possible first step in an investigation into the cause of the drop in edge pressure gradient would be to vary plasma parameters, such as density and plasma current, to identify the conditions under which the phenomenon occurs.

Appendix A

The first attempt at generating the equilibria (GS2D)

The full equilibrium reconstruction for each time-slice was performed in four stages.

1. An equilibrium reconstruction was performed using the EFIT code (section 1.3.2).

2. Data for the edge pressure from HELIOS and a core value from TS was substituted for the EFIT generated pressure profile and the equilibrium reconstruction was performed again with EFIT fitting the pressure profile with a polynomial.

3. The complete pressure profile was fit using the sum of a modified tanh fit and a polynomial. The *mtanh* function was kindly supplied by Groebner and Osbourne (1998) of DIII-D.

4. The fit pressure profile was substituted for the pressure output from EFIT and a separate equilibrium solver, GS2D (Roach and Thyagaraja, 2002), was used to re-generate a consistent solution.

A.1 Initial EFIT reconstruction

This initial stage was performed with the assistance of Hendrik Meyer. Accurate reconstructions for all time-slices were generated with the inclusion of extra outboard Mirnov coils, which are not normally used, and with great care paid to the relative weighting of the magnetic coils until the best fit was obtained.

The modified calibration file was then used to create separate equilibrium files for each time-slice, which were needed for the next stage of the analysis. EFIT, in

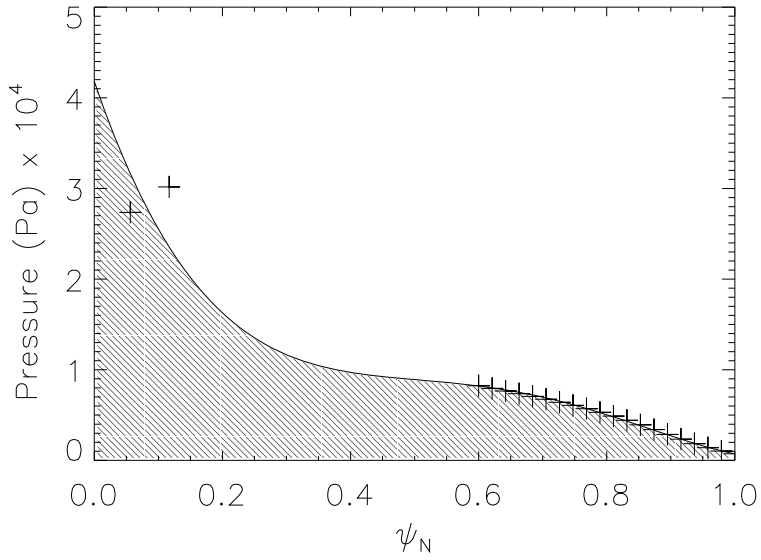

Figure A.1: *A polynomial pressure fit from EFIT for discharge number 29759 ($t = 0.148ms$). The polynomial fit gives an approximation to the general shape of the pressure profile but lacks the flexibility to make small changes at the edge without affecting the core.*

common with all the equilibrium solver codes used in this analysis requires the total pressure profile rather than the electron pressure. The total temperature profile was calculated using the Artsimovich scaling law (Artsimovich, 1972a). The total density profile was estimated by assuming quasi-neutrality, with the mean atomic number taken to be, $Z_{eff} = 2$.

A.2 Gross change in P_e performed by EFIT

Real pressure values for HELIOS and TS at the edge were fitted in flux space, using the equilibrium fit generated in the previous step. The fit was combined with TS values from the core and substituted into equilibrium files for five time points between a single ELM, these time points were; $0.147ms, 0.148ms, 0.149ms, 0.150ms$, $0.151ms$.

EFIT fits pressure profiles with a polynomial fit. An example of which can be seen in figure A.1. The profile appears as if it might be unphysical because there is no constraint on $(\mathrm{d}P/\mathrm{d}\psi)_{\psi=0}$. Under these circumstances, the pressure profile is not necessarily flat at magnetic axis, *i.e.* $(\mathrm{d}P/\mathrm{d}r)_{\psi=0} \neq 0$. In fact, EFIT *rounds off* the pressure profile at the centre, after the fitting.

Although this method is perfectly valid and creates consistent equilibria, due to the nature of a polynomial fit, any small change at the edge of the plasma pressure profile will create a larger change towards the centre of the equilibrium.

A.3 Fitting the pressure profile

The measured pressure profile for discharge number 29759 at time $t = 0.148$, including the entire TS profile except for the outer-most TS point can be seen in figure A.3. The outer-most TS point was ignored because it is on the same flux surface as the inner-most usable HELIOS data point. From figure 5.3(a,b), it can be seen that the agreement between the two diagnostics was good but the TS does not have the time resolution to track the changes in edge pressure. The profile was fit with a modified tanh (mtanh) function supplied by R.J. Groebner of DIII-D,

$$Y = A_1 \times \tanh\left\{\frac{2(A_5 - r)}{A_3}\right\} + A_2, \tag{A.1}$$

$$Y = Y + A_6 \times (A_4 - r) \quad \} \; r < A_4. \tag{A.2}$$

In the above,

$$\begin{aligned} A_1 &= \text{Offset}, \\ A_2 &= \text{Height of pedestal}, \\ A_3 &= \text{Width of pedestal}, \\ A_4 &= \text{Position of knee}, \\ A_5 &= \text{Position of pedestal}, \\ A_6 &= \text{Slope of line inside the knee}. \end{aligned}$$

An example of an mtanh curve, with the fitting parameters marked, is shown in figure A.2. Studies by Groebner and Osbourne (1998) show empirically that the mtanh function provides good agreement with measured temperature, density, and pressure profiles in H-mode. Work by Wagner and Lackner (1986) suggests that the tanh function may be the natural shape for the H-mode edge density pedestal.

The mtanh function was subtracted from the data and the difference was fit with a polynomial. This technique allowed small variations in the edge pressure gradient to be fit whilst not affecting the core pressure profile. An example of a fit can be seen in figure A.3. It might seem that the HELIOS edge data has little effect on the overall pressure profile but this is not the case. The HELIOS data effectively defines the gradient of the steep part of the mtanh function. The knee of which is limited by the TS data.

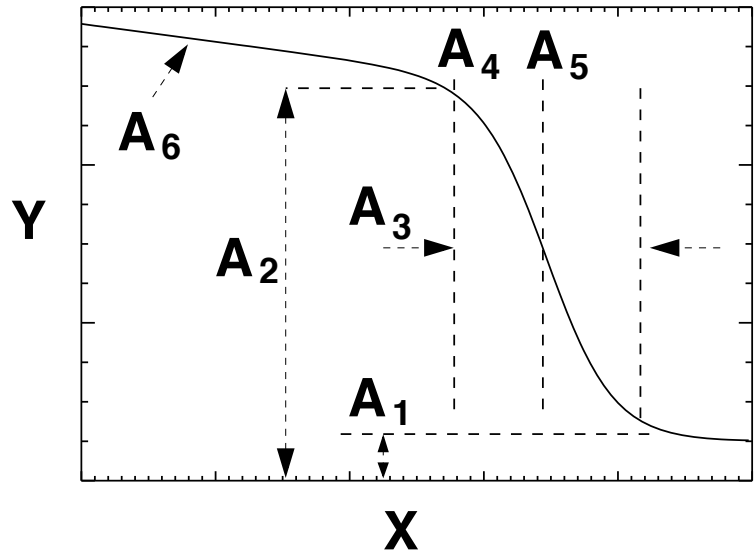

Figure A.2: *A representation of the modified* tanh *fit used for fitting the edge pressure to refine the equilibrium reconstruction for discharge* 29759.

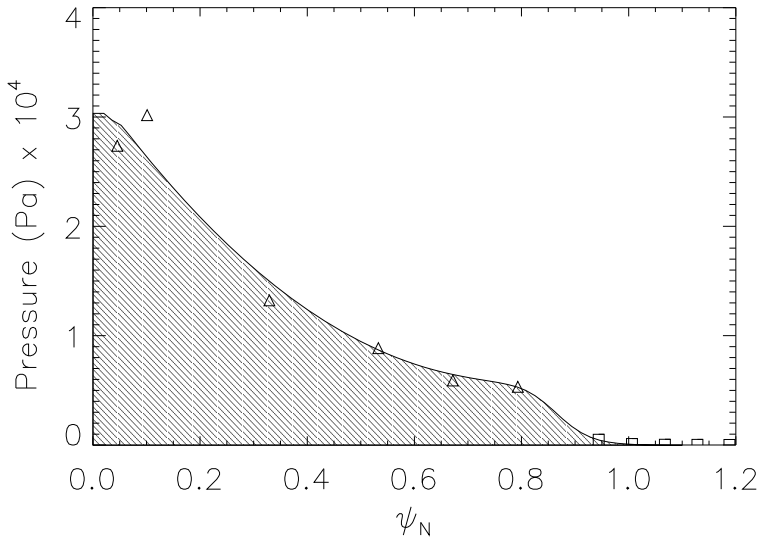

Figure A.3: *A modified tanh and polynomial fit to the pressure profile for discharge 29759* $t = 0.148ms$ *including TS (*$\triangle$*) and HELIOS (*$\square$*). This fitting method allows fine tuning of the edge pressure profile without affecting the core pressure profile.*

A.4 Final equilibrium using GS2D

GS2D is a numerical equilibrium solver that iteratively solves the Grad-Shafranov Equation (equation 1.14), for given pressure and f profiles, plasma current, and values of ψ at points on a rectangle surrounding the poloidal cross section (Roach and Thyagaraja, 2002).

It was impossible to make large changes to the pressure profile without seriously affecting the shape and size of the plasma boundary to the point where the solution became unphysical. GS2D was used here to combine the approximate equilibrium from EFIT with the correctly fitted pressure profile, thereby allowing meaningful comparisons of α and $j_{\|}/\langle j \rangle$, between time-slices.

An example of the output from GS2D can be seen in figures A.4a and A.4b. The shape of the poloidal flux surfaces are shown in the top left hand plot in figure A.4a. The equilibrium had a reasonable and physical shape. The level of error of the fit was low as shown in the top right hand and the bottom left hand graphs in figure A.4a. The pressure profile contained the pedestal, as measured by HELIOS and Thomson scattering and fit with the mtanh and polynomial fit. Figure A.4b shows the current profile as both a surface plot and a cross section at the $Z = 0$ plane. The dotted line shows the ff' contribution to the current, and the dashed line shows the p' contribution which had a clear peak due to the steep edge pressure profile. The resulting current profile is shown by the solid line, it can be seen that the high pressure shear led to enhanced edge current density. There was a shell of increased current just inside the separatrix. The final two plots show the p' and ff' contributions to the Grad-Shafranov equation. These equilibria were in qualitative agreement with equilibria generated by Horton et al. (2002) for similar work based on type I ELMy discharges on the ASDEX-U tokamak.

Attempts were made to use these equilibria to establish stability as tested by the elite code (section 2.4.5). After several unsuccessful attempts to test stability, it was observed that edge current given by GS2D was wildly variable, dependent on tiny alterations of the input pressure profile, inconsistent and often giving negative results. It became clear at this point that the alterations to the pressure profile from EFIT before entering them into GS2D constituted more than a small perturbative change. It was also noted that the ff' profile from EFIT was not well specified. To properly specify an ff' profile for GS2D, a bootstrap model would have to be used to predict the current profile. The equilibrium could then be iteratively solved until a consistent solution could be found.

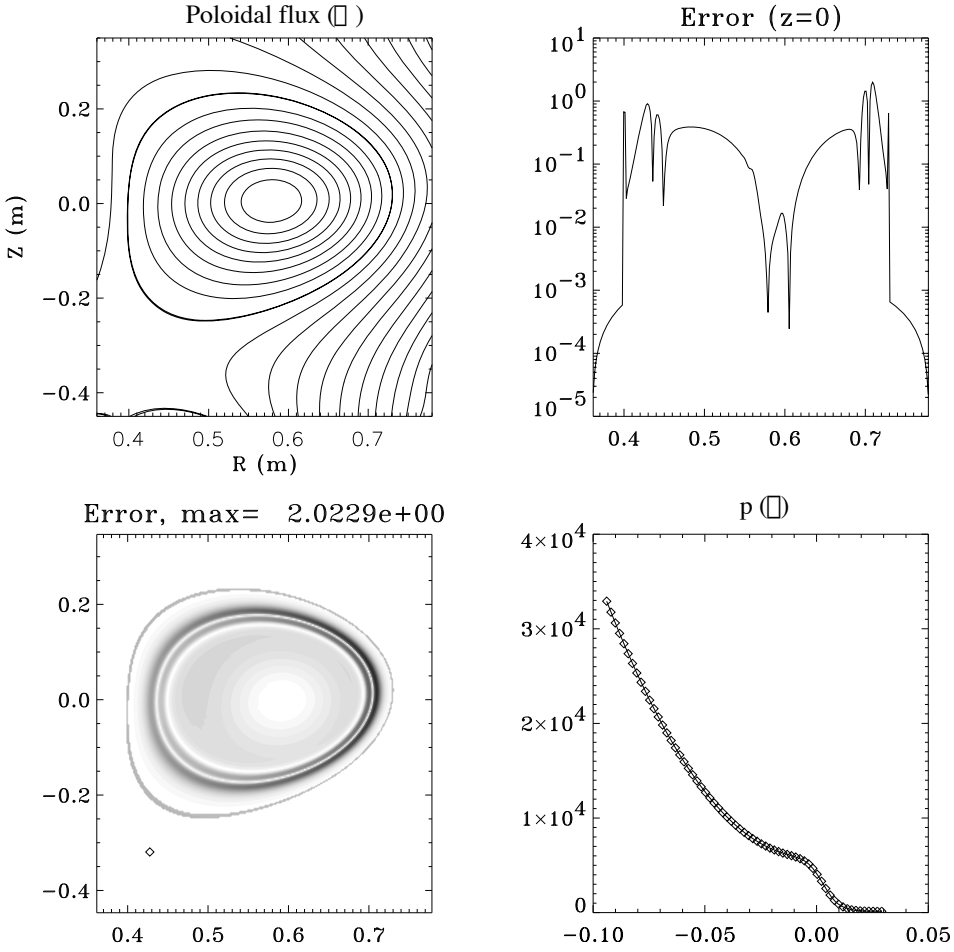

(a) ψ_N *(top left) and the level of error in the fit (top right, bottom left). In the shaded contour plot, the darkest regions have the highest error. The pressure profile measured by HELIOS and Thomson scattering and fit with a modified tanh and polynomial function is also shown (bottom right).*

Figure A.4: *An example of an output from GS2D*

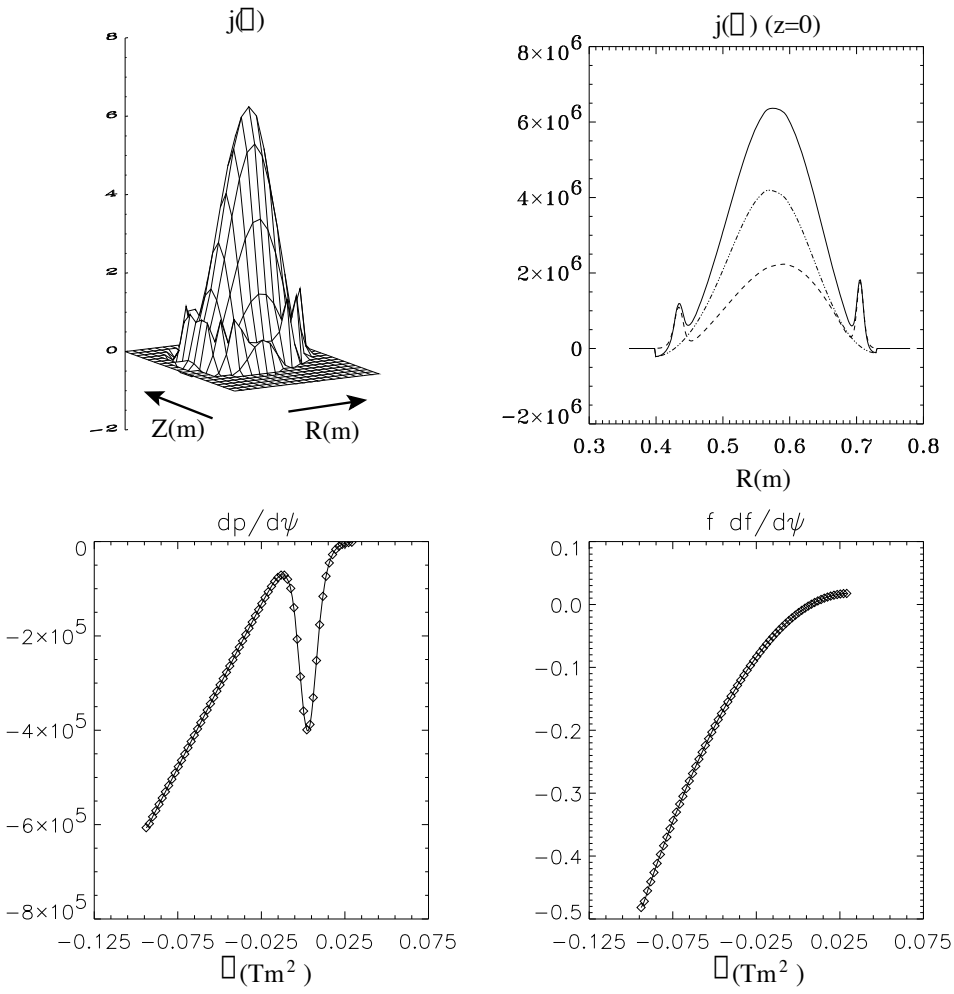

(b) *The plasma current density (top) and the contributions to the Grad-Shafranov equation* cf. *equation 1.14 (bottom). There is a local peak of increased current just inside the separatrix due to the steep pressure gradient.*

Making changes to a GS2D equilibrium is not a straight forward process. GS2D is a free boundary code, which means that it calculates the shape and size of the separatrix. Although this feature of the code can be of great use for certain studies, it adds complexity to this particular problem. When ff' or p' are altered, the shape of the discharge can be altered, in moderate cases, this means that the plasma changes shape but in more extreme cases, the equilibrium can fail to converge as the plasma size disappears to zero or increases greatly.

Furthermore, it was found that the achievable resolution of the GS2D equilibrium was insufficient for ELITE to converge fully. This was due to the steep edge pressure gradient associated with H-mode; pressure is a flux function and so a steep edge gradient will result in a concentration of flux surfaces at the edge. Many of the flux surfaces represent rational surfaces of q, which must be resolved for successful stability analysis.

Appendix B

List of Symbols

Common subscripts

$X_{\parallel}$	parallel to the magnetic field
$X_{\perp}$	perpendicular to the magnetic field
X_{θ}	in the poloidal direction
X_{ϕ}	in the toroidal direction
X_0	unperturbed or initial value
X_m	value at the neck of a magnetic mirror
X_e	electron
X_i	ion
X_D	deuterium neutrals
X_z	impurity ions
X_{edge}	value at edge of plasma
X_{ped}	value at top of pedestal
X_c	value at plasma core

Fundamental Constants

e	the charge on an electron ($1.6 \times 10^{-19} coulomb$)
ϵ_0	permittivity of free space ($8.854 \times 10^{-12} Fm^{-1}$)
μ_0	permeability of free space ($1.3566 \times 10^{-6}\ m\ kg\ C^{-2}$)
c	speed of light ($2.9979 \times 10^{8} ms^{-1}$)
k_b	Boltzmann constant ($1.3805 \times 10^{-23} JK^{-1}$)

Geometry

R	major radius
r	minor radius
S	surface area
ϕ	toroidal angle
θ	poloidal angle

ε	inverse aspect ratio (r/R)
κ	elongation
δ	triangularity
$\hat{\boldsymbol{e}}_{\boldsymbol{R}}$	unit vector in the direction of R
$\boldsymbol{e}^{\boldsymbol{\psi}}$	unit vector orthogonal to ψ
l	scale length

Magnetic field

$\boldsymbol{B}$	magnetic field
q	the safety factor
ψ	poloidal magnetic flux
ψ_a	poloidal magnetic flux on the magnetic axis
ψ_b	poloidal magnetic flux at the boundary
ψ_N	normalised poloidal magnetic flux

Plasma Parameters

n	density
T	temperature
p	pressure
α	normalised edge pressure
$\hat{\alpha}$	analytical approximation to α
ν_e	electron collision frequency (collisionality)
ν_e^*	normalised electron collisionality (to the bounce time)
η	resistivity
τ_E	energy confinement time
τ_η	resistive diffusion time
τ_p	particle diffusion time
s	magnetic shear
η_l	Lawson's coefficient for energy recycling
f	current flux function
$\boldsymbol{E}$	electric field
I_p	plasma current
$\boldsymbol{j}$	current density
j_b	bootstrap current
j_{PS}	Pfirsh-Schlütter current
P	power into the plasma
β	ratio of kinetic to magnetic pressure
$\ln \Lambda$	Coulomb logarithm
$\bar{\boldsymbol{\pi}}$	viscosity tensor
$\boldsymbol{R}_{\boldsymbol{z0}}$	friction force due to neutrals
$\boldsymbol{R}_{\boldsymbol{z\beta}}$	friction force due to species β

$\boldsymbol{v_{z\theta}}$	impurity velocity in z direction from poloidal rotation
$\boldsymbol{v_{zth}}$	impurity velocity in z direction from thermal motion
Z_{eff}	average atomic number of the ions in a discharge
λ_x	pedestal width of parameter x

Particles

m	mass
Z	atomic mass
$\boldsymbol{v}$	particle velocity
v_{eT}	electron thermal velocity
μ	the first adiabatic invariant
θ_g	the angle between an electron guiding centre and the $\boldsymbol{B}$-field
$\boldsymbol{F}$	force
$\boldsymbol{V_F}$	drift velocity due to a force
σ	collisional cross-section for bulk ions
σ_{ij}	collisional cross between for transition from state i to state j
E_f	Energy released for each fusion reaction
b	bremsstrahlung coefficient
ω_b	trapped electron bounce frequency
ρ_e	electron Larmor radius

Spectroscopy

C_{jk}	population rate from state j to state k
n_{He}	density of helium
A_{kj}	spontaneous relaxation rate from state k to state j
n_e^*	critical electron density for collisional radiative model
I_{jk}	light intensity from spectral line associated with $j-k$ transition
n_j	density of atoms in state j
A_j	spontaneous relaxation rate from state j to ground
A_{jm}	spontaneous relaxation rate from state j to all other levels
$\sigma_{j,rec}$	cross-section for recombination to state j
$\sigma_{j,ion}$	cross-section for ionisation from state j
λ_1	wavelength of transition line $3s^1S-2p^1P$ $(728.1nm)$
λ_2	wavelength of transition line $3d^1D-2p^1P$ $(667.8nm)$
λ_3	wavelength of transition line $3s^3S-2p^3P$ $(667.8nm)$
I_1	intensity of line λ_1
I_2	intensity of line λ_2
I_3	intensity of line λ_3
R_1	ratio of line intensities I_3/I_1
R_2	ratio of line intensities I_1/I_2
I	light intensity
L	length

ϵ	emissivity
Δ_α	width of D_α emission shell
$\langle\sigma v\rangle_{ion}$	ionisation impact parameter
$\langle\sigma v\rangle_{ex}$	excitation impact parameter
τ_{bin}	binning time for CCD chip
N	number of rows in the image region
h_i	height of row on CCD chip
τ_v	vertical transfer time for CCD chip
τ_m	mode switch time for CCD chip
τ_{fr}	frame time (reciprocal of the frame rate)
$S(pi)$	sensitivity for any given pixel
I_s	intensity of light from the integrating sphere
$N(pi)$	number of photons counted at each pixel number
λ_{pi0}	spectrometer wavelength
D	dispersion relation
$\Delta\lambda$	separation of two spectral lines
Δpi	measured separation of two spectral lines in pixels
λ_{pi0}	known wavelength of the line at the centre of the image region
pi	horizontal pixel number, $pi = 0$ is the centre of the image region
$\Delta\lambda_{\text{final}}$	final recorded Doppler shift
$\Delta\lambda_{\text{obs}}$	observed shift in measured wavelength
$\Delta\lambda_{\text{ref}}$	wavelength shift of reference chord
T_{raw}	ion temperature prior to correction for instrument function
T_{instr}	offset temperature due to instrument function
λ_0	centroid wavelength of a spectral line
$\Delta\lambda_0$	shift in centroid wavelength
I_0	centroid intensity of a spectral line
χ	excitation rate
σ	standard deviation
μ	mean number of counts
W_{FWHM}	full width of spectral line at half the peak value
N	number of counts per pixel
σ_W	total width of spectral line

Waves and Instabilities

ω	wave frequency
$\boldsymbol{k}$	wave vector
$\boldsymbol{\xi}$	displacement
$\boldsymbol{\xi_0}$	amplitude
x	spatial coordinate in wave equation
γ	growth term
E_{ELM}	energy lost during an ELM
E_{TOTAL}	energy stored in the plasma

P_{cr}	critical input power for type III ELMs
m	poloidal mode number
n	toroidal mode number
τ_{ELM}	inter-ELM period
ν_{ELM}	ELM frequency

Miscellaneous

t	time
$L_{\perp}$	pressure gradient scale length
L_x	gradient scale length of parameter x
τ_{EXP}	current rise time from model using experimental data
α_x	power law term for SCENE numerical code
c	scaling factor $\alpha/\hat{\alpha}$

References

R J Akers, L C Appel, E Arrends, C Byrom, M Cox, M Tournianski, P G Carolan, N J Conway, S Gee, M Nightingale, M Gryaznevich, K G McClements, M J Walsh, A Sykes, S J Fielding, P Helander, H R Wilson, S Medley, and L Roquemore. On the neutral beam heating of spherical tokamak plasmas. In *IAEA Fusion Energy, 18th Conference Proceedings*, October 2000.

M Alonso and E J Finn. *Fundamental University Physics III: Quantum and Statistical physics*. Addison-Wesley Publishing Company, 1968.

D T Anderson and P R Garabedian. A stellarator configuration for reactor studies. *Nuclear Fusion*, **34**(6):881, 1994.

L A Artsimovich. Ion energy balance explained by classical collisional processes. *Nuclear Fusion*, **12**:215, 1972a.

L A Artsimovich. Tokamak devices. *Nuclear Fusion*, **12**(12):215–252, 1972b.

R Aymar. ITER Overview. *Fusion Engineering and Design*, **36**(1):9, 1996.

D A Baker. A review of the experimental and theoretical status of the reversed-field pinch. In *Fusion Energy and Plasma Physics. Energy Independence Conference*, pages 730–753, 1987.

G Bateman. *MHD Instabilities*. Cambridge, MIT Press, 1978.

H Behrendt, W Bohmeyer, L Dietrich, G Fussman, H Greuner, H Grote, M Kammeyer, P Kornejew, M Laux, and E Pasch. Parallel electron temperature and density gradients measured in the JET divertor using thermal helium beams. *Journal of Nuclear Materials*, **241-243**:426–432, 1997.

K L Bell, H B Gilbody, J G Hughes, A E Kingston, and F J Smith. Atomic and Molecular Data for Fusion Part 1. Recommended cross sections and rates for electron ionisation of light atoms and ions. Technical Report **CLM-R216**, Culham Laboratory, 1982.

I B Bernstein, A E Frieman, M D Kruskal, and R M Kulsrud. An energy principle for hydromagnetic stability problems. *Proceedings of the Royal Society*, **A223**:17, 1958.

P R Bevington. *Error Analysis and Data Reduction*. McGraw-Hill book company, 1969.

R J Bickerton, J W Connor, and J B Taylor. Diffusion driven plasma currents and bootstrap tokamak. *Nature Physical Science*, **229**:110, 1971.

M Brix. *Messung von Elektronentemperatur und -dichte mittels Heliumstrahldiagnostik im Randschichtplasma eines Tokamaks*. PhD thesis, Ruhr-Universität Bochum, 1998.

P K Browning et al. Progress on SPHEX, the spheromak at UMIST. In *11th US-Japan Workshop on Field-Reversed Configurations with Steady-State High-Temperature Fusion Plasmas*, 1989.

B E Burke et al. Use of charge-coupled device imagers for charged-particle spectroscopy. *Review of Scientific Instruments*, **68**(1):599, 1997.

K H Burrell et al. Confinement physics of H-mode discharges in DIII-D. *Plasma Physics and Controlled Fusion*, **31**(10):1649–1644, 1989.

P Carolan, R O'Connell, N J Conway, R A Bamford, J Hugill, and I M Melnick. Toroidal and poloidal rotation in the COMPASS-D tokamak. In *22nd European Physical Society Conference on Controlled Fusion and Plasma Physics*, 1995. Contributed papers, Part 2. p133.

P G Carolan, N J Conway, A R Field, P B Jones, and H Meyer. Synergy of Multiviewing spectroscopic diagnostic on COMPASS-D. *Review of Scientific Instruments*, **72**(Issue 1, Part 11):881–887, 2001.

P G Carolan, N J Conway, M R Tournianski, M P S Nightingale, and M J Walsh. A Doppler Spectroscopy Diagnostic to Study the Ion Temperature, Rotation and Confinement in Neutral-Beam-heated START Plasmas. *Plasma Physics Reports*, **24**(3):206–213, 1998.

P G Carolan, A R Field, H Meyer, C D Challis, G Cunningham, A Kirk, M Valovic, R Akers, E A Arends, P J Catto, N J Conway, G F Counsell, S J Fielding, T Fulop, P Helander, P B Jones, B Lloyd, M McGrath, A Patel, A Sykes, D M A Taylor, M R Tournianski, M J Walsh, H R Wilson, and the MAST and NBI Teams. H-mode access physics in MAST. In *IAEA Fusion Energy Conference*, 2002.

P G Carolan et al. Characteristics of Ohmic H-modes in COMPASS-D. *Plasma Physics and Controlled Fusion*, **36**(Supplement A):A111–A116, 1994.

G G Castle, A W Morris, D Gates, and M Valovič. Halo Currents and VDEs in COMPASS-D. In *23rd European Physical Society Conference on Controlled Fusion and Plasma Physics*, volume **20C**, pages 420–423, 1996.

F F Chen. *An introduction to Plasma Physics and Controlled Nuclear Fusion*. Plenum Press, 1984.

D Ciric, T T C Jones, D C Edwards, D Martin, A J Bickley, D P D Brown, S J Cox, A J Dines, J A Dodding, J J Milnes, S R Shaw, D Stork, E Surrey, M J Watson, D Young, I D Young, P Bayetti, and J Doncel. Upgrade of the JET neutral beam heating system. In *Proceedings of the 19th IEEE/NPSS Symposium on Fusion Engineering*, January 2002.

A L Colton, R J Buttery, S J Fielding, D A Gates, T C Hender, J Hugill, A W Morris, M Valovic, and the COMPASS and ECRH teams. ELM studies on the COMPASS-D tokamak. *Plasma Physics and Controlled Nuclear Fusion*, **38**:1359–1365, 1996.

J W Connor. Edge-localised modes-physics and theory. *Plasma Physics and Controlled Fusion*, **40**(7):2687–2700, 1998.

J W Connor, R J Hastie, and J B Taylor. Shear, Periodicity and Plasma Ballooning Modes. *Physical Review Letters*, **40**(6):396–399, 1978.

J W Connor, R J Hastie, H R Wilson, and R L Miller. Magnethydrodynamic stability of tokamak edge plasmas. *Physics of Plasmas*, **5**:531–542, 1998.

N J Conway. *Study of ion behaviour on tokamaks using active and passive doppler spectroscopy*. PhD thesis, University College, Dublin, 1998.

B Coppi and M N Rosenbluth. Collisional interchange instabilities in shear and $\int \mathrm{d}l/B$ stabilized systems. In *IAEA Culham*, page 617, 1965.

S P Cunningham. Conference on Thermonuclear reactors, 1955. US Atomic Energy Commission Report No. **279** p279.

S J Davies, P D Morgan, Y Ul'Haq, C F Maggi, S K Erents, W Fundamenski, L D Horton, A Loarte, G F Mathews, and R D Monk P C Stangeby. Parallel electron temperature and density gradients measured in the JET divertor using thermal helium beams. *Journal of Nuclear Materials*, **241-243**:426–432, 1997.

Displaytech Inc. *FLC Drivers User Manual*. 2602 Cloverbasin Drive, Longmont, Co 80503, USA, 1991.

E J Doyle, R J Groabner, K H Burrell, P Gohil, T Lehecka, Jr N C Luchmann, H Matsumoto, T H Osbourne, W A Peebles, and R Philipona. Modifications in turbulence and edge electric fields at the L-H transition in the DIII-D tokamak. *Physics of Fluids B*, **3**(8):2300–2307, 1991.

T Edlington and R Wylde. A multichannel interferometer for electron density measurements in COMPASS. *Review of Scientific Instruments*, **63**(10):4968–4970, 1992.

A R Field, P G Carolan, N J Conway, and M G O'Mullane. Optimised instrumentation for edge T_e and n_e measurements on COMPASS-D tokamak from HeI line intensity ratios. *Review of Scientific Instruments*, **70**:355–358, 1999a.

A R Field, S J Fielding, , P Helender, H R Wilson, J M A Ashbourne, P G Carolan, P B Jones, and M G O'Mullane. H-mode studies using HELIOS (HElium Injection and Optical Spectroscopy) diagnostic on COMPASS-D tokamak. *Europhysics Abstracts*, Awaiting Publication, 1999b.

S Fielding, J D Ashall, A Colton, D Gates, A W Morris, M Valovic, and the COMPASS-D and ECRH teams. The H-mode in COMPASS-D. *Plasma Physics and Controlled Nuclear Fusion*, **38**:1091–1102, 1996.

S J Fielding, R J Buttery, A R Field, P B Jones, H Meyer, M Valovic, H R Wilson, and the COMPASS-D and ECRH Teams. ELM control in COMPASS-D. In *28th European Physical Society Conference on Controlled Fusion and Plasma Physics*, 2001.

S J Fielding, M Valovic, P G Carolan, D A Gates, C Hunt, P Leahy, A W Morris, and the COMPASS-D and ECRH Teams. H-modes on COMPASS-D with high-power ECRH. *Plasma Physics and Controlled Nuclear Fusion*, **40**:731–735, 1988.

T Fujimoto. Semi-empirical cross sections and rate coefficients for excitation and ionization by electron collision and photoionization of helium. Technical Report **IPPJ-AM-8**, Nagoya University, Institute of Plasma Physics, 1978.

T Fujimoto. A collisional-Radiative model for helium and it's application to a discharge plasma. *Journal of Quantitative Spectroscopy*, **21**(5):439–455, 1979.

T Fujita. Spatial structure of internal and edge transport barriers. *Plasma Physics and Controlled Fusion*, **44**(Supplement 5A):A19–A35, 2001.

P Gohil et al. Study of giant edge-localized modes in DIII-D and comparison with ballooning theory. *Physical Review Letters*, **61**(14):1603–1606, 1988.

R J Goldston. Energy confinement scaling in tokamaks: some implications of recent experiments with ohmic and strong auxiliary heating. *Plasma Physics and Controlled Fusion*, **26** (1A):87–103, 1984.

C Gormezano. High performance tokamak operation regimes. *Plasma Physics and Controlled Fusion*, **41**(Supplement 12B):B367–B380, 1999.

C Gormezano et al. Overview of JET results in support of the ITER physics basis. *Nuclear Fusion*, **41**(10):1327–1340, 2001.

JM Greene and M S Chance. The second region of stability against ballooning modes. *Nuclear Fusion*, **21**(4):453–464, 1981.

H R Griem. *Spectral Line Broadening by Plasmas*. Academic Press, 1974.

R J Groebner and T H Osbourne. Scaling studies of high mode pedestal. *Physics of Plasmas*, **5**(5):1800–1806, 1998.

R J Hawryluk et al. TFTR plasma regimes. In *Plasma Physics and Controlled Fusion Research, 11th International Conference, Kyoto*, volume **1**, pages 51–64, 1986.

R D Hazeltine and J D Meiss. *Plasma Confinement (Frontiers in Physics, Vol, 86)*. Addison-Wesley Publishers, 1992.

C C Hegna, J W Connor, R J Hastie, and H R Wilson. Toroidal coupling of ideal magneto-hydrodynamic instabilities in tokamak plasmas. *Physics of Plasmas*, **3**:584, 1996.

J F Holzrichter. Laser fusion update. A historical overview of inertial confinement fusion at Livermore. *Lasers and Applications*, **2**(3):65–70, 1983.

K I Hopcraft. *Plasma Physics*, chapter Magnetohydrodynamics. Cambridge University Press, 1993.

L D Horton, J C Fuchs, S Günter, M Jakobi, P J McCarthy, H Murmann, J Neuhauser, S D Pinches, S Saarelma, J K Stober, W Suttrop, and the ASDEX Upgrad Team. Pedestal Physics at ASDEX Upgrade. In *29th EPS Conference on Controlled Fusion and Plasma Physics*, 2002.

O A Hurricane, B H Fong, and S C Cowley. Nonlinear magnethydrodynamic detonation: Part 1. *Physics of Plasmas*, **4**(10):3565, 1997.

I H Hutchinson. *Principles of Plasma Diagnostics*. Cambridge University Press, 1987.

G T A Huysmans, H J de Blanck, W Kerner, J P Goedbloed, and M F F Nave. . In *19th EPS Conference on Controlled Fusion and Plasma Physics*, volume 16C Part 1, page 247, 1992.

Y Igitkhanov, O P Poguste, H R Wilson, J W Connor, H Wobig, P Grigull, M Hirsch, G Janeschitz, A Loarte, G Saibene, R Sartori, G Pacher, and H Pacher. A physics picture of type I ELMs. *Plasma Physics*, **42**(2-4):272–276, 2002.

R Itatani, Y Yasaka, and H Imaizumi. Research program on mirror confinement in Kyoto University. In *Physics in Open Ended Fusion Systems: International Symposium*, pages 179–185, 1980.

Y Kamada, K Ushigusa, O Naito, S Ishida, T Fujita, R Yoshino, MKikuchi, M Mori, and H Ninomiya. ELMy H-mode with high β_N and high β_p in JT-60U. *plasma Physics and Controlled Fusion*, **36**:A123–A128, 1994.

T Kass, S Günter, M Marascheck, W Suttrop, H Zohm, and the ASDEX-Upgrade team. Characteristics of type I and type III ELM precursors in ASDEX-Upgrade. In *24th European Physical Society Conference on Controlled Fusion and Plasma Physics*, volume **21A**, pages 1521–1524, 1997. Contributed papers.

P Kornejew. *Bestimmung der Elktronenparameter in Randschichtplasmen unter Verwendung eines thermischen Heliumstrahls*. PhD thesis, Humbolt-Universität, Berlin, 1996.

L L Lao, L C Appel, M K Bevir, and M J Walsh. Reconstruction of current profile parameters and plasma shapes in tokamaks. *Nuclear Fusion*, **25**(11):1611–1622, 1985.

J D Lawson. Some criteria for a power producing thermonuclear reactor. *Nuclear Fusion*, **B70**:6, 1957.

F M Levinton, L Zakharov, S H Batha, J Manickam, and M C Zarnstorff. Stabilization and Onset of Sawteeth in TFTR. *Physical Review Letters*, **72**(18):2895–2898, 1994.

J Lingertat, K Borass, S Clement, G Fishpool, E Gauthier, J de Haas, G Huysmans, L Porte, P Ssmeulders, V Parail, and R Reiche. The ELM operational window and power deposition in JET. In *24th EPS Conference on Controlled Fusion and Plasma Physics*, 1997. Poster 24.

A Loarte, G Saibene, R Sartori, G Janeschitz, Y Igitkahov, A S Kukushkin, M Sugihara, D P Coster, A Hermann, L D Horton, J Stober, N Asakura, k Itami, H Tamai, G Mathews, R Schneider, D Reiter, A W Leonard, and G D Porter. Predicted ELM Energy Loss and Power Loading in ITER-FEAT. In *IAEA Fusion Energy, 18th Conference Proceedings*, October 2000.

D Lortz. The general "Peeling" instability. *Nuclear Fusion*, **15**:49–54, 1975.

H Lütjens, A Bondeson, and A Roy. Axisymmetric mhd equilibrium solver with bicubic hermite elements. *Computational Physics Communications*, **69**:287, 1992.

J Manickam. The role of edge current density on kink mode stability and its implication for magnetohydrodynamic activity associated with edge localized modes. *Physics of Fluids B*, **4**:1901–1908, 1992.

C Mercier. Un Critere necessaire de stabilite Hydromagnetique pour un plasma en symetrie de revolution. *Nuclear Fusion*, **1**:47–53, 1960.

H. Meyer, P G Carolan, N J Conway, A R Field, S J Fielding, and P Helander. Profile evolution of edge parameters during L/H and H/L mode transitions on COMPASS-D. *Czechoslovak Journal of Physics*, **50**(12):1451–1461, 2000.

O Naito and the JT-60 team. Steady state plasma performance on JT-60U. *Plasma Physics and Controlled Fusion*, **33**(Supplement (12)B):B215, 1993.

T H Osbourne, R J Groebner, L L Lao, A W Leonard, R Maingi, R L Miller, G D Porter, D M Thomas, and R E Waltz. Scaling of ELM and H-mode pedestal characteristics in ITER shape discharges in the DIII-D tokamak. In *24th European Physical Society Conference on Controlled Fusion and Plasma Physics*, volume 3, page 1101, 1997. Contributed papers.

T Ozekiet al. Plasma shaping, edge ballooning stability and ELM behaviour in DIII-D. *Nuclear Fusion*, **30**(8):1425, 1990.

D Pfirsch and A Schlüter. Der Einfluss der elektrischen Leitfähigkeit auf das Gleichgewichtsverhalten von Plasmen neidrigen Drucks in Stellaratoren. Technical Report **MPI/PA/7/62**, Max-Planck Institut, 1962.

O Pogutse, Y Igitkhanov, J G Cordey, and G Janeschitz. A possible physical explanation for type 111 ELMs in tokamaks. In *20th Symposium on Fusion Technology in **JET-CP(99)***, page 150, 1999.

W H Press, B P Flannery, S A Teukolsky, and W T Varenna. *Numerical Recipes*. Cambridge University Press, 2nd edition, 1992.

C M Roach and A Thyagaraja. . Technical Report **PPN 01/1.1**, UKAEA/Euratom Fusion Association, 2002.

S Sasaki, S Takamura, and T Kato. Effective ionization and emission rate coefficients of the helium atom in a plasma. *Fusion Engineering and Design*, **34 & 35**:747, 1997.

S Sasaki, S Takamura, S Masuzaki, S Watanabe, T Kato, and K Kadota. Helium I line intensity ratios in a plasma for the diagnostics of fusion edge plasmas. *Review of Scientific Instruments*, **67**(10):3521, 1996.

K Sawada, K Eriguchi, and T Fujimoto. Hydrogen-atom spectroscopy of the ionizing plasma containing molecular hydrogen: Line intensities and ionization rate. *Journal of Applied Physics*, **73**(12):8122–8125, 1993.

B Schweer, G Mank, and A Pospiezczyk. Electron temperature and electron density profiles measured with a thermal He-beam in the plasma boundary of TEXTOR. *Journal of Nuclear Materials*, **196-198**:174–178, 1992.

V D Shafranov. On magnetohydrodynamical equilibrium confirgurations. *Soviet Physics JETP*, **6**:545, 1958.

P B Snyder, H R Wilson, J R Ferron, L L Lao, A W Leonard, T H Osbourne, A D Turnbull, D Mossessian, M Murakami, and X Q Xu. Edge localised modes and the pedestal: A model based on coupled peeling-balooning modes. *Physics of Plasma*, **5**(5):2037–2043, 2002.

R D Stambaugh et al. Enhanced confinement in tokamaks. *Physics of Fluids B: Plasma Physics*, **2**(12):2941, 1990.

H P Summers. Atomic Data and Analysis Sturcture. Technical Report **JET-IR(94)06**, JET Joint Undertaking, 1994.

P R Thomas, D J Campbell, A Gondhalekar, C J Lowry, and The JET Joint Undertaking. Steady state H-modes in JET. In *19th European Conference on Controlled Fusion and Plasma Physics*, pages 175–180, 1992.

M R Tournianski, P G Carolan, G F Counsell, and M G O'Mullane. Use of 1D D_α camera to measure edge neutral and electron density evolutions. In *International Diagnostics Conference, Varena*, August 2001.

M Valovic, M Edwards, D Gates, S J Fielding, T C Hender, J Hugil, A W Morris, and the COMPASS team. L-H transitions and ELMs on COMPASS-D. In *21st European Physical Society Conference on Controlled Fusion and Plasma Physics*, volume **1**, pages 105–127, 1994. Contributed papers.

O Vollmer, R Aratari, F Rhyter, K H Steuer, F Wagner, and Ther ASDEX and NI teams. Long-pulse heating in ASDEX L- and H-mode discharges. In *17th EPS conference on Controlled Fusion and Plasma Heating*, volume Part I, page 295, 1990.

F Wagner and K Lackner. *Physics of Plasma Wall Interactions in Controlled Fusion*, chapter Divertor tokamak experiments, pages 931–1004. Plenum press, 1986.

F Wagner et al. Regime of Improoved Confinement and High Beta in Neutral-Beam-Heated Divertor Discharges of the ASDEX Tokamak. *Physical Review Letters*, **49**(19):1408–1412, 1982.

F Wagner et al. Recent results of H-mode studies on ASDEX. In *13th International Conference of Plasma physics and controlled nuclear fusion*, volume **1**, pages 277–290, 1990. IAEA Vienna.

J Wesson, editor. *Tokamaks*. Oxford University Press, 2nd edition, 1997.

H R Wilson. SCENE-Simulation of Self-Consistent Equilibria with Neoclassical Effects. Technical Report **UKAEA FUS 271**, UKAEA/Euratom Fusion Association, 1994.

H R Wilson and J W Connor. Ballooning instabilities, poloidal flow and the temperature pedestal at the tokamak edge. In *Proceedings of the 13th International Conference on Controlled Fusion and Plasma Physics*, volume Part I, page 289, 1997.

H R Wilson, J W Connor, A R Field, S J Fielding, and R J Hastie. influence of the plasma edge on tokamak performance. *Nuclear Fusion*, **40**(3Y):713–720, 2000.

H R Wilson, J W Connor, A R Field, S J Fielding, R L Miller, L L Lau, and A D Turnbull. Ideal Magnetohydrodynamic stability of the tokamak high-confinement-mode edge region. *Physics of Plasma*, **6**(5):1925–1934, 1999.

H R Wilson, P B Snyder, and G T Huysmans. Coupled peeling-ballooning modes:A model for ELMs and the temperature pedestal? In *28th European Physical Society Conference on Controlled Fusion and Plasma Physics*, volume 25A, pages 1752–1756, 2001.

H Zohm. Edge localised modes (ELMs). *Plasma Physics and Controlled Nuclear Fusion*, **38**:105–128, 1996.